# Band Anticrossing Effects in Highly Mismatched Semiconductor Alloys

by

Junqiao Wu

B.S. (Fudan University) 1993

M.S. (Peking University) 1996

A dissertation submitted in partial satisfaction of the requirements for the degree of

Doctor of Philosophy
in

Applied Science and Technology

in the

GRADUATE DIVISION

of the

UNIVERSITY OF CALIFORNIA, BERKELEY

Committee in charge:

Professor Eugene E. Haller, Chair

Professor Ture K. Gustafson

Professor Alan M. Portis

Dr. Wladyslaw Walukiewicz

Fall 2002

Abstract

Band Anticrossing Effects in Highly Mismatched Semiconductor Alloys

by

Junqiao Wu

Doctor of Philosophy in
Applied Science and Technology

University of California, Berkeley

Professor Eugene E. Haller, Chair

The first five chapters of this thesis focus on studies of band anticrossing (BAC) effects in highly electronegativity-mismatched semiconductor alloys. The concept of bandgap bowing has been used to describe the deviation of the alloy bandgap from a linear interpolation. Bowing parameters as large as 2.5 eV (for ZnSTe) and close to zero (for AlGaAs and ZnSSe) have been observed experimentally. Recent advances in thin film deposition techniques have allowed the growth of semiconductor alloys composed of significantly different constituents with ever-improving crystalline quality (*e.g.*, $GaAs_{1-x}N_x$ and $GaP_{1-x}N_x$ with $x < \sim 0.05$). These alloys exhibit many novel and interesting properties including, in particular, a giant bandgap bowing (bowing parameters > 14 eV). A band anticrossing model has been developed to explain these properties. The model shows that the predominant bowing mechanism in these systems is driven by the anticrossing interaction between the localized level associated with the minority component and the band states of the host. In this thesis I discuss my studies of

the BAC effects in these highly mismatched semiconductors. It will be shown that the results of the physically intuitive BAC model can be derived from the Hamiltonian of the many-impurity Anderson model. The band restructuring caused by the BAC interaction is responsible for a series of experimental observations such as a large bandgap reduction, an enhancement of the electron effective mass, and a decrease in the pressure coefficient of the fundamental gap energy. Results of further experimental investigations of the optical properties of quantum wells based on these materials will be also presented. It will be shown that the BAC interaction occurs not only between localized states and conduction band states at the Brillouin zone center, but also exists over all of $\boldsymbol{k}$-space. Finally, taking ZnSTe and ZnSeTe as examples, I show that BAC also occurs between localized states and the valence band states. Soft x-ray fluorescence experiments provide direct evidence of the BAC interaction in these systems.

In the final chapter of the thesis, I describe and summarize my studies of optical properties of wurtzite InN and related alloys. Early studies performed on InN films grown by sputtering techniques suggested a direct bandgap of ~1.9 eV for this semiconductor. Very recently, high-quality InN films with much higher mobility have become available by using the molecular beam epitaxy growth method. Optical experiments carried out on these samples reveal a narrow bandgap for InN of 0.77 eV, much lower than the previously accepted value. Optical properties of InGaN and InAlN ternaries on the In rich side have also been characterized and are found to be consistent with the narrow bandgap of InN. The bandgap bowing parameters in these alloys were determined. In the context of these findings, the bandgap energies of InGaN and InAlN were found to cover a wide spectral range from the infrared for InN to the ultraviolet for GaN and deep ultraviolet

for AlN. The significance of this work is rooted in many important applications of nitride semiconductors in optoelectronics and solar energy conversion devices.

# Table of Contents

# Acknowledgements

The research work that led to this thesis was conducted under the direct supervision of Professor Eugene Haller. I would like to thank Professor Haller for his solid advice, warm encouragement and continuous support throughout the years.

It has been a great privilege and pleasure for me to work with Dr. Wladek Walukiewicz. His profound knowledge and insightful thoughts in semiconductor physics have been a crucial resource from which I have benefited immeasurably in my studies. Without his constant guidance and the invaluable discussions I had with him, it would have been impossible for me to do this work.

I would like to thank Professor Alan Portis and Professor Kenneth Gustafson for having served on my Qualifying Examination committee two years ago, and for their recent help with my thesis. Along the way they have provided me with important advice and suggestions.

I am also indebted to Dr. Kin M. Yu, Dr. Wei Shan, Dr. Joel W. Ager III and Dr. Henning Feick for sharing with me their expertise in the laboratory. I thank Professor Oscar Dubon for his assistance in all areas of the graduate school experience.

I would like to acknowledge Professor C. W. Tu's group at University of California, San Diego, Dr. W. J. Schaff's group at Cornell University, Dr. J. F. Geisz's group at National Renewable Energy Laboratory, Professor A. K. Ramdas' group at Purdue University, and Professor I. K. Sou's group at Hong Kong University of Science and Technology for providing high-quality samples. Their sample growth efforts made this research possible.

The wonderful assistance of Ms. Pat Berumen has made my study at Berkeley an enjoyable experience.

I am grateful for the support of all my fellow graduate students and staff in the Haller group. In particular, I am indebted to Ben Cardozo for his help with the Mathematica software that I used to do my calculations. Hughes Silvestri has helped me greatly in performing the Hall Effect measurements and Fourier Transform Infrared Spectroscopy. I thank Jeff Beeman for his instruction in sample lapping and polishing. David Hom has also been an essential resource and I would like to thank him for his various assistances whenever I needed.

Most importantly, I thank my parents for providing me with the opportunity of receiving this advanced education that they have missed in their own lives. Their unconditional support and encouragement are priceless.

Finally I wish to gratefully acknowledge the multi-year Berkeley Fellowship from the University of California, Berkeley, and the effort that the Applied Science and Technology Graduate Group has taken to help me earn this fellowship.

# 1. Introduction to Semiconductor Alloys

## 1.1 Virtual Crystal Approximation and Bandgap Bowing in Semiconductor Alloys

The simplest possible prediction of the physical properties of a semiconductor alloy states that they scale linearly between the properties of the endpoint semiconductors. Indeed, this is the case for lattice constants, which, in the absence of phase transitions or other complications, do scale linearly with composition to a high level of precision. This effect is expressed as the Vegard's law and has been applied widely to determine the alloy compositions in x-ray diffraction experiments.

In contrast, it has been realized for over forty years that in most cases, the band gap of an alloy semiconductor does not follow a simple linear trend with composition, and that some degree of "bowing" away from the linear dependence is observed. From the very beginning, a quadratic relationship has been used to characterize this behavior,

$$E_g^{AB}(x) = (1-x)\cdot E_g^A + x\cdot E_g^B - b\cdot x\cdot(1-x) \tag{1.1}$$

where $E_g^A$ and $E_g^B$ are the band gaps of the endpoint materials and $b$ is the optical bowing parameter. As an example, Figure 1.1 shows the bandgap bowing in $ZnSe_{1-x}Te_x$ alloys.

Given its great importance to fundamental semiconductor physics and to technology, the phenomenon of bandgap bowing has been extensively studied. In the early 1970's, it was shown that the form of Eq. (1.1) could be derived by considering the effects of alloy disorder within the currently available theoretical models, and that the value of $b$ could be estimated by considering the electronegativity mismatch of the elements in the alloy [1, 2].

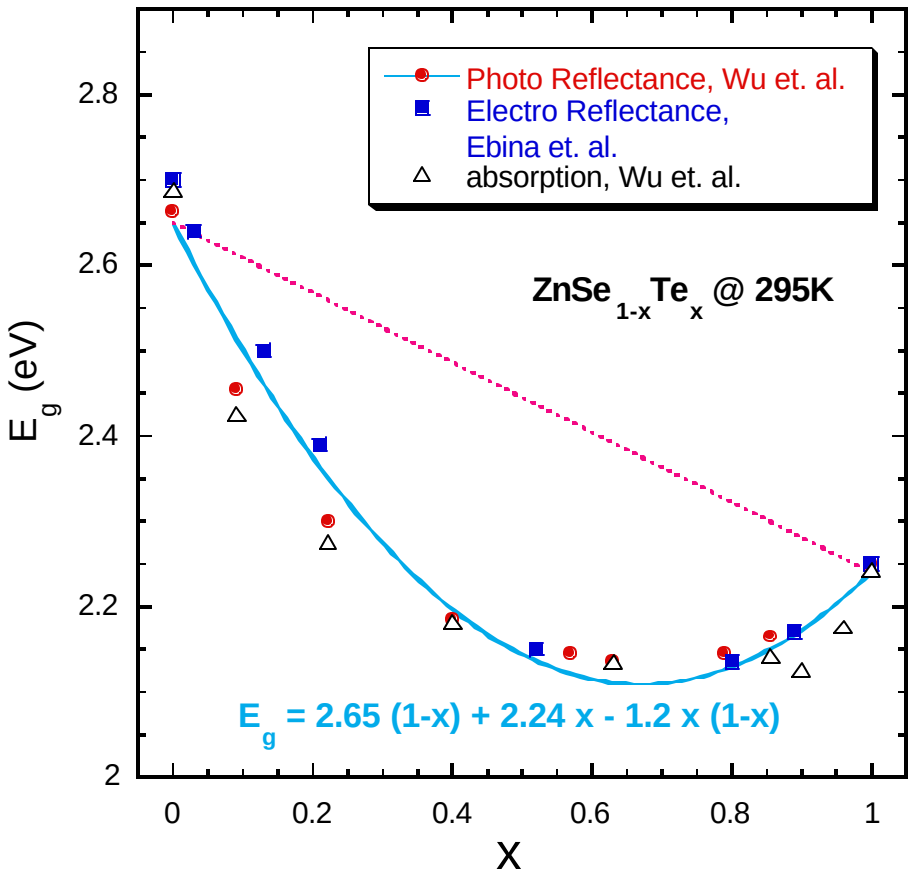


Fig. 1.1 Bandgap bowing in $ZnSe_{1-x}Te_x$ alloys. The bowing parameter $b$ is approximately 1.2 eV.

In early studies of electronic structures of random alloys in the 1930's, a linear dependence of the crystal potential on the alloy composition was adopted as the first-order approximation [3]. In this approximation the composition disorder of the alloy is neglected, and the crystal potential of the alloy that the valence electrons feel is assumed to have perfect periodicity as in pure crystalline materials. The value of this periodic

crystal potential is linearly interpolated between that of the endpoint crystals; therefore, the alloy is approximated by a new, perfect crystal with this interpolated crystal potential. Not surprisingly, this approach is named the "Virtual Crystal Approximation" (VCA). In the framework of VCA the bowing parameter for the bandgap of a semiconductor alloy is expected to be small, because there is no strong non-linearity in the dependence of the energy gap on the crystal potential in band-structure calculations. It has been proposed that the total bowing parameter should be the sum of the intrinsic bowing $b_i$ found in the VCA and the "extrinsic" bowing $b_e$ associated with disorder (non-periodicity) [1]. Table 1.1 shows the bowing parameters for the direct bandgap of some ternary alloys.

Potential fluctuations scatter electrons and mix band states, and hence modify the band structures. As a result, the composition disorder can also be responsible for the deviations from linear behavior of many other electronic properties, such as the free carrier effective mass and the spin-orbit splitting in semiconductor alloys.

| Alloy | $b_i$ (eV) | $b_e$ (eV) | $b_{calc}$ (eV) | $b_{exp}$ (eV) |
|---|---|---|---|---|
| GaAs-P | 0.21 | 0.09 | 0.30 | 0.21 |
| InAs-P | 0.15 | 0.08 | 0.23 | 0.20, 0.26 |
| Ga-InSb | 0.12 | 0.24 | 0.36 | 0.43 |
| Ga-InAs | 0.28 | 0.29 | 0.57 | 0.33, 0.56 |
| InAs-Sb | 0.03 | 0.67 | 0.70 | ≥ 0.58 |
| Ga-AlAs | 0 | 0.03 | 0.03 | ~ 0.20 |
| Ga-InP | 0.39 | 0.31 | 0.70 | 0.88 |
| ZnS-Se | 0.14 | 0.14 | 0.28 | ~ 0 |
| ZnSe-Te | -0.04 | 1.14 | 1.10 | ~ 1.28 |
| ZnS-Te | 0.28 | 2.12 | 2.40 | ~ 2.40 |
| Ag-CuI | 0.14 | 0.11 | 0.25 | 0.58 |
| CuI-Br | -0.65 | 1.54 | 0.89 | 0.44 |
| InP-N | | | | > 14 |
| GaAs-N | | | | > 14 |
| Ga-InN | | | | 1.43 |
| Al-InN | | | | 3.0 |
| Al-GaN | | | | 1.40 |

Table 1.1, the bandgap bowing parameter for some ternary alloys. All the data are from ref.[1], except for the nitrides, which are based on our own experimental results. The parameter $b_{calc}$ is the calculated value obtained using a dielectric model [1].

## 1.2 Unusual Properties of III-$V_{1-x}$-$N_x$ Alloys and Their Applications

Very recently, advances in thin film growth have led to semiconductor alloys composed of elements with very large electronegativity mismatches; the zincblende $GaAs_{1-x}N_x$ alloy is an example of such a system. Very large bandgap reductions have been observed in this system for a small percentage of As substituted with N (*e.g.*, a reduction of 0.18 eV at $x = 0.01$). Direct application of Eq. (1.1) to the observed bandgaps of $GaAs_{1-x}N_x$ with $x$ up to about 0.05 would require a bowing parameter greater than 14 eV, and would predict a negative bandgap for a large range of compositions. The direct energy gap of $GaAs_{1-x}N_x$ as a function of lattice constant is shown in Fig.1.2.

It has not yet been technically feasible to investigate this system outside of $0 < x < 0.05$ due to the large immiscibility between GaAs and GaN. However, only 5% N incorporation in GaAs already forces the bandgap down to below 1 eV. InAs, on the other hand, when alloyed with GaAs, reduces the bandgap less dramatically. The bandgap of $In_xAs_{1-x}N$ ternary does not deviate severely from the linear interpolation and the bowing is much smaller than that in $GaAs_{1-x}N_x$. Since the In atom is much larger than the Ga atom, the incorporation of InAs in GaAs increases the lattice constant and compensates the N-induced lattice contraction in $GaAs_{1-x}N_x$. The quaternary alloy system $In_yGa_{1-y}As_{1-x}N_x$ can, therefore, be grown lattice-matched on GaAs substrates by adjusting the In and N content [4]. From Fig.1.2 and Vegard's law, it can be estimated that $y \approx 3x$ is the appropriate ratio for the lattice match with GaAs substrates. Adding In to GaAsN further reduces the bandgap, but still maintains the direct type of the energy gap of the system. Consequently, InGaAsN is considered a light-emitting material having bandgap

energies suitable for the application for 1.3 and 1.55 μm laser diodes for optical fiber communication [4]. By combining InGaAsN with GaAs or other wide-gap semiconductors that can be grown pseudomorphically on GaAs substrates, very deep quantum wells can be achieved in the active layers. This novel material is very promising for overcoming the poor temperature characteristics of conventional long-wavelength laser diodes. In these structures electron overflow from the wells to the barrier layers at high operation temperatures can be efficiently suppressed due to the strong confinement in the deep wells. Shown in Fig. 1.3 is a single quantum well laser diode structure based on this quaternary alloy proposed by Kondow, *et. al.* [4].

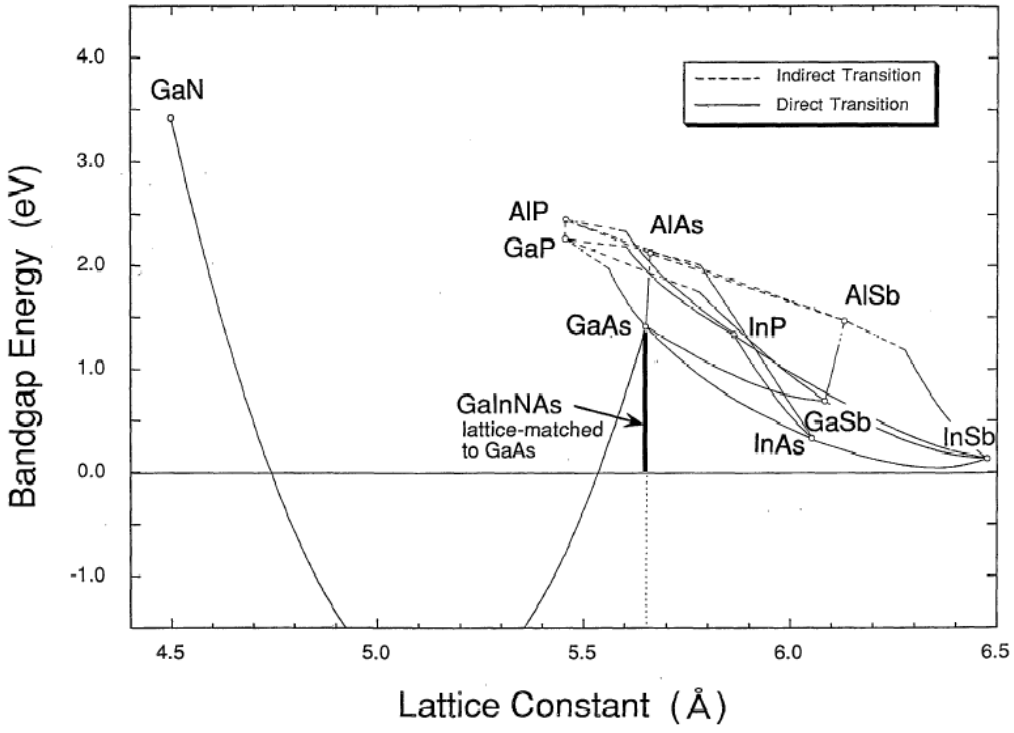


Fig.1.2 The relationship between the bandgap and lattice constant for most III-V alloys [4]. The curve for $GaAs_{1-x}N_x$ that exhibits huge bowing is a fit to experimental bandgaps on the GaAs-rich side using Eq.(1.1).

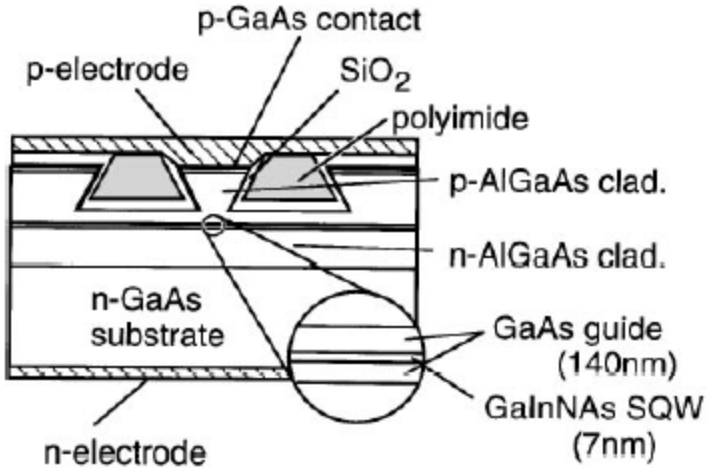


Fig. 1.3 Schematic cross section of a InGaAsN/GaAs single quantum well laser diode [4].

The InGaAsN alloy has applications not only in the area of light emitting devices, but also in multijunction solar cells. Figure 1.4 shows the solar spectrum and materials used in the multijunction solar cells that can covert the solar energy into photovoltaic current at high efficiencies. The design of the multijunction solar cell takes advantages of the fact that the materials used in the multijunction are all lattice matched (to GaAs for example) and have gap energies covering the main portion of the solar spectrum when assembled in series. The InGaAsN alloy is promising in this device because of its large band-gap tunability (0.8-1.4 eV) while lattice-matched with GaAs.

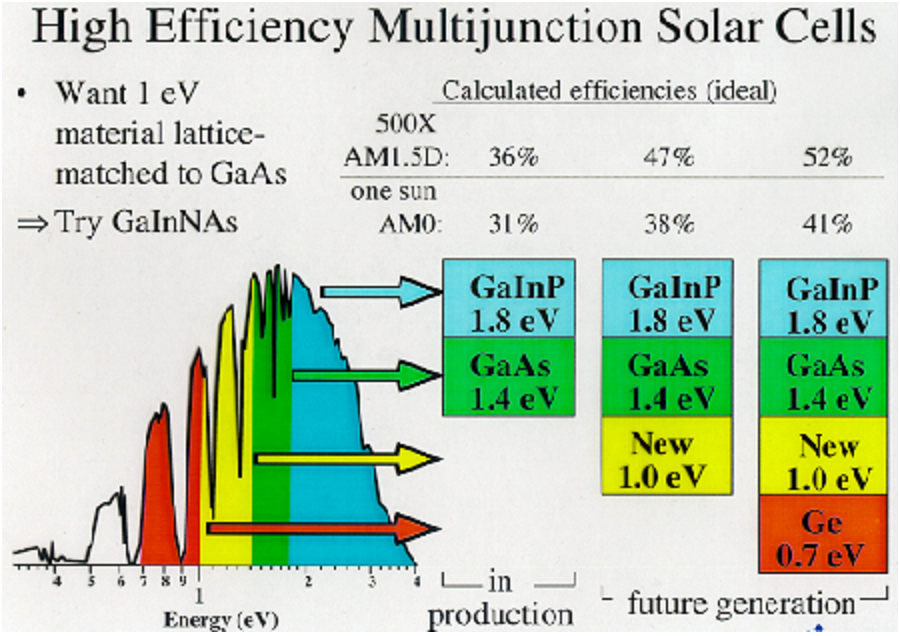


Fig. 1.4 Materials basis for multijunction solar cells. The layer in the box "New 1.0 eV" could possibly be InGaAsN lattice-matched to Ge and GaAs.

Comparably large bandgap reductions have also been observed in other N-containing alloys such as GaPN [5, 6], InPN [7], and AlGaAsN [8], which will be discussed in this thesis. The strong dependence of the bandgap on the N content has made dilute III-V nitrides important materials for a large variety of applications. The materials physics behind the huge bandgap bowing in these dilute nitrides also needs to be understood from the basic research point of view.

# 2. Isovalent Impurity States in Semiconductors

## 2.1 Formation of Isovalent Impurity States

When a substitutional impurity atom has the same valence as the host atom it replaces, it is referred to as an isovalent or isoelectronic center. Although they have the same valence, the impurity atom may differ from the host atom in many other aspects, such as a different atom size and different electronegativity. When these differences are significant, they may result in local defect potential associated with the isovalent impurities. However, isovalent centers appear electrically neutral to the host crystal except within the immediate vicinity of the impurities. Their potentials are thus short-range, rather than long-range as in the case of the Coulomb potential of hydrogenic defects. The highly localized nature of these potentials causes the isovalent states to behave like deep centers in spite of the fact that their binding energies are very small. In general, therefore, the definition of the term "deep level" is extended to including these defect states that have shallow energy levels but cannot be described by the effective mass theory of hydrogenic impurities [9]. Unlike hydrogenic states, deep states have localized wavefunctions in real space which may involve Bloch functions from several bands over a large region of $\boldsymbol{k}$-space. Their energy levels, therefore, do not follow one specific band minimum (as the hydrogenic states do) when the band structure is gradually changed by external causes such as applying pressure, changing temperature, and alloying with other materials.

To calculate the energy positions of these deep levels, one needs to know the defect potential and then solve the corresponding Schrödinger equation. In many cases the exact functional form of the localized potential is not very crucial; the deep center wavefunction is predominantly determined by the host crystal rather than by the deep impurity. The main difficulty of the problem lies in the second step, *i.e.*, finding the solution to the Schrödinger equation.

In 1980, Hjalmarson *et. al.* made the first systematic theoretical investigation of this problem [10]. Employing a Koster-Slater model for the localized potential, they established the eigenvalue equation in a tight-binding-function basis. For $A_1$-symmetry deep states, the strength of the defect potential was assumed to be equal to the difference between the *s* atomic orbital energies of the impurity and the host atom it substitutes. The energy levels for various substitutional impurities in common host semiconductors were calculated by solving this eigen-value equation [10]. The results reproduce reasonably well the chemical trend of the deep levels observed in experiments and are shown in Fig.2.1.

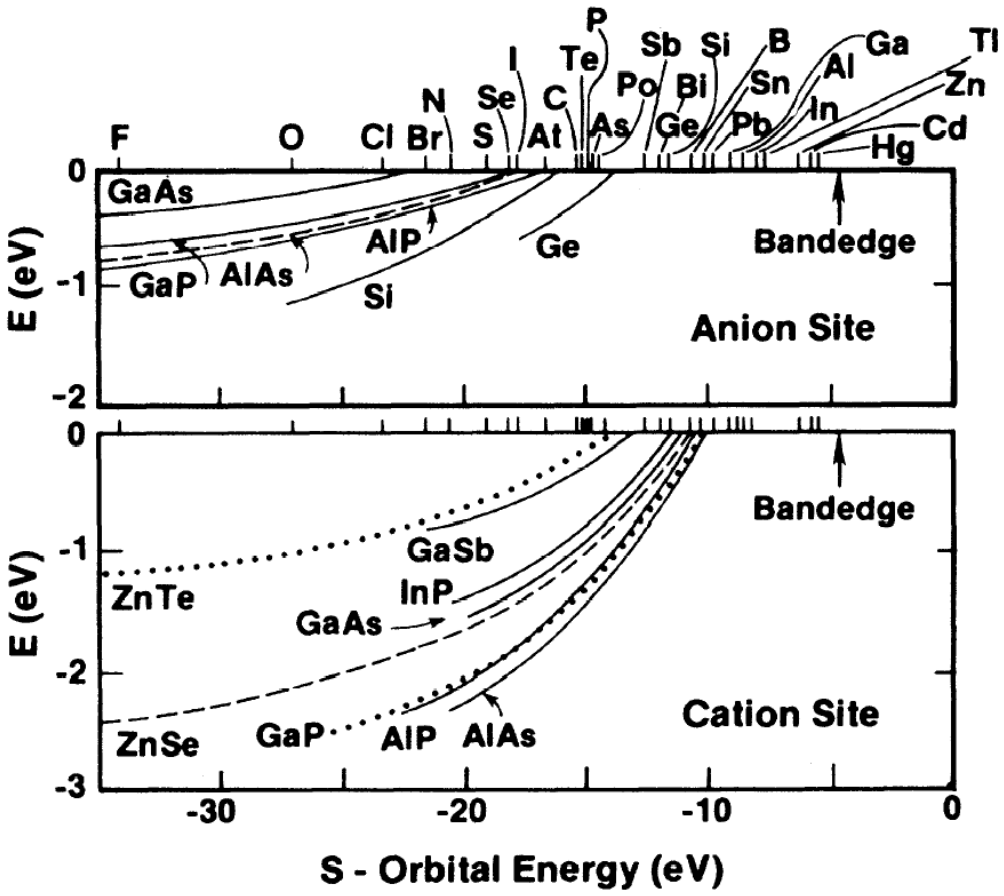


Fig. 2.1 Calculated energies of the $A_1$-symmetry deep levels in various diamond and zinc-blende semiconductors [10]. The relevant impurities are listed above the upper horizontal axis in the order of decreasing defect potentials. The energy on the vertical axis is referenced to the conduction band minimum.

As an example of isovalent impurities which are particularly relevant to this thesis, we can see from Fig. 2.1 that nitrogen substituting group V element in GaP produces a deep level in the bandgap with energy close to the conduction band minimum. In GaAs, in contrast, N substituting group V element forms a level above the conduction band edge, *i.e.*, it becomes a resonant state in the conduction band.

## 2.2 Experimental Observations

When the ternary alloy $GaAs_{1-x}P_x$ is formed between GaAs and GaP, the location of the lowest conduction band minimum in reciprocal space switches from the zone center ($\Gamma$ point) to the zone edge (X point) at $x \sim 0.45$. As a result, the slope of the conduction band minimum versus $x$ (hence the slope of the energy levels of hydrogenic donors, which always follow the conduction band minimum) changes abruptly at $x$~0.45. On the other hand, the energy level of deep states, such as O and N in $GaAs_{1-x}P_x$, varies continuously with $x$. This is because the energy of a deep state is determined by the entire band, rather than by the lowest band minimum only, as in the case of hydrogenic states. The energy levels discussed here are shown as a function of $x$ in Fig.2.2. The calculations show reasonably good agreement with experimental data; especially in the case of N in $GaAs_{1-x}P_x$, the theory predicts a single slope for $E_N$ as a function of $x$, a "shallow" bound state in GaP and a resonant state in GaAs, which are all experimentally confirmed.

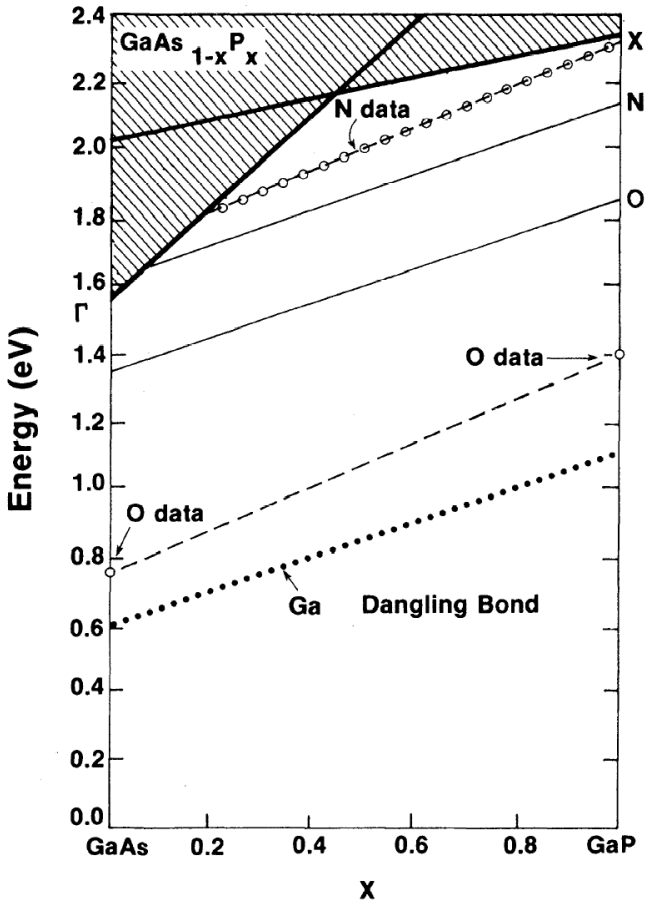


Fig.2.2 Comparison of predictions with experimental data for the N and O $A_1$-symmetry deep levels as a function of the $GaAs_{1-x}P_x$ alloy composition.

The resonant nature of the N level in GaAs can be seen from the $E_N$ versus $x$ plot in Fig. 2.2. The extrapolation of this line to $x$=0 yields an energy level of $E_N \sim 1.7$ eV in GaAs (at low temperature), which is above the conduction band minimum. This resonant level does not bind electrons or excitons, but the impurity will behave as an efficient scattering center for free electrons in transport process.

Another verification of this N resonant level in GaAs has been obtained by Wolford *et. al.* [11] using hydrostatic pressure. The pressure coefficient of the Γ conduction band minimum in GaAs is as large as 10 meV/kbar. The N level is much less

sensitive to applied pressure, because its wavefunction contains the Bloch states over a large region in the Brillouin zone. The pressure coefficient of $E_N$ takes the average of the coefficients of all band states in $\boldsymbol{k}$-space, much like the behavior of the composition dependence. As the pressure increases, the N resonant level therefore gradually moves into the energy gap and becomes a bound state. The energy position of this bound state can be determined from the emission line of excitons that are bound to this N level. The results are shown in Fig. 2.3. Similar to the energy versus composition plot, the extrapolation of the pressure dependence to ambient pressure shows a resonant energy for the N level at ~1.7 eV.

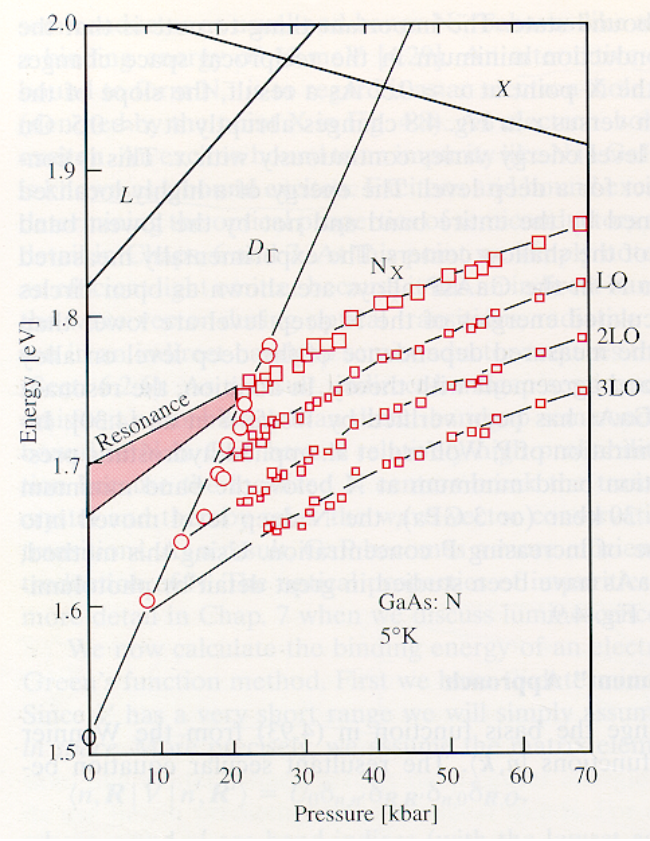


Fig. 2.3 The energies of L and X band minima, shallow-donor-bound excitons, and N localized states and its phonon replica as a function of applied hydrostatic pressure in GaAs [9, 11].

GaP is an indirect-gap semiconductor. However, it has been realized for a long time that GaP becomes an efficient light emitter with the introduction of small amounts of N. Light emitting diodes based on $GaAs_{1-x}P_x$ : N have been commercially manufactured with wavelength covering the spectral range from the red to the green. The N impurities were believed to break the translational invariance in the crystal and relax the momentum conservation in the light emission process. Recent progress in epitaxial growth techniques provides the availability of GaAs and GaP films incorporated with N at alloy concentration (~ several percent). These alloys exhibit new, interesting optical properties that cannot be understood by the simple theory that has been used to explain the properties of GaP : N at doping concentrations.

# 3. Highly-mismatched Semiconductor Alloys: Group III-V Based

## 3.1 Electronegativity Mismatch of the Constituents of Semiconductor Alloys

Electronegativity of the elements is an important property, which Pauling has described in qualitative terms as “the power of an atom in a molecule to attract electrons to itself.” [12]. A widely-used quantitative definition of the electronegativity has been proposed by Mulliken [13]. He uses the arithmetic mean value of the first ionization energy and the electron affinity of the element. The values of the electronegativity are plotted in Fig.3.1 for most of the group II, III, VI, V and VI elements starting from the second period [14].

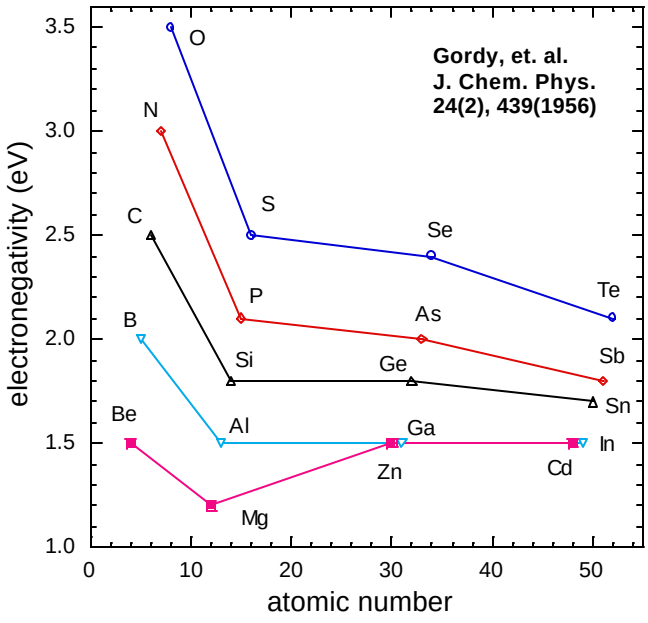


Fig.3.1 Electronegativity of the elements as a function of atomic number [14].

It can be seen that, except for group II, the electronegativity of the elements in the second period is much larger than that of the rest of the same group. Therefore, as the atoms in a semiconductor are substituted with elements in the same group, the resultant isovalent alloy can be classified into three categories based on the difference in the electronegativities of the elements involved. Some examples of ternary alloys are listed in Tab.3.1.

| category | alloys | Electronegativity difference (eV) |
|---|---|---|
| Highly mismatched | III-N-As | 1.0 |
| | III-N-Sb | 1.2 |
| | III-N-P | 0.9 |
| | II-O-Te | 1.4 |
| | II-O-Se | 1.1 |
| | II-O-S | 1.0 |
| Moderately mismatched | II-S-Te | 0.4 |
| | II-Se-Te | 0.3 |
| Lightly mismatched | III-P-As | 0.1 |
| | II-S-Se | 0.1 |

Tab.3.1 classification of semiconductor alloys based on the electronegativity difference.

The classification based on the difference in the electronegativities of constituent elements can be justified by the electronic behavior of the alloy. For example, GaAsP

belongs to lightly mismatched alloys because the electronegativity difference between P and As is only 0.1 eV. The bandgap of GaAsP shows a nearly linear dependence on composition as predicted by the VCA theory. In Fig.3.2, the minimum bandgap of GaAsP is shown as a function of GaP fraction [15].

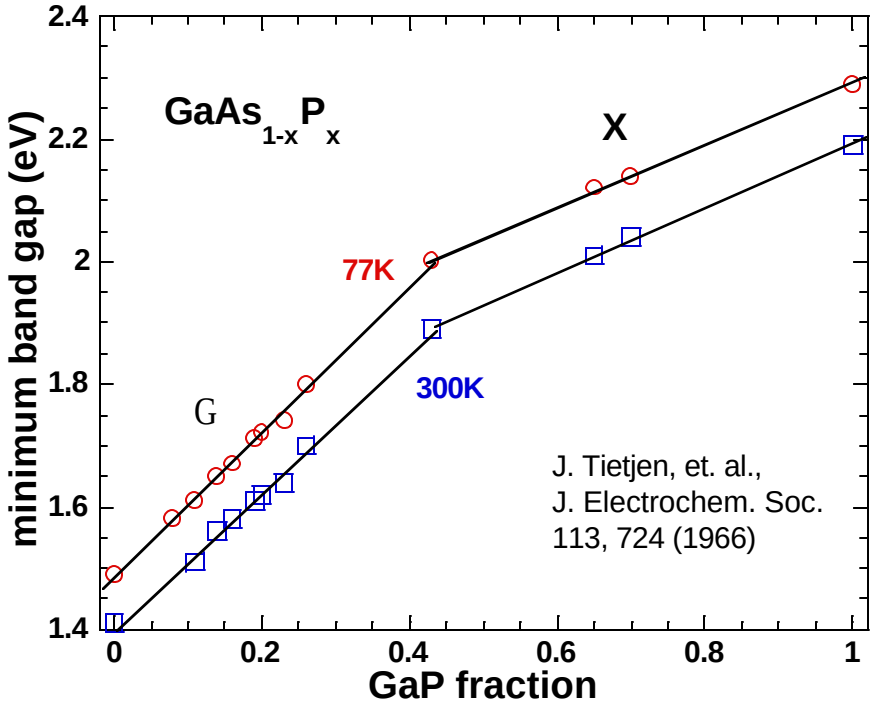


Fig.3.2 The minimum bandgap of GaAsP as a function of GaP fraction [15].

In contrast to the behavior of GaAsP, the composition dependence of highly mismatched alloys is expected to be very different. GaAsN is an example of such highly mismatched alloy. Some experimental results for these materials will be presented in the next section.

## 3.2 Experimental results of $GaAs_{1-x}N_x$ and $In_yGa_{1-y}As_{1-x}N_x$: Properties of HMA's

Most of the experimental studies of semiconductor alloy systems have been restricted to the cases where there are only small electronegativity differences between the end-point semiconductor materials. Properties of such lightly-mismatched alloys are close to the VCA predictions. In contrast, the properties of "highly mismatched" alloys (HMA's) deviate drastically from the linear predictions of the VCA. The most prominent class of HMA's comprises the III-$V_{1-x}$-$N_x$ alloys, in which electronegative nitrogen substitutes group V anions in standard group III-V compounds. The electronegativity difference between N and As is as large as 1.0 eV.

One of the striking effects of nitrogen incorporation into III-V semiconductors is a dramatic reduction in the fundamental band gap. A band gap reduction of more than 180 meV has been observed in $GaAs_{1-x}N_x$ alloys with only 1% N [16, 17]. Similar effects have been also observed in $GaP_{1-x}N_x$ [5], $InP_{1-x}N_x$ [7], $GaSb_yAs_{1-x-y}N_x$ [18] and $InSb_{1-x}N_x$ [19] alloys. The large band gap bowing and the lower-than-usual band gap pressure dependence have been found also in group II-VI HMA's such as $ZnS_{1-x}Te_x$ and $ZnSe_{1-x}Te_x$ [20], where electronegative S or Se substitutes metallic Te atoms.

The composition dependence of the bandgap of GaAsN is shown in Fig.3.3 [21-24]. In stark contrast to Fig.3.2, the dependence deviates significantly from the VCA prediction. Even the trend of the change in the bandgap is reversed from the VCA dependence on the As-rich side. While the VCA predicts a slight increase in the bandgap, it is observed the bandgap energy dropping rapidly as a function of N concentration. If the dependence is expressed with the band bowing equation Eq.(1.1), a huge bowing

parameter of more than 14 eV is required to accommodate this strong composition dependence on the As-rich side.

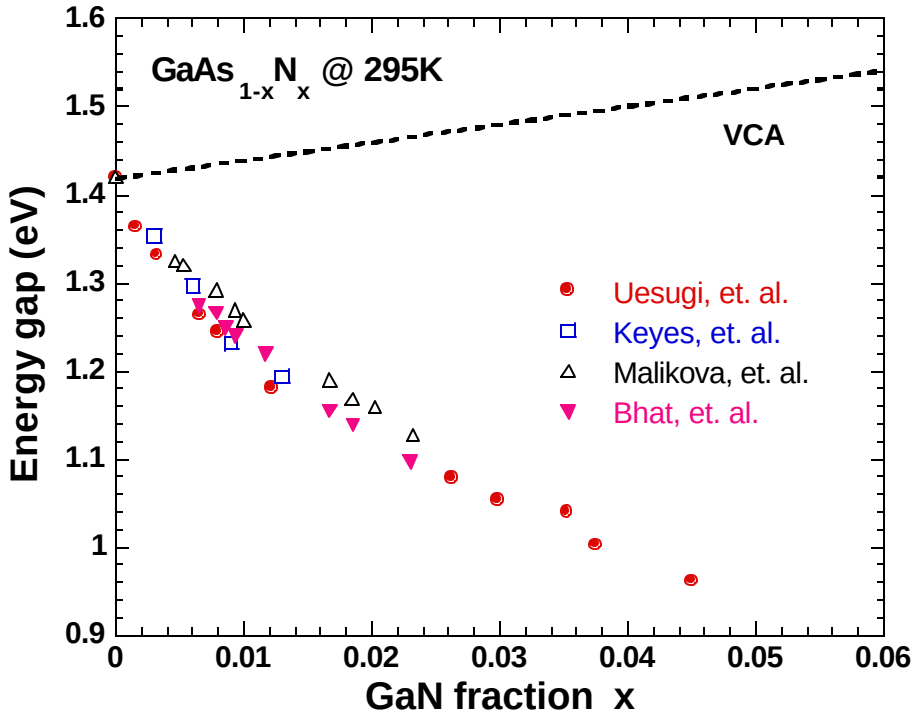


Fig.3.3 Measured bandgap of GaAsN as a function of GaN fraction [21-24].

## 3.3 Band Restructuring: Many-impurity Anderson Model in the Coherent Potential Approximation

### 3.3.1 Background

Over the past several decades, the physics of randomly disordered crystals has been studied extensively. An especially intense effort has been directed towards understanding of the electronic structure of random semiconductor alloys. The simplest treatments of such alloys is based on the Virtual Crystal Approximation [1, 2]. As stated earlier, in this approximation the electronic properties of the alloys are given by the linear interpolation between the properties of the end-point materials. The alloy disorder effects are typically included through a bowing parameter that describes the deviations from the VCA. The description of the composition dependence of the band gap in terms of the bowing parameter has been commonly used for a large variety of semiconductor alloys. It should be emphasized, however, that this approximation is expected to work reasonably well only for systems with bowing parameters much smaller than the energy gap.

In contrast, the bowing parameter of HMA's can be significantly larger than the bandgap energy, as exemplified in section 3.2. In this case the alloy disorder effects cannot account for the large deviation of the electronic properties from the VCA predictions. The first attempts to explain these unusual behaviors were based on a dielectric model that predicted highly nonlinear composition dependencies of the band gap for the alloys of semiconductor compounds with very different properties [25]. The model predicted a semiconductor to semi-metal transition in some of the alloys [26]. The

large band gap reduction in $GaN_xAs_{1-x}$ alloys has also been explained by Wei and Zunger [27] in terms of a large composition dependent bowing parameter that could be decomposed into three different contributions: a volume deformation, a charge exchange and a structural relaxation. In the meantime, this approach has been abandoned, and several other theoretical explanations of the large band gap reduction in III-V-N alloys have been proposed [28-32].

Alternatively, the energy band structure of HMA's has been explained in terms of the two-level Band Anticrossing (BAC) model [20, 33, 34]. The model accurately describes the composition and pressure dependencies of the fundamental band gaps of HMA's. Furthermore, it has been used to predict several new effects such as a N-induced enhancement of the electron effective mass [35-36] and an increase in the donor activation efficiency [37] in $In_yGa_{1-y}As_{1-x}N_x$ alloys, and the change in the nature of the fundamental band gap from indirect to direct in $GaP_{1-x}N_x$ [6]. All these predictions have now been experimentally confirmed.

In the BAC model, the restructuring of the conduction band is a result of an anticrossing interaction between highly localized $A_1$ states of the substitutional N atoms and the extended states of the host semiconductor matrix. The interaction between these two types of states has been treated in the simplest possible manner in analogy to the perturbation theory of a degenerate two-level system. More recently, it has been demonstrated that the BAC model can be derived from a firmer theoretical base [38]. It is the direct result of the many-impurity Anderson model, which has been widely used to treat the interaction between impurity states and band states [39].

The original Anderson model was developed to describe a single impurity atom of a transition metal or a rare-earth element in a non-magnetic metal. In Anderson's *s-d* exchange model [39], the electron system is separated into a delocalized part of the matrix metal, which is described in terms of the band theory, and a localized level of the *d* shell electrons of the transition metal impurity atom. A dynamical mixing term is introduced into the Hamiltonian of the system to describe the hybridization between the band states and the localized impurity states. Solving the Anderson Hamiltonian, it has been found that, as a result of the hybridization, the impurity *d* state becomes a virtual energy state with an imaginary energy part proportional to the strength of the *s-d* hybridization. The imaginary part of the eigen-energy of the virtual state defines the width of the density distribution of the *d* state, and determines the lifetime of the state before the *d* electrons are delocalized into the band states through the exchange interaction. Self-consistent calculations were performed to find the conditions for the existence of localized magnetic moments.

The single impurity Anderson model has been extended to explain the properties of cerium-based heavy-Fermion systems. A periodic coherent Anderson model has been developed and investigated over the years to accommodate both the spatial periodicity and the localization of the 4*f* orbitals in these systems [40, 41]. The energy dispersion of the system is restructured into two subbands, a result of the hybridization between the localized orbitals and the band states. The newly-created indirect gap between the subbands has profound effects on the electrical and thermodynamical properties of the system [42].

A many-impurity Anderson model has been proposed to describe the electronic properties of semiconductor crystals with low concentrations of deep-level transition-metal impurities [43, 44]. Unlike ordinary hydrogenic impurity states in semiconductors, these impurity states are characterized by two independent parameters: the spatial extent of their wave function and their energy level with respect to the nearest band edge of the host. The phase diagram for the electronic properties of crystals with such impurities is much richer than for the simple hydrogenic impurities. For example, as the impurity concentration increases, in addition to the trend of the conductivity increasing as a result of the Mott transition [45], hybridization between the impurity states and the band states of the host can suppress considerably the conductivity of the system in the form of inter-state electron scattering. Therefore, transport properties of the crystal are diversified by the competition between these two opposing processes.

In the following sections, we use the many-impurity Anderson model to evaluate the interaction between the randomly distributed localized states and the extended states in HMA's. We solve this problem within the single-site coherent potential approximation (CPA). The calculations reproduce the BAC model results for the restructuring of the conduction band. The imaginary part of the Green's function also yields new information on the electronic level broadening that is used to determine the broadening of the optical transitions and to calculate the free electron mobility.

3.3.2 Hamiltonian and Green's Function Approach

We describe the electronic structure of HMA's (*e.g.*, $GaAs_{1-x}N_x$) by considering an interaction between the localized and extended states within the many-impurity Anderson model. The total Hamiltonian of the system is the sum of three terms [43, 44],

$$H = \sum_{\boldsymbol{k}} E_{\boldsymbol{k}}^{c} c_{\boldsymbol{k}}^{+} c_{\boldsymbol{k}} + \sum_{\boldsymbol{j}} E_{\boldsymbol{j}}^{d} d_{\boldsymbol{j}}^{+} d_{\boldsymbol{j}} + \frac{1}{\sqrt{N}} \sum_{\boldsymbol{j},\boldsymbol{k}} (e^{i\boldsymbol{k}\cdot\boldsymbol{j}} V_{\boldsymbol{kj}} c_{\boldsymbol{k}}^{+} d_{\boldsymbol{j}} + h.c.), \qquad (3.1)$$

where the first term is the Hamiltonian of the electrons in the band states with energy dispersion $E_{\boldsymbol{k}}^{c}$. In the case of $GaAs_{1-x}N_x$, this is the $G_1$ conduction band near the Brillouin zone center. The second term corresponds to the energy of the electron localized on the $j$th impurity site with energy $E_{\boldsymbol{j}}^{d}$. To simplify the expressions, we use a vector $\boldsymbol{j}$ to denote the 3-dimentional coordinates of the $j$th site. The third term describes the change in the single electron energy due to the dynamical mixing between the band states and the localized states. $N$ is the number of primitive cells in the crystal. It is assumed that only one band and one impurity level are involved in the process. Following Anderson's scheme, the hybridization strength is characterized by the parameter $V_{\boldsymbol{kj}}$ defined by the following equation [39],

$$\begin{aligned} \langle \boldsymbol{k} | H_{HF} | d \rangle &= \frac{1}{\sqrt{N}} \sum_{\boldsymbol{l},\boldsymbol{j}} e^{i\boldsymbol{k}\cdot\boldsymbol{l}} \int a^{*}(\boldsymbol{r}-\boldsymbol{l}) H_{HF}(\boldsymbol{r}) j_{d}(\boldsymbol{r}-\boldsymbol{j}) d\boldsymbol{r} \\ &= \frac{1}{\sqrt{N}} \sum_{\boldsymbol{j}} e^{i\boldsymbol{k}\cdot\boldsymbol{j}} \cdot \sum_{\boldsymbol{l}} e^{i\boldsymbol{k}(\boldsymbol{l}-\boldsymbol{j})} \int a^{*}(\boldsymbol{r}-\boldsymbol{l}) H_{HF}(\boldsymbol{r}) j_{d}(\boldsymbol{r}-\boldsymbol{j}) d\boldsymbol{r} \qquad (3.2) \\ &\equiv \frac{1}{\sqrt{N}} \sum_{\boldsymbol{j}} e^{i\boldsymbol{k}\cdot\boldsymbol{j}} V_{\boldsymbol{kj}}, \end{aligned}$$

where $a(\boldsymbol{r}-\boldsymbol{j})$ and $j_d(\boldsymbol{r}-\boldsymbol{j})$ are the Wannier functions belonging to the band and the localized wavefunction of the impurity on the $j$th site, respectively. $H_{HF}(\boldsymbol{r})$ is the single electron energy described in the Hartree-Fock approximation [39].

The retarded double-time Green's function for band electrons is defined as

$$G(t) \equiv << c(t) \mid c^{+}(0) >>= -\frac{i}{\hbar} q(t) < \left[c(t), c^{+}(0)\right]_{+} >, \tag{3.3}$$

where $q(t)$ is the step function, $A(t) \equiv e^{iHt} A e^{-iHt}$, $[A,B]_{+} = AB + BA$ is the Fermi anticommutator, and $< A >= Tr\left(Ae^{-H/kT}\right)/Tr\left(e^{-H/kT}\right)$ represents the ensemble average.

The Fourier transform of Eq.(3.3) is

$$G(E) \equiv << c \mid c^{+} >>= \int_{-\infty}^{\infty} G(t) e^{i\left(E+i0^{+}\right)t/\hbar} dt, \tag{3.4a}$$

and

$$G(t) = \frac{1}{2p\hbar} \int_{-\infty}^{\infty} G(E) e^{-i\left(E+i0^{+}\right)t/\hbar} dE. \tag{3.4b}$$

From the Heisenberg equation

$$i\hbar \frac{d}{dt} A(t) = [A(t), H] = A(t)H - HA(t), \tag{3.5}$$

the equation of motion of the Green's function $G(t)$ can be written,

$$i\hbar \frac{d}{dt} << c(t) \mid c^{+}(0) >>= d(t) < \left[c(t), c^{+}(0)\right]_{+} > + << [c(t), H] \mid c^{+}(0) >> . \tag{3.6}$$

The corresponding equation of motion of $G(E)$ is obtained from the Fourier transform of Eq.(3.6) [46-47],

$$E << c_{\boldsymbol{k}} \mid c_{\boldsymbol{k}'}^{+} >>=< \left[c_{\boldsymbol{k}}, c_{\boldsymbol{k}'}^{+}\right]_{+} > + << \left[c_{\boldsymbol{k}}, H\right] \mid c_{\boldsymbol{k}'}^{+} >> . \tag{3.7}$$

Because of the commutation relation $\left[c_{\boldsymbol{k}}^{+}, c_{\boldsymbol{k}'}\right]_{+} = \delta_{\boldsymbol{k},\boldsymbol{k}'}$, Eq.(3.7) leads to

$$G_{\boldsymbol{k}\boldsymbol{k}'} = \delta_{\boldsymbol{k}\boldsymbol{k}'} G_{\boldsymbol{k}\boldsymbol{k}}^{(0)} + \frac{1}{\sqrt{N}} G_{\boldsymbol{k}\boldsymbol{k}}^{(0)} \sum_{j} V_{\boldsymbol{k}j} e^{i\boldsymbol{k}j} F_{\boldsymbol{j}\boldsymbol{k}'}, \tag{3.8}$$

where the coupling Green's function is defined as $F_{\boldsymbol{j}\boldsymbol{k}'} \equiv \ll d_{\boldsymbol{j}} \mid c_{\boldsymbol{k}'}^{+} \gg$ and has the following equation of motion,

$$F_{\boldsymbol{j}\boldsymbol{k}'} = H_{\boldsymbol{j}\boldsymbol{j}}^{(0)} \frac{1}{\sqrt{N}} \sum_{\boldsymbol{k}''} V_{\boldsymbol{k}''j} e^{-i\boldsymbol{k}''j} G_{\boldsymbol{k}''\boldsymbol{k}'}. \tag{3.9}$$

In Eq.(3.8) and (3.9), the unperturbed retarded Green's functions are

$$G_{\boldsymbol{k}\boldsymbol{k}'}^{(0)} = \delta_{\boldsymbol{k}\boldsymbol{k}'} \left(E - E_{\boldsymbol{k}}^{c} + i0^{+}\right)^{-1}, \qquad H_{\boldsymbol{j}\boldsymbol{j}'}^{(0)} = \delta_{\boldsymbol{j}\boldsymbol{j}'} \left(E - E_{\boldsymbol{j}}^{d} + i0^{+}\right)^{-1}. \tag{3.10}$$

The Green's function for the impurity atoms is defined by $H_{\boldsymbol{j}\boldsymbol{j}'} \equiv \ll d_{\boldsymbol{j}} \mid d_{\boldsymbol{j}'}^{+} \gg$.

Eq.(3.8) and (3.9) yield an integral equation for $G_{\boldsymbol{k}\boldsymbol{k}'}$ of the form

$$G_{\boldsymbol{k}\boldsymbol{k}'} = \delta_{\boldsymbol{k}\boldsymbol{k}'} G_{\boldsymbol{k}\boldsymbol{k}}^{(0)} + \frac{1}{N} G_{\boldsymbol{k}\boldsymbol{k}}^{(0)} \sum_{\boldsymbol{k}''\boldsymbol{j}} \tilde{V} \cdot e^{i(\boldsymbol{k}-\boldsymbol{k}'')\cdot\boldsymbol{j}} G_{\boldsymbol{k}''\boldsymbol{k}'}, \tag{3.11}$$

where the renormalized interaction parameter is given by

$$\tilde{V} = V_{\boldsymbol{k}\boldsymbol{j}} \cdot V_{\boldsymbol{k}''\boldsymbol{j}} \Big/ \left(E - E_{\boldsymbol{j}}^{d}\right) \approx V^{2} \Big/ \left(E - E_{\boldsymbol{j}}^{d}\right), \tag{3.12}$$

In Eq.(3.12), $V$ is the average value of $V_{\boldsymbol{k}\boldsymbol{j}}$, assuming weak dependencies on $\boldsymbol{k}$ and $\boldsymbol{j}$.

For the single impurity case, we can set $\boldsymbol{j}$=0. The equation chain represented by Eq.(3.11) is closed and has the following solution,

$$G_{\boldsymbol{k}\boldsymbol{k}'} = \delta_{\boldsymbol{k}\boldsymbol{k}'} G_{\boldsymbol{k}\boldsymbol{k}}^{(0)} + \frac{\tilde{V}}{N} G_{\boldsymbol{k}\boldsymbol{k}}^{(0)} G_{\boldsymbol{k}'\boldsymbol{k}'}^{(0)} \left[1 - \frac{\tilde{V}}{N} \sum_{\boldsymbol{k}''} G_{\boldsymbol{k}''\boldsymbol{k}''}^{(0)}\right]^{-1}. \tag{3.13}$$

Meanwhile,

$$\sum_{\boldsymbol{k}''} G^{(0)}_{\boldsymbol{k}''\boldsymbol{k}''} = \sum_{\boldsymbol{k}''} \frac{1}{E - E^c_{\boldsymbol{k}''} + i0^+} = N \int_{BZ} \frac{r_0(e)}{E - e + i0^+} de$$
$$= N\left\{ P\int \frac{r_0(e)}{E-e} de + ipbr_0\left(E^d\right)\right\} \qquad (3.14)$$
$$\equiv R + iNpbr_0\left(E^d\right) \approx ipbNr_0\left(E^d\right),$$

where $r_0(e)$ is the density of states (DOS) of $E_{\boldsymbol{k}}{}^c$ per unit cell. $P\int$ represents the principal value of the integral and is usually very small if $r_0(e)$ does not change rapidly near $E^d$. $R$ is the real part of the integration and is small, so that it will be neglected in the following discussions. Even if $R$ is not negligible, it can be taken into account by including a shift to $E^d$, and the main conclusion of this theory is not affected. Since $r_0(e)$ depends only weakly on energy, we can assume that it is constant in first order approximation of the imaginary part calculation, with an effective value equal to the unperturbed DOS evaluated at $E^d$ and multiplied by a prefactor $b$.

The poles of Eq.(3.13) give the dispersion relations for the system,

$$E = \begin{cases} E^c_{\boldsymbol{k}}; \\ E^d + V^2 R + ipbV^2 r_0(E) \approx E^d + ipbV^2 r_0\left(E^d\right). \end{cases} \qquad (3.15)$$

This is the original Anderson localization model for magnetic impurities in metals. It shows that the band state energy is unaffected, but the energy of the localized state gains an imaginary part, implying that the DOS of the localized state is broadened by the dynamical mixing.

In the case of $x$ = 1, there is one localized state in each unit cell. The model then becomes a "periodic Anderson model", which applies to heavy fermion system [40, 41]. In this case the equation chain given by Eq. (3.11) is also closed and takes a form,

$$
\begin{aligned}
G_{\boldsymbol{k}\boldsymbol{k}'} &= d_{\boldsymbol{k}\boldsymbol{k}'} G^{(0)}_{\boldsymbol{k}\boldsymbol{k}} + \frac{1}{N} G^{(0)}_{\boldsymbol{k}\boldsymbol{k}} \tilde{V} \sum_{\boldsymbol{k}''\boldsymbol{j}} e^{i(\boldsymbol{k}-\boldsymbol{k}'')\boldsymbol{j}} G_{\boldsymbol{k}''\boldsymbol{k}'} \\
&= d_{\boldsymbol{k}\boldsymbol{k}'} G^{(0)}_{\boldsymbol{k}\boldsymbol{k}} + G^{(0)}_{\boldsymbol{k}\boldsymbol{k}} \tilde{V} \sum_{\boldsymbol{k}''} d_{\boldsymbol{k}''\boldsymbol{k}} G_{\boldsymbol{k}''\boldsymbol{k}'} \\
&= d_{\boldsymbol{k}\boldsymbol{k}'} G^{(0)}_{\boldsymbol{k}\boldsymbol{k}} \left[1 - \tilde{V} G^{(0)}_{\boldsymbol{k}\boldsymbol{k}}\right]^{-1}.
\end{aligned}
\tag{3.16}
$$

Combined with Eq.(3.10) and (3.12), the Green's function given by Eq.(3.16) has poles given by,

$$
\left(E - E^{c}_{\boldsymbol{k}}\right) \cdot \left(E - E^{d}\right) = V^{2}, \tag{3.17}
$$

which shows a spectrum restructuring [40,41]. The dispersion relations $E_{\boldsymbol{k}}{}^{c}$ and $E^{d}$ anticross each other and result in two new dispersions, *i.e.*, the algebraic solutions of Eq.(3.17).

### 3.3.3 Coherent Potential Approximation

For concentrations between 0 and 1, $0<x<1$, the summation in Eq. (3.1) extends over $x \cdot N$ sites that are occupied by impurities. This situation corresponds to the so-called "many-impurity Anderson model". The equation chain Eq.(3.11) is not closed and approximation is needed for a solution.

We perform the Fourier transform of Eq.(3.11), and obtain the equation of the Green's function in real space representation,

$$
\begin{aligned}
G_{ll'} &\equiv \frac{1}{N}\sum_{kk'} e^{-ikl+ik'l'} G_{kk'} \\
&= G^{(0)}_{ll'} + \frac{1}{N^2}\sum_{kk'}\sum_{k''}\sum_{j} e^{-ikl+ik'l'} e^{ikj-ik''j} \tilde{V} G^{(0)}_{kk} G_{k''k'} \\
&= G^{(0)}_{ll'} + \frac{1}{N}\sum_{k'k''}\sum_{j} e^{ik'l'} e^{-ik''j} \tilde{V} G^{(0)}_{lj} G_{k''k'} \\
&= G^{(0)}_{ll'} + \sum_{j} G^{(0)}_{lj} \tilde{V} G_{jl'}.
\end{aligned}
\tag{3.18}
$$

In matrix form, Eq.(3.18) is written as the Dyson equation,

$$
\begin{aligned}
G &= G^{(0)} + G^{(0)} \cdot \tilde{v} \cdot G \\
&= G^{(0)} + G^{(0)} \cdot \tilde{v} \cdot G^{(0)} + G^{(0)} \cdot \tilde{v} \cdot G^{(0)} \cdot \tilde{v} \cdot G^{(0)} + ...,
\end{aligned}
\tag{3.19}
$$

where $(\tilde{v})_{ll'} = p_l \tilde{V} d_{ll'}$ is the effective perturbation matrix. $p_l$ = 1 if the $l$-th site is occupied by an impurity atom, and $p_l$ = 0 otherwise.

In the dilute limit, $0<x<<1$, we assume that the impurities are distributed randomly and homogeneously in space. A configurational averaging can be carried out, neglecting correlations between positions of the impurities. In this case, the single-site coherent-potential-approximation (CPA) is adequate for the many-impurity system. In the CPA, consecutive multiple scattering from a single impurity atom is fully taken into account, but correlations between scattering from different impurity atoms are neglected due to the lack of coherence between the randomly distributed impurity sites. This approximation is illustrated by the following Feynman diagrams in Fig.3.4. We retain diagrams like (a), (b), (c), etc., but ignore (d), (e), (f), etc..

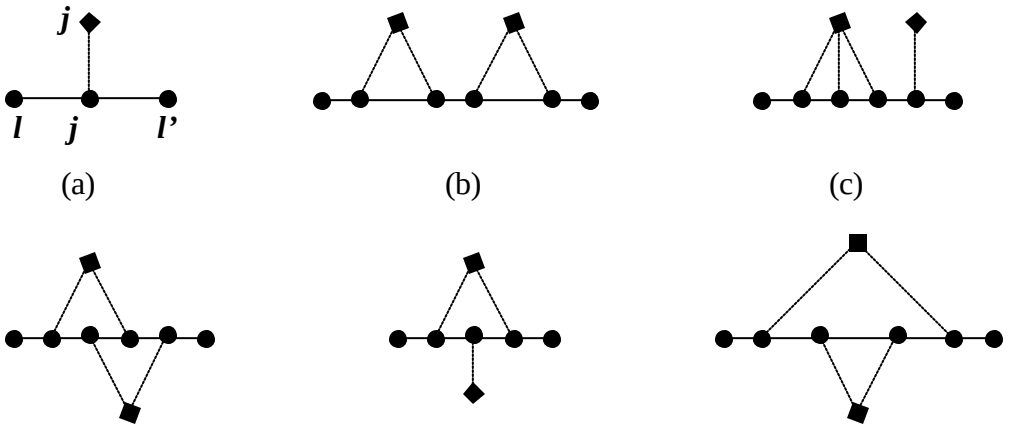


(a) (b) (c)

(d) (e) (f)

Fig.3.4 Feynman diagrams of the CPA. Each solid segment represents an unperturbed Green's function, and each dashed segment represents a scattering interaction.

The CPA treatment leads to the result that [43, 48, 49], after the configurational averaging, the average Green's function partially restores the space translational invariance, and ***k*** resumes its well-defined properties as a good quantum number. In momentum space, the diagonal Green's function in CPA can be written as [43, 48, 49]

$$G_{\boldsymbol{kk}}(E)=\left[E-E_{\boldsymbol{k}}^{c}-s(E)\right]^{-1}, \tag{3.20}$$

where the average self-energy is proportional to the impurity concentration,

$$s(E)=\frac{x\tilde{V}}{1-\left(\tilde{V}/N\right)\sum_{\boldsymbol{k}}G_{\boldsymbol{kk}}}\equiv\frac{x\tilde{V}}{1-\tilde{V}G(E)}. \tag{3.21}$$

The average Green's function in real space, $G(E)$, is determined by the self-consistency equation,

$$
\begin{aligned}
G(E) = G_{jj} = G_{j=0,0} &\equiv \frac{1}{N}\sum_{k\in BZ} G_{kk}(E) \\
&= \frac{1}{N}\sum_{k\in BZ} \frac{1}{E - E_k^c - x\tilde{V}/\left[1-\tilde{V}G(E)\right]} \\
&= \int_{BZ} \frac{r_0(e)de}{e - \left\{E - x\tilde{V}/\left[1-\tilde{V}G(E)\right]\right\}}.
\end{aligned}
\tag{3.22}
$$

The poles of the average Green's function determine the eigen-energies of the system. In the next section, the approximate solutions of Eq.(3.22) will be discussed.

## 3.4 Discussion and Comparison between Theory and Experiments

### 3.4.1 Simplified Representation: Two-level Band Anticrossing Model

In general, $G(E)$ can have an imaginary part, and the DOS for the conduction band in the entire Brillouin zone is rather complicated. Therefore, numerical calculations are needed to find the solution to the transcendental Eq.(3.22). Considering that, similar to the case of Eq.(3.14), the imaginary part of the denominator of the integrand in Eq.(3.22) is very small (proportional to a small number $x$), we can replace Eq.(3.22) by Eq.(3.14) as the lowest order approximation,

$$G(E) \approx P\int \frac{r_0(e)de}{e-E} + ipbr_0(E^d) \approx ipb?_0(E^d). \tag{3.23}$$

Equation (3.20) is then

$$\begin{aligned} G_{\boldsymbol{kk}}(E) &\approx \left[ E - E_{\boldsymbol{k}}^c - \frac{x\tilde{V}}{1-ipbr_0(E^d)\tilde{V}} \right]^{-1} \\ &= \left[ E - E_{\boldsymbol{k}}^c - \frac{V^2 x}{E - E^d - ipbV^2 r_0(E^d)} \right]^{-1} \\ &= \frac{E - \left(E^d + ipbV^2 r_0(E^d)\right)}{\left(E - E_k^c\right)\cdot\left[E - \left(E^d + ipbV^2 r_0(E^d)\right)\right] - V^2 x}. \end{aligned} \tag{3.24}$$

The new dispersion relations are determined by the poles of $G_{\boldsymbol{kk}}(E)$, and the solutions are given by an equivalent two-state-like eigen-value problem,

$$\begin{vmatrix} E_{\boldsymbol{k}}^c - E(\boldsymbol{k}) & V\sqrt{x} \\ V\sqrt{x} & E^d + i\Gamma_d - E(\boldsymbol{k}) \end{vmatrix} = 0, \tag{3.25}$$

where $\Gamma_d = pbV^2 r_0(E^d)$ is the broadening of $E^d$ in the single-impurity Anderson Model. If $\Gamma_d$=0, Eq.(3.25) is reduced to the BAC model [20, 33, 34] with two restructured dispersions for the upper and lower conduction subbands,

$$E_{\pm}(\boldsymbol{k}) = \frac{1}{2}\left\{\left(E_{\boldsymbol{k}}^c + E^d\right) \pm \sqrt{\left(E_{\boldsymbol{k}}^c - E^d\right)^2 + 4V^2 x}\right\}. \tag{3.26}$$

If the broadening $\Gamma_d$ is nonzero but small, so that $2V\sqrt{x} >> pbV^2 r_0(E^d)$ and $\left|E_{\boldsymbol{k}}^c - E^d\right| >> pbV^2 r_0(E^d)$, we obtain an approximate analytical solution for Eq.(3.25),

$$\tilde{E}_{\pm}(\boldsymbol{k}) \approx E_{\pm}(\boldsymbol{k}) + i\Gamma_d \frac{\left[E_{\pm}(\boldsymbol{k}) - E_{\boldsymbol{k}}^c\right]}{\left[E_{\pm}(\boldsymbol{k}) - E_{\boldsymbol{k}}^c\right] + \left[E_{\pm}(\boldsymbol{k}) - E^d\right]} \equiv E_{\pm}(\boldsymbol{k}) + i\Gamma_{\pm}(\boldsymbol{k}), \tag{3.27}$$

where $E_{\pm}(\boldsymbol{k})$ has been defined in Eq.(3.26). The imaginary part of the dispersion relations defines the hybridization-induced uncertainty of the energy. We note that the imaginary part in Eq.(3.27) is proportional to the admixture of the localized states to the restructured wavefunctions in the two-state-like-perturbation picture described by Eq.(3.25),

$$\Gamma_{\pm}(\boldsymbol{k}) = \left|\langle d \,|\, E_{\pm}(\boldsymbol{k})\rangle\right|^2 \cdot \Gamma_d. \tag{3.28}$$

As an example, Fig.3.5(a) shows the dispersion relations given by Eq.(3.27) for $GaAs_{0.995}N_{0.005}$ near the Brillouin zone center. The broadening of the dispersion relations is given by the imaginary part of Eq.(3.28). In the calculation, the hybridization parameter $V = 2.7\,\text{eV}$ is taken to be an experimentally-determined constant [20]. The density of states for the GaAs conduction band edge is assumed to have a parabolic form following the effective-mass theory,

$$r_0(e) = 4p\sqrt{e - E_0^c}\,/\,e_B^{3/2}, \tag{3.29}$$

where $e_B = \hbar^2 (2p/b)^2 / (2m^*)$ is of the order of the conduction band width. The lattice constant of the unit cell is $b$=5.65 Å, and $m^*$=0.067$m_0$ is the electron effective mass of GaAs. The prefactor $b$ is taken to be equal to 0.22, as will be estimated in a later section.

This anticrossing interaction between the localized states and the $\Gamma_1$ conduction band states which all have the same $A_1$ symmetry, is similar to the band anticrossing effect frequently seen in intrinsic semiconductors. Shown in Fig.3.5(b) is the band structure of pure GaAs on a large energy scale over the whole Brillouin zone. A band anticrossing between two $\Gamma_5$-symmetry bands in intrinsic GaAs along the ? line is shown.

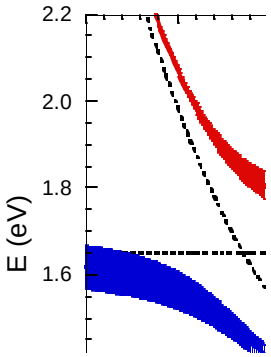


**(a)**

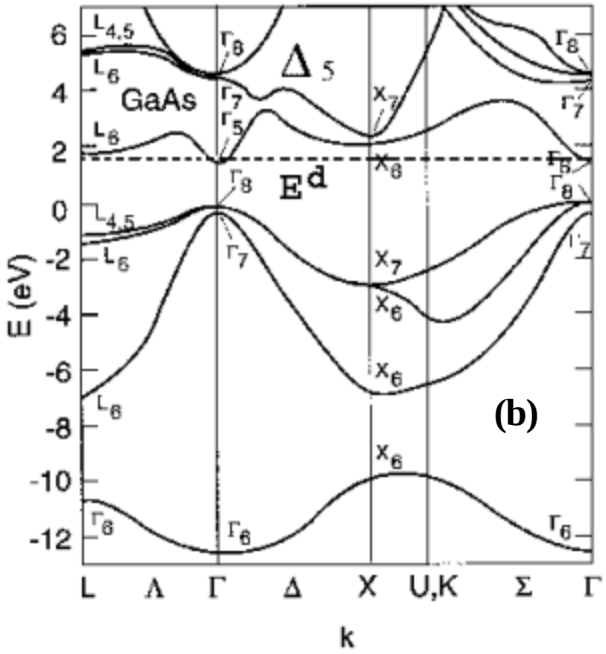


Fig.3.5 (a) Conduction band restructuring according to Eq.(3.27) for $GaAs_{0.995}N_{0.005}$. The broadening of the dispersion curves of the newly-formed subbands illustrates the energy uncertainties defined in Eq.(3.27). All the energies are referenced to the top of the valence band of GaAs. (b) The band structure of GaAs and the localized N level at $E^d$ (dashed line) over the whole Brillouin zone.

3.4.2 Comparison with Experimental Results: $GaAs_{1-x}N_x$, etc.

In this section the predictions of the BAC model are compared with some fundamental experimental results. The bandgap reduction in $GaAs_{1-x}N_x$ alloys is accounted for by the downward shift of the conduction band edge caused by the anticrossing interaction. Fig.3.6 shows the fundamental bandgap as a function of N concentration from various reports [21-24] together with the dependence calculated from Eq.(3.26). The best fit is obtained with an interaction constant of $V$=2.7eV.

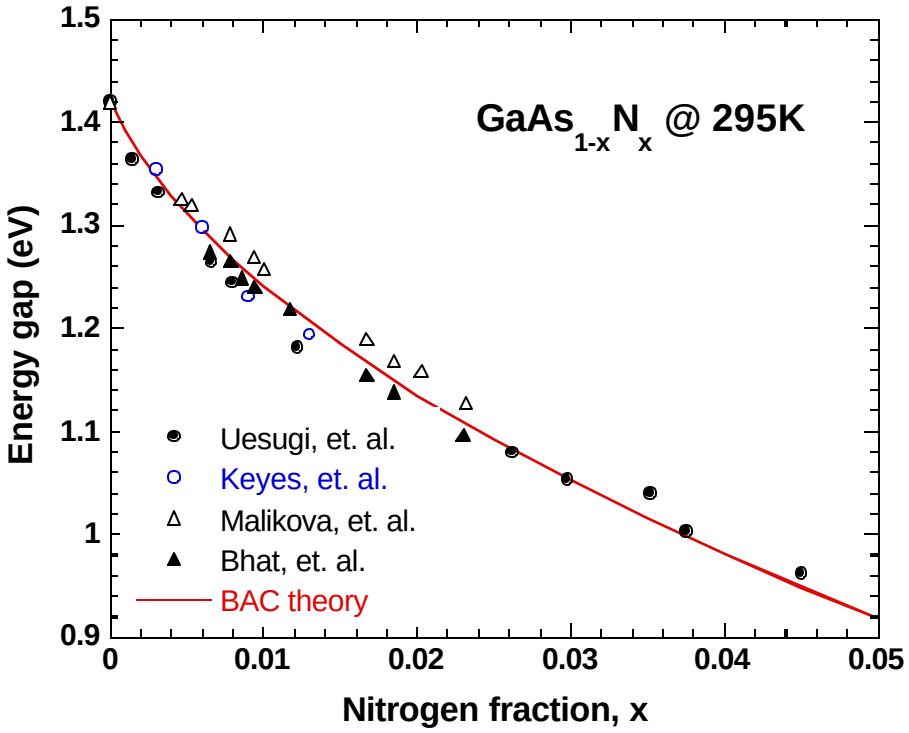


Fig.3.6 Energy gap of $GaAs_{1-x}N_x$ as a function of the N concentration from various reports [21-24]. The solid curve is a fit based on the BAC model.

The additional $E_+$ transition at energies blue-shifted from the previously observed N resonant level [31] suggests a strong interaction between the N states and the host GaAs. Fig.3.7(a) shows the photo-modulated reflectance (PR) spectra for $GaAs_{1-x}N_x$ for a range of N concentrations [50]. The critical energies are plotted as a function of $x$ in Fig.3.7(b). In Fig.3.7(b) it can be seen that the spin-orbit transition energy $E_- + \Delta_0$ follows $E_-$, indicating that the top of the valence band of GaAs is not affected by the N incorporation. The symmetric shift of $E_+$ and $E_-$ is a typical behavior for interacting two-level systems. On the other hand, the $E_1$ energy that corresponds to the inter-band transition along the ? line in the Brillouin zone shows a much weaker composition dependence. This implies that the effect of N on the band structure of GaAs away from the Brillouin zone center is much weaker.

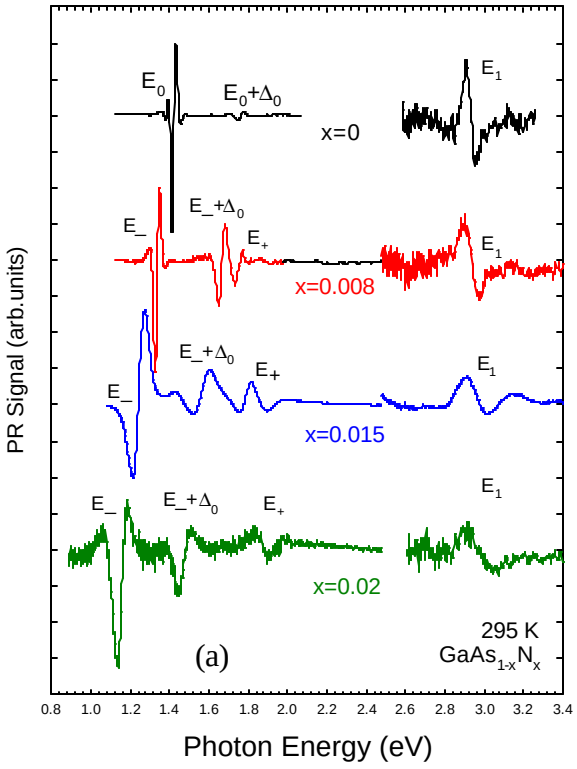


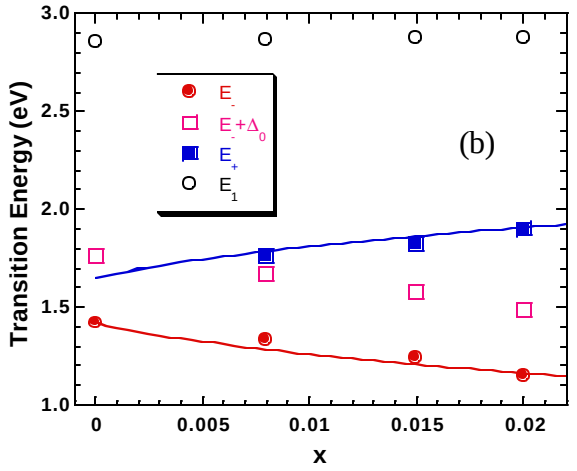


Fig.3.7(a) Photomodulated reflectance spectra showing the critical transitions [50]. (b) The critical energies obtained from (a) plotted as a function of *x*.

The anticrossing character of $E_+$ and $E_-$ is not only reflected in the composition dependence, but can also be seen in their pressure dependencies. Fig.3.8 shows the energy positions of the $E_+$ and $E_-$ transition for $GaAs_{0.985}N_{0.015}$ as a function of hydrostatic pressure [50]. The solid curves represent the pressure dependencies calculated from Eq.(3.26), using previously-known pressure coefficients $dE^C/dP = 10.8$ meV/kbar for the GaAs conduction band edge and $dE^d/dP = 1.5$ meV/kbar for the N localized states.

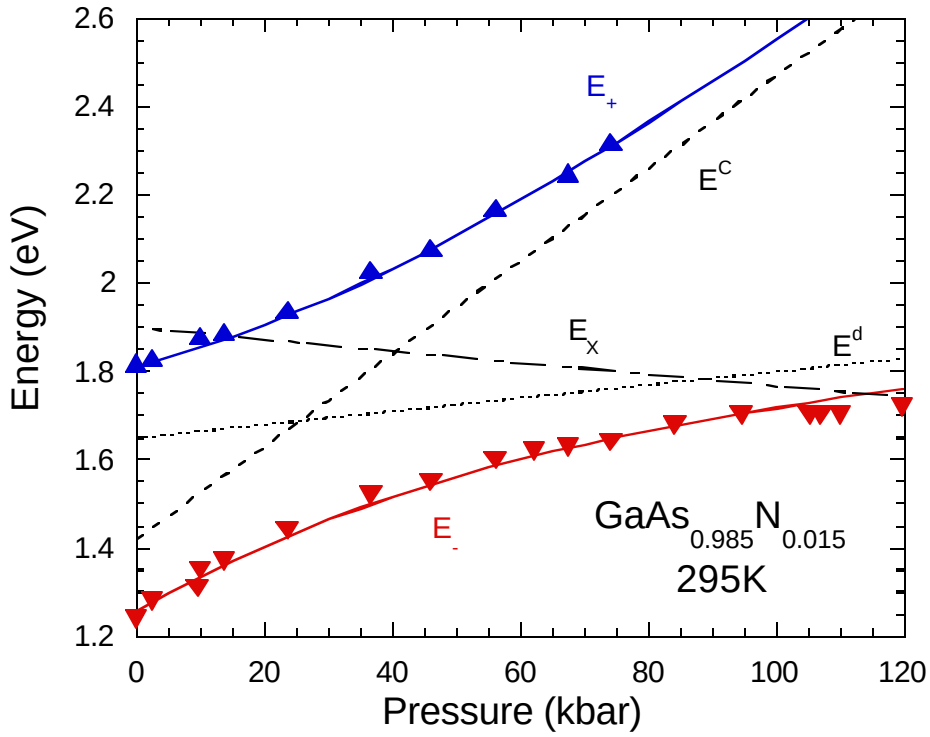


Fig.3.8 Energies of the $E_+$ and $E_-$ transitions obtained from PR experiments as a function of hydrostatic pressure for $GaAs_{0.985}N_{0.015}$ [50].

At present, growth of III-V-N alloys is considered challenging; bulk material has not been reported and most studies use epitaxial techniques such as gas-source molecular

beam epitaxy (MBE) or metal-organic chemical vapor deposition (MOCVD) to grow thin films. Because only a small concentration of N (~1%) can lead to a large modification in the energy band gap of III-V-N materials, ion implantation is an attractive and feasible alternative approach to synthesize these alloys. We have synthesized a series of III-V-N alloys [51] using ion implantation technique and their optical properties have been subsequently characterized. In the following text, the quaternary alloy $Al_yGa_{1-y}As_{1-x}N_x$ is discussed as an example.

As in the case of $GaAs_{1-x}N_x$, N incorporation in $Al_yGa_{1-y}As$ has also been observed to have similar effects. We have observed a significant N-induced reduction of the band gap in N-implanted $Al_yGa_{1-y}As$ thin films. For the implantation, $N^+$ ions were implanted into 0.3-0.5 μm $Al_yGa_{1-y}As$ epitaxial films MOCVD-grown on GaAs substrates with $y$ up to 0.61. Multiple N implants with energies in the range of 33 - 160 keV were used to create ~ 200-350 nm thick layers with a uniform N atomic fraction. Rapid thermal annealing was performed on the implanted samples in a flowing $N_2$ ambient over the temperature range of 560-950$^o$C for 5-120s. The samples were then optically investigated by PR spectroscopy. Positions of both the lower $E_-$ and upper $E_+$ subbands for $Al_yGa_{1-y}As_{1-x}N_x$ determined from the PR measurements are shown in Fig.3.9 as a function of AlAs mole fraction $y$. Note that the optical transitions to the indirect band gaps at L or X minima are not observed in the PR spectra. The known dependencies of the Γ, X, and L conduction-band minima on $y$ are also shown in the figure. The dependence of the localized nitrogen level $E_N$ on $y$ has been determined from published results on N-related photoluminescence lines in $Al_yGa_{1-y}As$ alloys doped with N at low concentrations [11, 52]: $E_N$=1.65+0.58 $y$ (eV) for the N level at room temperature. This dependence is shown

by the dotted line in Fig.3.9. It is worth noting that the change of $E_N$ by about 0.58 eV for $y$ changing from 0 to 1 is very close to the valence band offset between GaAs and AlAs, 0.55 eV. This indicates that the energy $E_N$ is practically constant independent of the AlGaAs alloy composition when referenced to an absolute energy scale, a characteristic feature of highly localized levels that has also been previously observed for the N level in GaAsP alloys [10], as has been discussed in Ch.2.

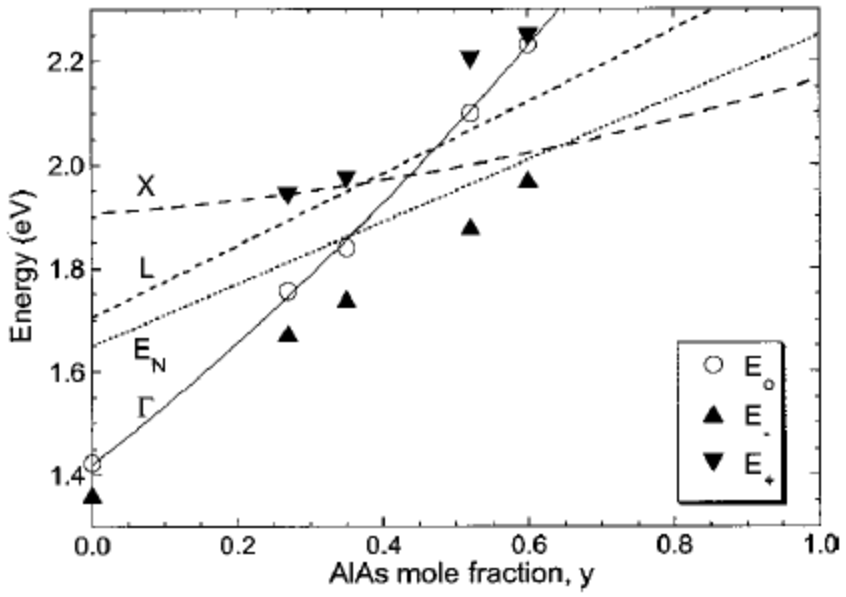


Fig.3.9 The $E_+$ and $E_-$ transition energies measured with ion beam synthesized $Al_yGa_{1-y}As_{1-x}N_x$ samples. The variation of $E_N$ and the Γ, X, and L conduction band edges as a function of AlAs mole fraction in $Al_yGa_{1-y}As$ alloys are also shown.

Results in Fig.3.9 show the evolution of the $E_-$ and $E_+$ energies as functions of the composition. The composition dependence of the relative locations of the interacting $E_N$ and Γ levels leads to a change in the nature of the $E_-$ and $E_+$ subbands. At larger $y$ the Γ

edge moves to higher energies and the $E_-$ subband acquires more Γ band-like character. This composition-induced evolution of the anticrossing interaction closely resembles a change in the nature of $E_-$ and $E_+$ states with hydrostatic pressure. The symmetric shift of $E_+$ and $E_-$ from the positions of $E_\Gamma$ and $E_N$ with increasing AlAs composition is another manifestation of the two-level anticrossing interaction in the system.

Similar band anticrossing effects have also been observed in several other N-containing III-V alloys, such as $GaP_{1-x}N_x$ [5], $InP_{1-x}N_x$ [7], $GaSb_yAs_{1-x-y}N_x$ [18] and $InSb_{1-x}N_x$ [19]. Shown in Fig.3.10 is the bandgap bowing of $InP_{1-x}N_x$ grown by gas-source molecular beam epitaxy with small N concentrations [53]. The energy of the localized N level $E^d$=2.0 eV above the valence band edge of InP was estimated from the valence band offset of 0.35 eV between InP and GaAs. A BAC fitting leads to a coupling constant of $V$=3.5 eV in $InP_{1-x}N_x$.

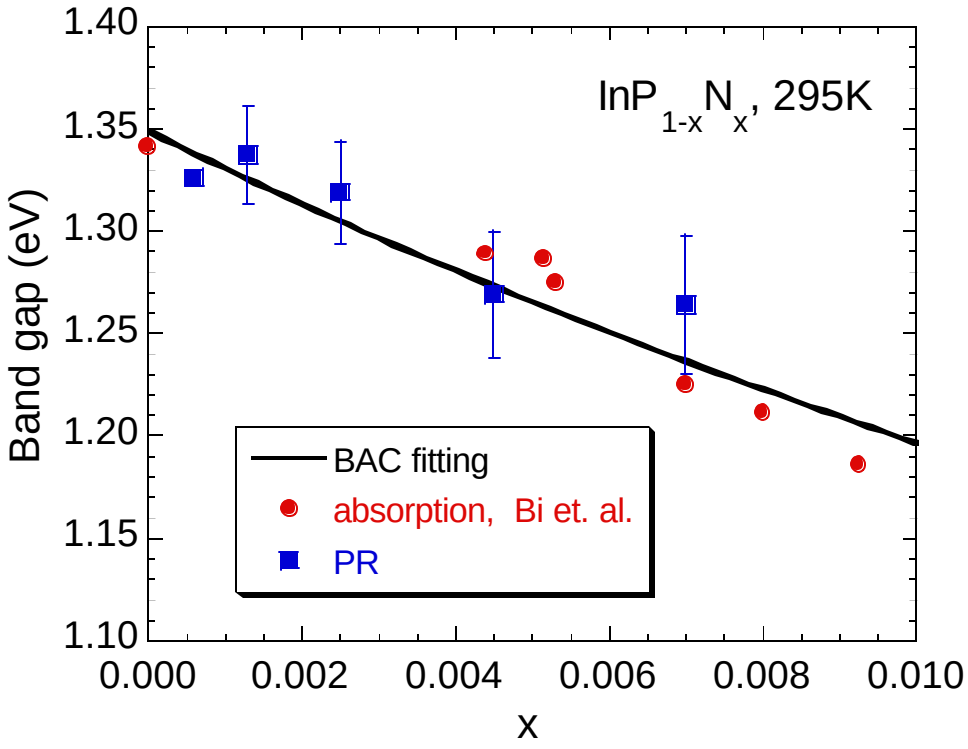


Fig.3.10 Energy gap of $InP_{1-x}N_x$ as a function of $x$. The solid line is a fit based on the BAC model.

The strong bandgap bowing is a characteristic of the localized-extended anticrossing effect in the system. This effect is frequently observed in III-V-N alloys because of the large electronegativity mismatch between N and the group V element it substitutes.

It is well known that large band gap bowings also exist in all group III-Sb alloys in which metallic Sb is replaced by either P or As. Given the moderate electronegativity difference between Sb and P or As, an interesting question arises: could the strong bowings also be explained by the band anticrossing interaction? Fig.3.11(a) shows the composition dependence of the energy of the conduction band edge in $GaAs_xSb_{1-x}$ [54]

and $InAs_ySb_{1-y}$ [55] along with the results of calculations based on the BAC model. The calculations account well for the conduction band shifts assuming that the energy of the localized As level lies at 1.6 eV above the valence band of GaSb and the coupling constant is 0.95 eV. The band anticrossing effects in these materials are significantly weaker compared with III-N-V alloys because of the smaller electronegativity difference of 0.2 eV between Sb and As.

Somewhat larger anticrossing effects are expected for III-V alloys in which Sb with an electronegativity of 1.8 eV is partially replaced by P with an electronegativity of 2.1 eV. Such alloys containing P and Sb are difficult to grow because of a large immiscibility between the components. A successful synthesis of $GaP_xSb_{1-x}$ has shown that this alloy system exhibits a large band gap bowing [56]. The energy of the conduction band edge as a function of the P content is shown in Fig.3.11(b). As expected, the anticrossing effects are more pronounced in this case than in the case of $GaAs_xSb_{1-x}$ or $InAs_ySb_{1-y}$ alloys. Note that there is quite a large deviation of the conduction band energy from the prediction of the VCA represented by $E_M$. Again, calculations based on the BAC model account very well for the downward shift of the conduction band edge.

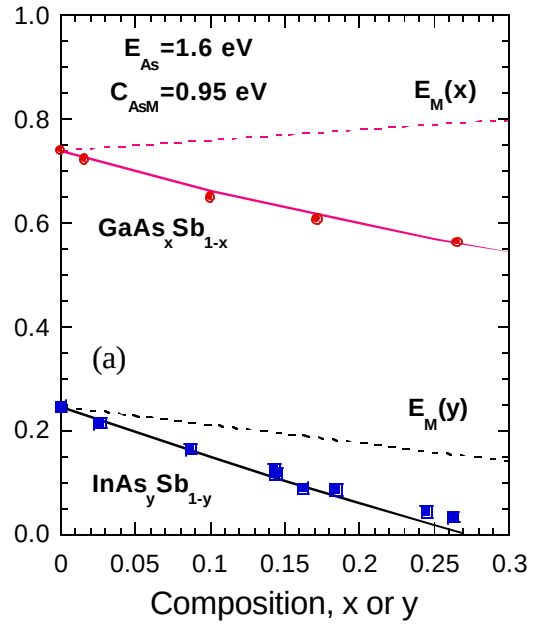


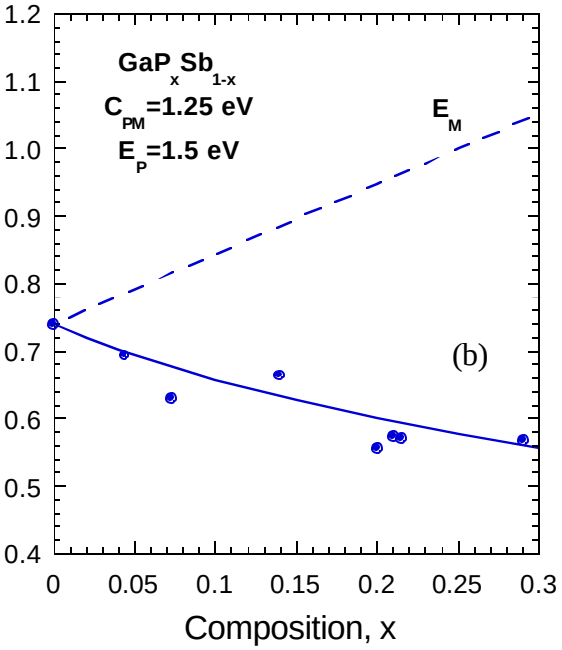


Fig.3.11(a) Energy of the conduction band edge in $GaAs_xSb_{1-x}$ and $InAs_ySb_{1-y}$. The energies are relative to the valence band maximum of GaSb [54, 55]. (b) Conduction band minimum as a function of composition in $GaP_xSb_{1-x}$. The solid line shows the results of BAC calculations with $E_M$ representing the conduction band edge obtained within the VCA [56].

### 3.4.3 $GaAs_{1-x}N_x$/GaAs Quantum Wells: Theory and Experiments

When semiconductor alloys form quantum wells (QW), the optical and the electronic transport properties can be changed significantly. The potential for important practical applications in high-efficiency optoelectronic devices clearly necessitates a good understanding of the electronic structure of the III-V-N based QW's. In this section, the results of studies of $GaAs_{1-x}N_x$/GaAs quantum superlattices will be shown. The Interband transitions in $GaAs_{1-x}N_x$/GaAs multiple QWs were studied at room temperature by PR spectroscopy as a function of well width, the nitrogen concentration, and hydrostatic pressure. It will be shown that all the experimental data can be explained quantitatively using the dispersion relationship obtained from the BAC model to calculate electron confinement effects in a finite depth quantum well.

A series of $GaAs_{1-x}N_x$/GaAs multiple QWs with different $GaAs_{1-x}N_x$ well thickness from 3 to 9 nm, N concentrations $0.012 < x < 0.028$, and 20 nm GaAs barriers were grown by gas-source molecular beam epitaxy on a semi-insulating GaAs substrate and capped by a 50 nm GaAs layer [57]. The QW structure is shown in Fig.3.12.

The PR spectra for GaAsN/GaAs QW's with 7 nm well width and four different N concentrations are shown in Fig.3.13(a).

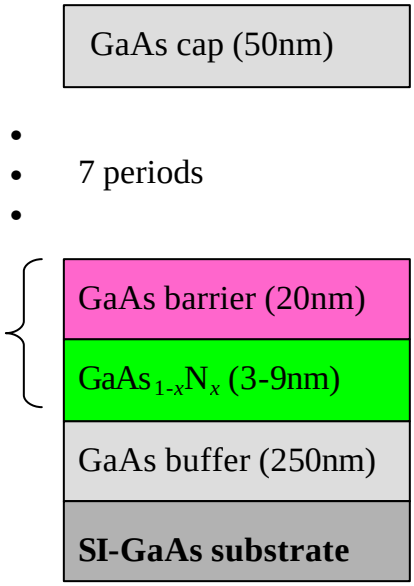


Fig.3.12 Structure of GaAsN/GaAs multiple QWs used in this study.

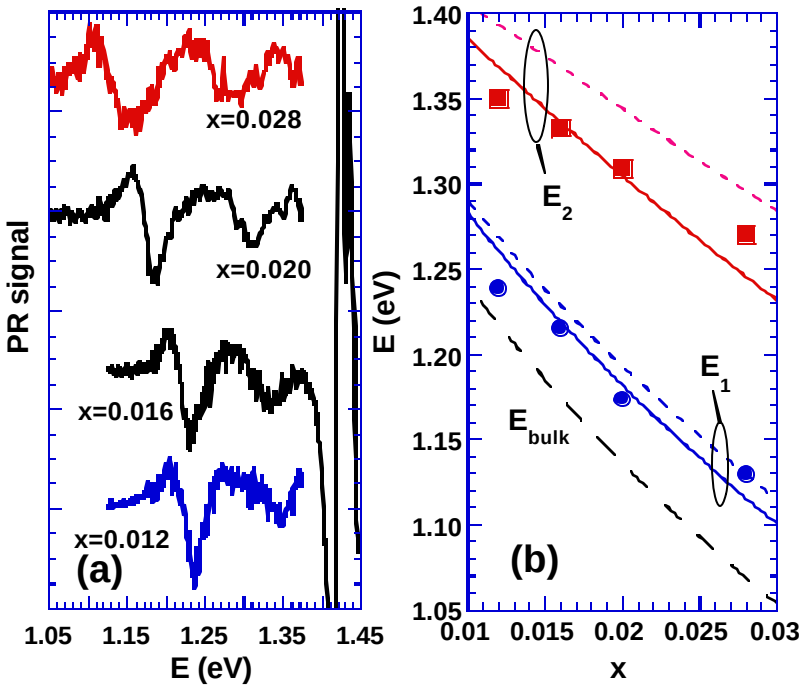


Fig. 3.13(a) Raw PR spectra taken at room temperature for $GaAs_{1-x}N_x$ / GaAs QW's with 7 nm well width and different N concentrations. (b) First and second transition energies $E_1$ and $E_2$ as a function of N concentration for the PR spectra shown in (a). Solid curves: calculated values using the band anticrossing (BAC) model and finite-depth single well confinement with $GaAs_{1-x}N_x$ electron effective mass given by Eq. (3.30); Short dashed curves: calculated values assuming $GaAs_{1-x}N_x$ electron effective mass equal to $m^*_{GaAs}$. Long dashed curve: band gap of bulk $GaAs_{1-x}N_x$ given by the BAC model.

The feature at 1.42 eV arises from the GaAs cap layer and barriers. Two transitions at lower energies are also clearly identified. We assign them to transitions from the GaAsN valence band to the two confined levels of the conduction band and denote them $E_1$ and $E_2$. These assignments are illustrated in Fig. 3.14. As shown in Fig. 3.13(b), the features corresponding to both transitions shift to lower energy with increasing $x$. The shifts can be attributed to the bandgap reduction observed in bulk

$GaAs_{1-x}N_x$ [34]. It should be noted that the data in Fig.3.13 and in Fig. 3.18 in the following text agree, within experimental error, with similar data presented in Ref. [58].

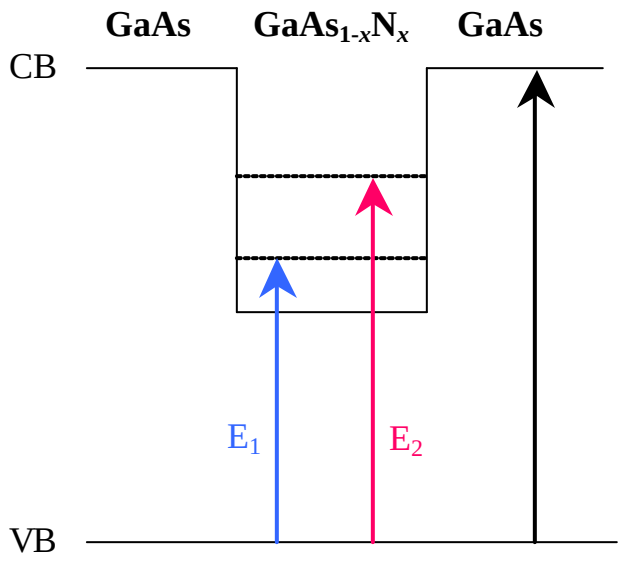


Fig.3.14 Band alignment and optical transitions in the QW.

In first order perturbation theory, the BAC model predicts a hybridized lowest conduction band given by Eq.(3.26). The GaAs conduction band near the Γ point can be represented well by a parabolic dispersion function with effective electron mass $m^*_{GaAs}=0.067\ m_0$. The band gap of bulk $GaAs_{1-x}N_x$ given by Eq. (3.26) is also plotted in Fig.3.13(b). It can be seen that the transitions in the QW's are blue shifted from the bulk energy gap due to quantum confinement.

To evaluate the confinement quantitatively, we applied a finite-depth square well confinement model with depth and width of the well and the effective mass inside ($m_{in}$) and outside ($m_{out}$) the well as input parameters. Since the barrier layer is much thicker than the active layer, we neglect the coupling between neighboring QW's and simplify

the system into a single QW problem. Furthermore, the electron dispersion given by Eq. (3.26) is non-parabolic; hence the electron effective mass in the conduction band is dependent on the ***k*** vector, resulting in an inseparable Schrödinger equation. To simplify the calculation, we have assumed that the effective mass of the electrons in the quantum well can be approximated by an energy-independent density-of-state mass at the bottom of the lowest conduction band [33, 59],

$$m^* \approx \hbar^2 \left| \frac{k}{dE_-(k)/dk} \right|_{k=0} = 2m^*_{GaAs} \Bigg/ \left[ 1 - \frac{E^c(0) - E^d}{\sqrt{\left(E^c(0) - E^d\right)^2 + 4V^2 x}} \right]. \qquad (3.30)$$

This is a good approximation, because as can be seen in Fig. 3.13, the confinement energies are below 0.2 eV, such that a change of the effective mass of less than 5% is estimated for the energy corresponding to the ground state confinement. Shown in Fig. 3.15 are the dispersion curves of $E_-(k)$ and the parabolic approximation assuming an electron effective mass given by Eq.(3.30). It can be seen that within the energy range of 0.2 eV from the $E_-$ bottom, the parabolic approximation mimics $E_-(k)$ quite well.

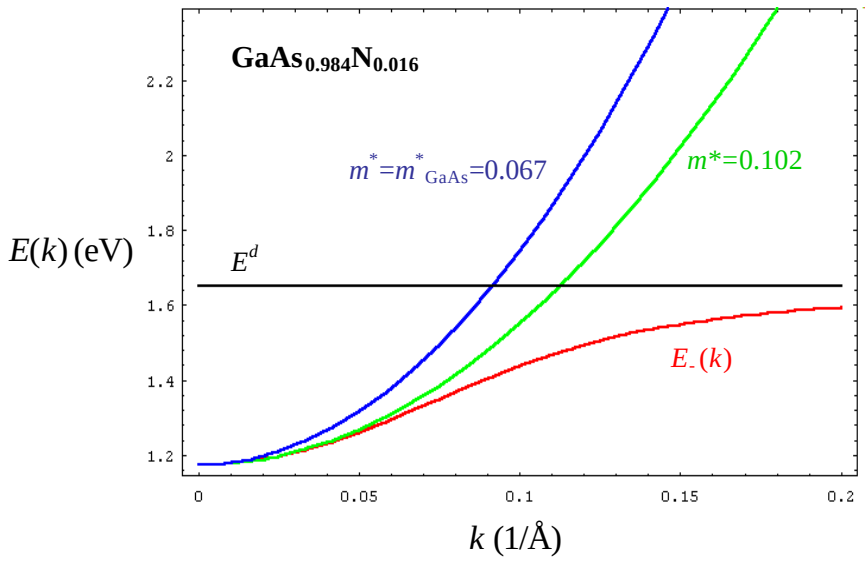


Fig.3.15 The dispersion relation of $E_-(k)$ for $x$=0.016, and the parabolic approximations to it near the band edge assuming different electron effective masses. Eq.(3.30) gives an effective mass of $m^* = 0.102$ for this N concentration.

Photoluminescence [60] and x-ray photoelectron spectroscopy [61] studies of $GaAs_{1-x}N_x$/GaAs heterostructures indicate a slightly type-II band lineup with a very small negative valence-band offset of $|DE_v| < 20$meV/%N. For this type-II band lineup, the transition energies are not sensitive to the value of the valence band offset, because the holes are not confined in the active well layer. Consequently, the lower states of the optical transitions in the well are always located at the top of the valence band, and the energies of the two observed transitions are given by the locations of the ground and first excited states of the confined conduction band electrons [60].

In the following discussion, we neglect the strain effect induced by the lattice mismatch between the $GaAs_{1-x}N_x$ layer and the GaAs layer. For x<0.03, the lattice constant of $GaAs_{1-x}N_x$ is changed from that of GaAs by less than 0.5% [62]. The biaxial

tensile strain introduced by this small mismatch may raise the valence band of $GaAs_{1-x}N_x$ by 40 meV at most [63]. The quantum confinement of the holes by this shallow well has been estimated to decrease the transition energies by less than 20 meV for all the QW's studied here. It is important to note that the small energy shifts resulting from the biaxial strain-induced hole confinement do not depend on the external hydrostatic pressure and are the same for all the optical transitions observed. Also, the maximum energy shift is equivalent to the shift produced by a change of the N content of less than 0.2 %, which is below the accuracy of our determination of the alloy composition. It can therefore be argued that the conclusions of this study are not affected by the omission of the strain effects on the valence band offsets.

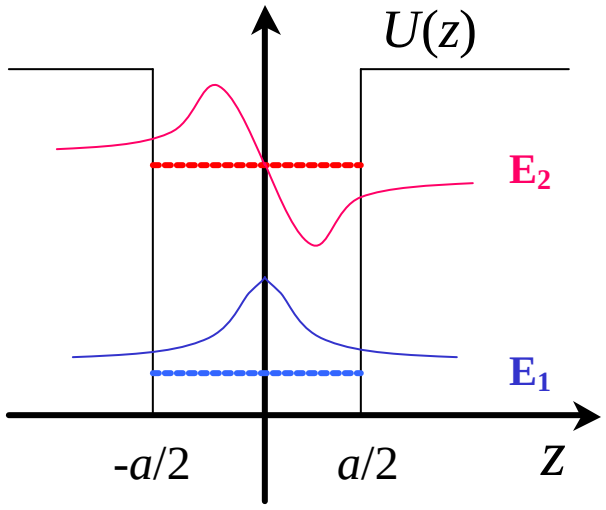


Fig.3.16 A schematic of the ground state and the first excited state wavefunctions in the QW.

The one-dimensional time-independent Schrödinger equation is written as

$$\left\{-\frac{\hbar^2}{2m}\frac{d}{dz^2}+U(z)\right\}y(z)=Ey(z), \qquad (3.31)$$

where $U(z)$ is the square potential shown in Fig.3.16. The boundary conditions are [64]

$$\begin{cases} y(-\infty) = y(+\infty) = 0; \\ y\left(\frac{a}{2}-\right) = y\left(\frac{a}{2}+\right); \\ \frac{1}{m_{in}} \cdot \frac{d}{dz} y(z)\Big|_{\frac{a}{2}-} = \frac{1}{m_{out}} \cdot \frac{d}{dz} y(z)\Big|_{\frac{a}{2}+}. \end{cases} \tag{3.32}$$

The equation and these boundary conditions lead to a number of transcendental equations, from which the bound-state eigen-energies of the system can be determined. For example, the even-parity states (ground state, second excited state, etc.) have the following equation set:

$$\begin{cases} \tan\left(\frac{k_{in}a}{2}\right) = \frac{k_{out}m_{in}}{k_{in}m_{out}}; \\ k_{in} = \sqrt{\frac{2m_{in}E_{even}}{\hbar^2}}; \\ k_{out} = \sqrt{\frac{2m_{out}(U_0 - E_{even})}{\hbar^2}}. \end{cases} \tag{3.33}$$

The numerical solutions for the set have been found and the transition energies have been calculated. The energies of $E_1$ and $E_2$ calculated using the QW effective mass obtained from Eq.(3.30) are shown as solid curves in Fig. 3.13(b). The calculations are in good agreement with the experimental results. The agreement is even more remarkable considering the fact that no adjustable parameters have been used in the calculations. We have used all the parameters (*i.e.*, $E^d$ and $V$) that were previously determined from the studies of composition and pressure dependence of the optical properties of bulk GaAsN alloys [33, 34]. For all the four samples shown in Fig. 3.13, the effective mass calculated from Eq.(3.30) is equal to about $0.11m_0$, which is over 60% larger than the electron

effective mass of GaAs. To demonstrate the effect of the heavier electron mass, we have also calculated the optical transition energies assuming that the electron effective mass of GaAsN alloys is the same as that of GaAs. The results are shown as dashed curves in Fig. 3.13(b). Clearly, much better agreement with the experiment is reached when the N-induced enhancement of the electron effective mass is incorporated in the model. Similar values of the effective mass have also been theoretically predicted [65] and experimentally observed. Jones and co-workers measured via three different techniques an effective mass of ~0.13$m_0$ for $In_{0.07}Ga_{0.93}As_{0.98}N_{0.02}$ [66]. Hetterich *et. al.* observed an effective mass increased by ~0.03$m_0$ in an InGaAsN alloy with 1.5% N [35]. All these independent results agree reasonably well with the values predicted by Eq.(3.30).

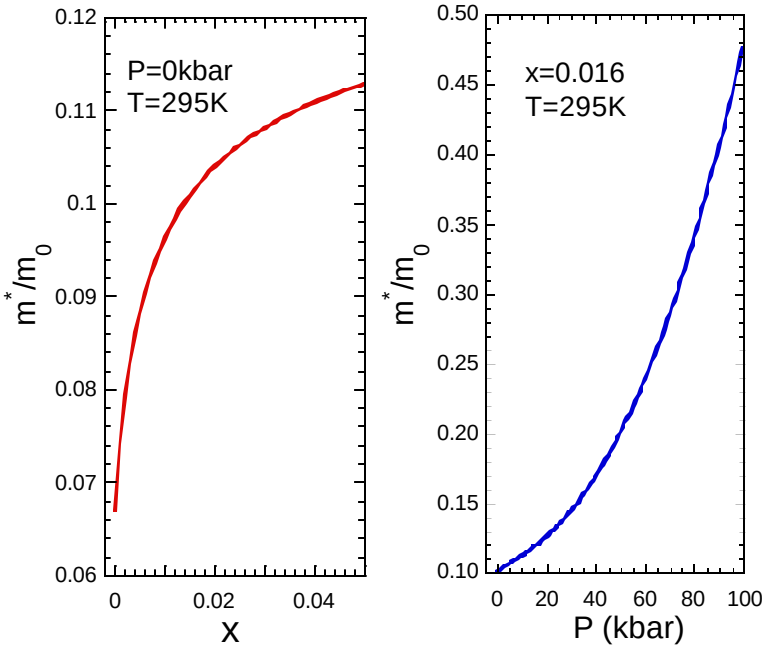


Fig.3.17 The electron effective mass given by Eq.(3.30) as a function of N concentration $x$ and hydrostatic pressure $P$.

Figure 3.18 shows the optical transition energies as a function of the well width for a fixed N concentration, $x$=0.016. The data clearly show increasing quantum confinement with decreasing well width. Again, the theoretical calculations agree well with the measured data if the heavier effective mass given by Eq.(3.30) is used in the calculations as opposed to a fixed value of $0.067m_0$. The effect of the heavier effective mass is especially pronounced for the optical transitions to the first excited state in the well ($E_2$).

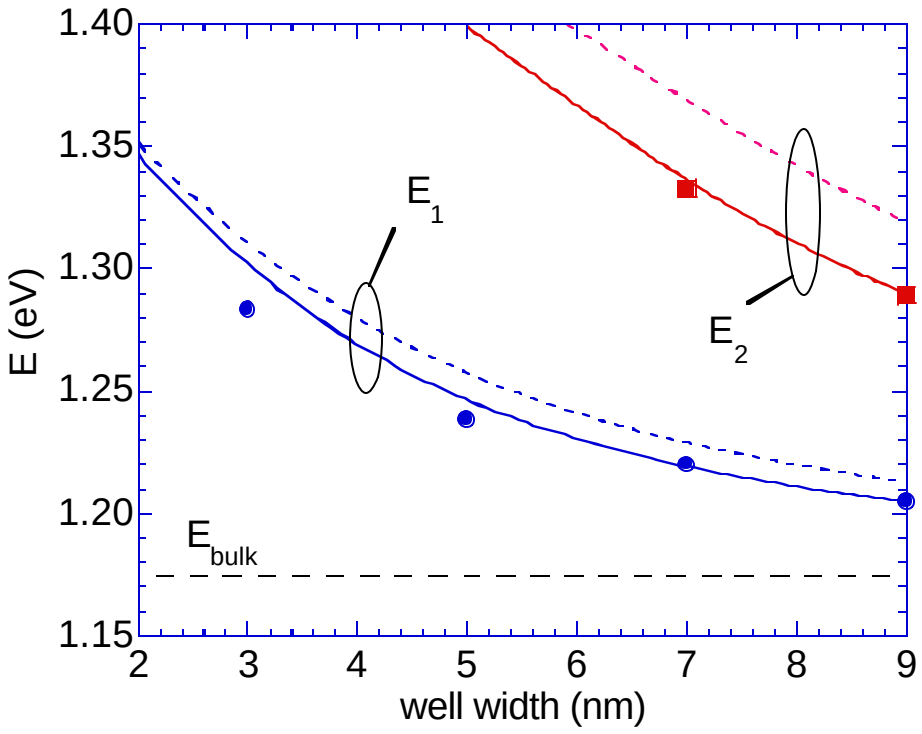


Fig. 3.18 $E_1$ (circles) and $E_2$ (squares) transition energies as a function of well width for $x$=0.016. The meaning of the curves is identical to those in Fig. 3.13(b).

The hydrostatic pressure dependence of the $E_1$ transition is shown in Fig. 3.19, along with the predicted pressure dependence of the bulk GaAsN conduction band edge $E_{\text{bulk}}$. It can be seen that the confinement energy, $E_1$-$E_{bulk}$, decreases with increasing pressure. This effect is a result of the pressure-induced increase of the electron effective mass predicted by the BAC model [33]. Because of the much different pressure coefficients of the extended states and the localized N states [33, 34], the conduction band edge shifts towards $E^d$ under hydrostatic pressures. According to Eqs.(3.26) and (3.30), this shift results in a flattening of the dispersion relation and an increase of the electron effective mass in the lowest conduction band. For the sample in Fig. 3.19, the effective mass increases from $0.11m_0$ at ambient pressure to $0.28m_0$ at 70 kbar, four times larger than the effective mass of the GaAs host. The calculated effective mass as a function of pressure is shown in Fig. 3.17. It is also evident from Fig. 3.19 that, as shown by the dashed curve, the calculations assuming a pressure-independent effective mass deviate from the experimental results at high pressures. The increase of electron effective mass with pressure has also been reported in Ref [66].

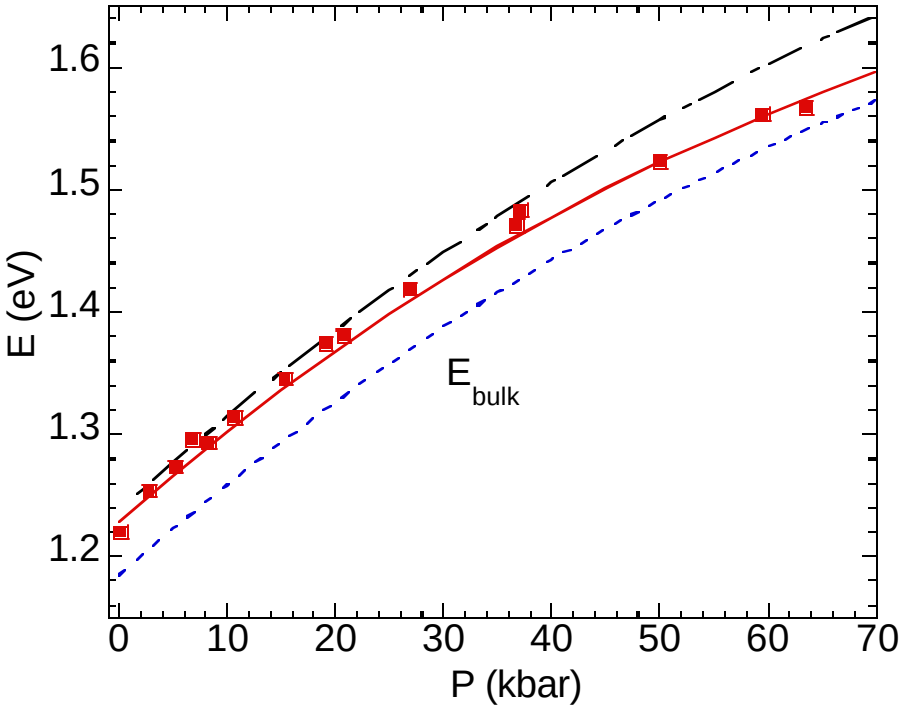


Fig.3.19 The first transition energy $E_1$ as a function of hydrostatic pressure for $x$=0.016 and well width=7nm. Solid curve, calculated values with $GaAs_{1-x}N_x$ electron effective mass given by Eq.(3.30); Long dashed curve, calculated values assuming $GaAs_{1-x}N_x$ electron effective mass equal to $m^*_{GaAs}$. The pressure dependence of the band edge in bulk $GaAs_{1-x}N_x$ expected from the BAC model is shown as a short dashed line.

### 3.4.4 Variational Calculations of the Ground State of Shallow Donors, Neutral Impurities, and Excitons in $GaAs_{1-x}N_x$

In this section, the ground state binding energies of hydrogenic donors, neutral impurities, and excitons in $GaAs_{1-x}N_x$ alloys are calculated based on the new dispersion relation in the context of the BAC model. It will be shown that due to the N-induced nonparabolicity of the dispersion and the downward shift of the conduction band, the Bohr radius and binding energy of shallow donors exhibit strong dependencies on the N concentration.

According to the BAC model, the interaction of the N resonant state with the conduction band of the GaAs matrix gives rise to the formation of two conduction sub-bands, $E_-$ and $E_+$, with non-parabolic dispersion relations given by Eq.(3.26). For lightly doped GaAs, the conduction band of the matrix can be well described by a parabolic dispersion function with a constant effective mass, $m^* = 0.067m_e$.

We consider the hydrogen atom problem for a band with a dispersion relation given by Eq.(3.26). For convenience, we define atomic units in which the unit of length is $\hbar^2 e_r / (m^* e^2)$ (≈10.4 nm for GaAs, the Bohr radius of a hydrogenic donor), the wavevector unit is the reciprocal of the length unit, and the energy unit is $2 \times 13.6 m^* / e_r^2$ (≈ 10.46 meV for GaAs, twice the Rydberg of the hydrogenic donor). In atomic units, the free-carrier-screened Coulomb potential for a hydrogenic donor is written as $V(r) = -e^{-br} / r$, where 1/*b* is the screening length measured in atomic units.

It is well known that the static dielectric constant that affects the binding energy of the hydrogenic impurities depends on the electronic band structure. The dielectric

function consists of the contributions from lattice vibrations and valence band electrons. The total static dielectric constant of GaAs is $e_r(0) = 1 + c_l(0) + c_e(0) \approx 13.2$. The lattice contribution to the static susceptibility, $c_l(0) \approx 2$, is the difference between the high-frequency $e_r$ and the static $e_r(0)$ [9]. $c_l(0)$ is assumed to be less sensitive than $c_e(0)$ to the few percent incorporation of N. To estimate the effect of the modified band structure on the dielectric constant, we adopt an empirical equation proposed by Chadi and Cohen that correlates the static electronic susceptibility to the fundamental band gap, $E_g$, for a wide variety of materials with zincblende structure[67],

$$c_e(0) = \frac{b}{a_0^{3/2} E_g}, \tag{3.34}$$

in which $b$ equal to 159.0 (eV Å$^{3/2}$) is a universal constant, and $a_0$ is the lattice parameter. Since the fundamental band gap is reduced by alloying with GaN according to Eq.(3.26), the total static dielectric constant can be calculated and is shown in Fig. 3.20. In our calculations, we have neglected the variation in $a_0$. It can be seen that Eq.(3.34) predicts that the N-induced modification in the conduction band structure raises the total static dielectric constant. It has been observed experimentally that the refractive index of $In_yGa_{1-y}As_{1-x}N_x$, which is directly related to the dielectric constant, indeed increases upon the incorporation of N [61]. However, no systematic experimental data of $e_r$ are available for a quantitative test of the applicability of Eq.(3.34) in $GaAs_{1-x}N_x$.

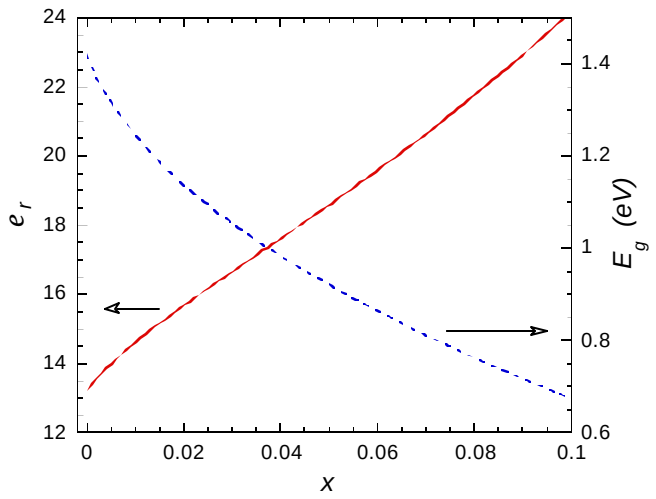


Fig.3.20 Minimum band gap predicted by the BAC model and total static dielectric constant calculated from Eq.(3.34) as functions of $x$.

Considering the complications introduced by the non-parabolic dispersion relation in Eq.(3.26), we seek solutions of the Schrödinger equation in momentum space. With an eigen-energy $W$, one writes the Schrödinger equation as [64]

$$\left(E(k)-W\right)\Phi(\vec{k})=-\int V(\vec{k}-\vec{q})\Phi(\vec{q})d\vec{q}, \tag{3.35}$$

where $E(k)$ is the kinetic energy associated with the dispersion relation. The screened Coulomb potential in momentum space is obtained with a Fourier transform,

$$\begin{aligned} V(\vec{k}) &\equiv \frac{1}{(2p)^3}\int e^{-i\vec{k}\cdot\vec{r}}V(\vec{r})d\vec{r} \\ &= \frac{-1}{(2p)^3}\int e^{-i\vec{k}\cdot\vec{r}}\,\frac{e^{-br}}{r}d\vec{r} \\ &= -\frac{1}{2p^2(b^2+k^2)}. \end{aligned} \tag{3.36}$$

For a central force potential, the Schrödinger equation is separable, and the wavefunction can be factorized as $\Phi_l(\vec{k}) \propto \frac{1}{k} g_l(k) Y_{lm}(q, f)$. For the ground state (1s) of the shallow donor, the radial part of Eq.(3.35) is given by

$$[E(k) - W] \cdot g_0(k) = \frac{1}{p} \int_0^\infty dq\, Q_0(k, q)\, g_0(q), \tag{3.37}$$

where the integral kernel is

$$Q_0(k, q) = \frac{1}{2} \ln \frac{(k+q)^2 + b^2}{(k-q)^2 + b^2}. \tag{3.38}$$

This integral equation can be numerically solved using the variational principle. For a hydrogenic donor in nitrogen-free GaAs, the dispersion is parabolic, $E(k) = E^c(k) = k^2/2$ (in atomic units). Assuming no free-carrier screening, $b$=0, Eq.(3.37) has an analytical solution with an eigen-energy $W = -\frac{1}{2}$ (≈ -5.23meV), and a wavefunction $\frac{g_0(k)}{k} \propto \frac{1}{(1+k^2)^2}$. This is the Fourier transform to momentum space of the ground-state wave function of a normal hydrogenic atom, $e^{-r}$.

For the variational calculation of the non-parabolic conduction band in $GaAs_{1-x}N_x$, we choose

$$g_0(k,t) = 4\sqrt{\frac{2}{p}} t^{5/4} \frac{k}{(t+k^2)^2} \tag{3.39}$$

as a trial function. This function is already normalized, $\int_0^\infty \left| \frac{g_0(k,t)}{k} \right|^2 k^2 dk = 1$. When the parameter $t$=1, $g_0(k,t)$ returns to the original exact solution, $g_0(k)$, for normal hydrogenic

donors with parabolic dispersion relation. The corresponding wave function in real space is the original one, rescaled by a factor $\sqrt{t}$ :

$$\frac{g_0(k,t)}{k} \xleftrightarrow{3D\ Fourier} \frac{c_0(r,t)}{r} \propto \frac{re^{-\sqrt{t}r}}{r}. \tag{3.40}$$

The total energy is the sum of the kinetic energy and potential energy,

$$W(t) = \int_0^\infty E(k)\left|g_0(k,t)\right|^2 dk - \frac{1}{2p}\iint \ln\frac{(k+q)^2+b^2}{(k-q)^2+b^2}\, g_0^{\,*}(k,t)\, g_0(q,t)\, dkdq. \tag{3.41}$$

The minimum point of the $W(t)$ dependence gives the best approximation for the ground state energy for this trial wave function. The integration should be performed within the first Brillouin zone, but due to the strong localization of the wavefunctions in momentum space, one can extend the upper limit of the integration to infinity as a good approximation.

Choosing the dispersion relation $E(k) = E_-(k)$, the lower sub-band of $GaAs_{1-x}N_x$ in Eq.(3.26), we can approximate the ground-state energy numerically. At the minimum point $t=t_m$, the binding energy is given by the difference between the ground-state energy and the bottom of the conduction sub-band, $E = \left|W(t_m) - E_-(0)\right|$. The extent of the wavefunction in real space (Bohr radius) is given by $a_B = 1/\sqrt{t_m}$ in atomic units.

As an example, Fig.3.21 shows the curve of $W(t)$ for the unscreened Coulomb potential. The minimum point of the curve gives the values of $t_m$ and $W(t_m)$. From these values the Bohr radius and the binding energy of the system can be calculated. It can be seen that as $x$ increase from 0 to 0.02, the minimum point of the curve shifts downward and rightward, corresponding to a lower eigen-energy and a smaller Bohr radius, respectively.

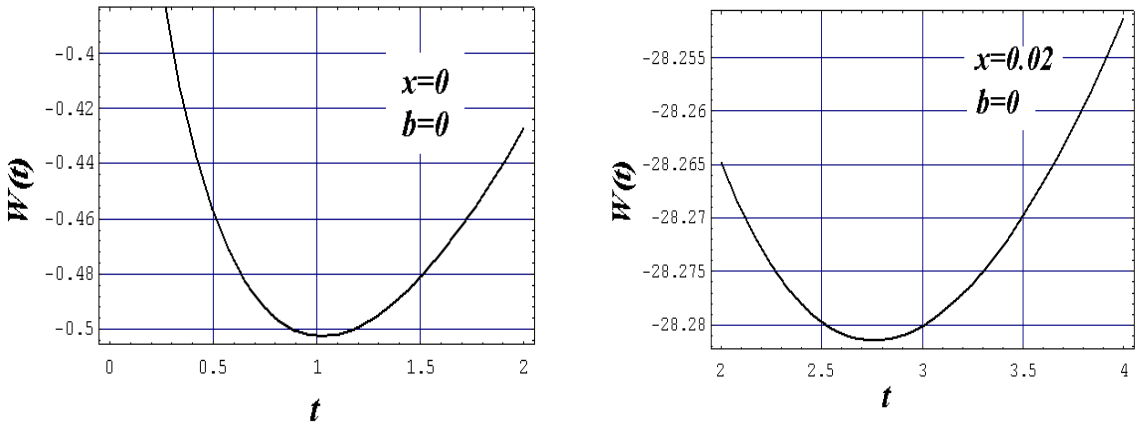


Fig.3.21 The total energy as a function of the variational parameter $t$ for unscreened Coulomb potential ($b$=0) for $x$=0 and 0.02. The change in $e_r$ shown in Fig.3.20 is not included in the calculation. The energy is always measured in atomic units from the bottom of the GaAs conduction band.

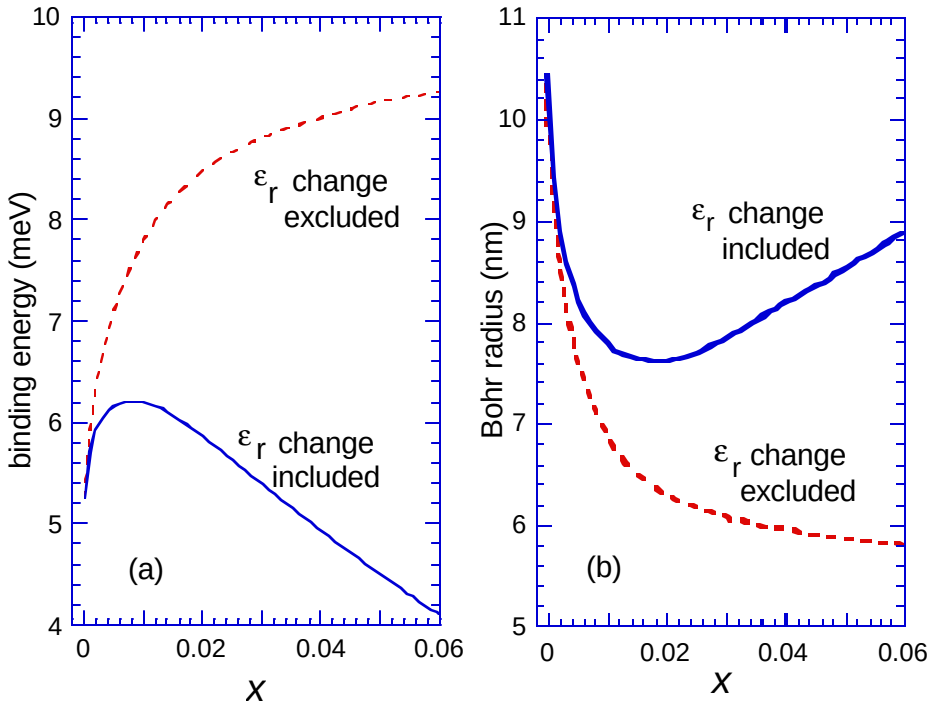


Fig.3.22 Calculated shallow donor binding energy (a), and Bohr radius (b), as functions of $x$ for a Coulomb potential without free-carrier screening. Two cases are shown: the effect of an increasing dielectric constant in Fig.3.20 is excluded or included.

The binding energy and the Bohr radius of the ground state of a hydrogenic donor as functions of $x$ calculated for the case of negligible free-carrier screening of Coulomb potential ($b$=0) are shown in Fig.3.22(a). The initial rapid increase of the binding energy shown in Fig. 3.22(a) is attributed to the N-induced increase of the effective mass. The gradual decrease of the binding energy for $x$ > 1% is associated with the increase of the dielectric constant. If the change of the dielectric constant predicted by Eq.(3.34) is neglected and a composition-independent $e_r$=13.2 is adopted, the binding energy increases monotonically, reflecting the increase of the electron effective mass with increasing N composition. These two situations should correspond to the upper and lower limits for the composition dependence of the binding energy. The effects of the composition dependencies of the effective mass and the dielectric constant are also clearly visible in the dependence of the Bohr radius on the N content shown in Fig. 3.22(b).

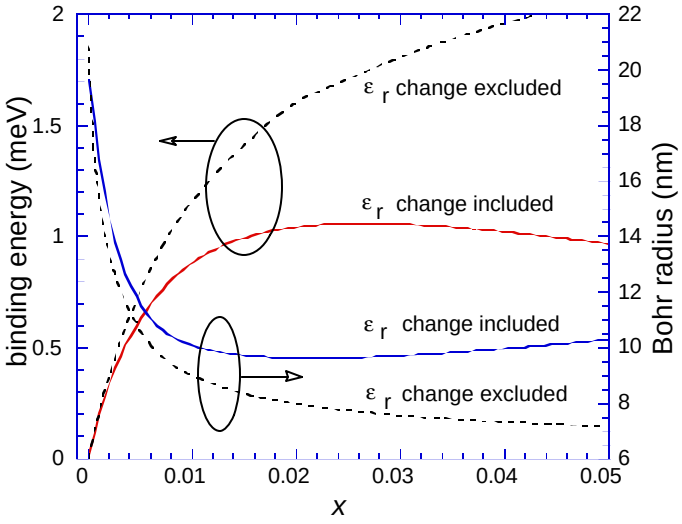


Fig.3.23 Calculated donor binding energy and Bohr radius as functions of N concentration for a free-carrier screened Coulomb potential with screening factor $b$=1.

Figure 3.23 shows the binding energy and the Bohr radius as a function of the N concentration for a Coulomb potential screened by free carriers with screening factor $b$=1, *i.e.*, a screening length $=\hbar^2 e_r/\left(m^* e^2\right)=\frac{e_r}{13.2}\times 10.4\,(\text{nm})$. The binding energy increases dramatically as $x$ increases from 0 to 0.02. The Bohr radius decreases rapidly for $x$ increasing from 0 to 0.01. At $x$=0.01, the predicted two-fold reduction of the effective Bohr radius should cause a large, eight-fold increase of the critical concentration for a metal-insulator transition for shallow donors in $GaAs_{0.99}N_{0.01}$.

Due to the lack of Coulomb attraction, the potential of a neutral impurity is usually much weaker and shorter-ranged than that of the hydrogenic defect. Several functional forms have been proposed to model the potential of neutral impurities [69]. Among them, the simplest ones are probably the "square" potential and the exponential potential, $-b_1 e^{-b_2 r}$. These potentials are shown in Fig. 3.24 for comparison.

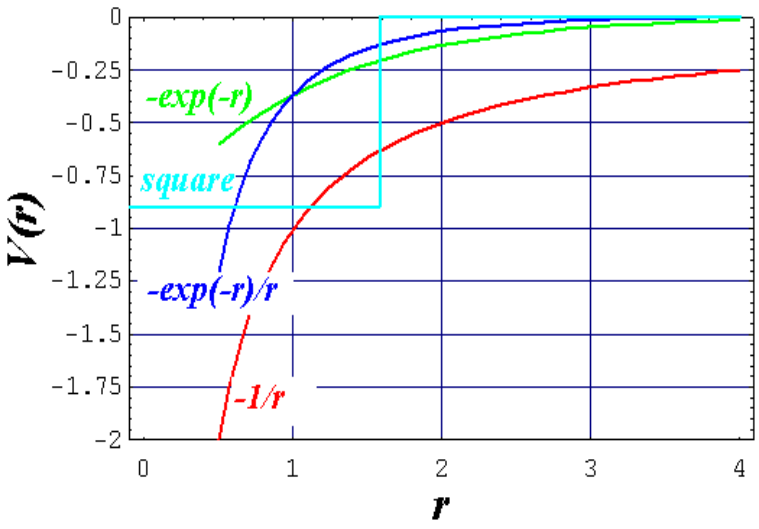


Fig.3.24 Comparison between different functional forms of potentials.

Similar variational calculations can be performed for these neutral impurity potentials. For example, for the exponential functional form, the integral kernel in Eq.(3.37) should be replaced by

$$V(r) = -b_1 e^{-b_2 r} \xrightarrow{3D\ Fourier} Q_0(k,q) = \frac{b_1 b_2}{p}\left[\frac{1}{b_2^2 + (k-q)^2} - \frac{1}{b_2^2 + (k+q)^2}\right]. \quad (3.42)$$

The calculated binding energy and Bohr radius for exponential potential with $b_1$=$b_2$=1 are shown in Fig. 3.25 in comparison with the previously-shown results of the Coulomb potential. It can be seen from Fig. 3.25 that, due to the much weaker attraction of the neutral impurity potential, the binding of electrons is much weaker. Nevertheless, its dependence on the N composition is similar to that of the hydrogenic donor.

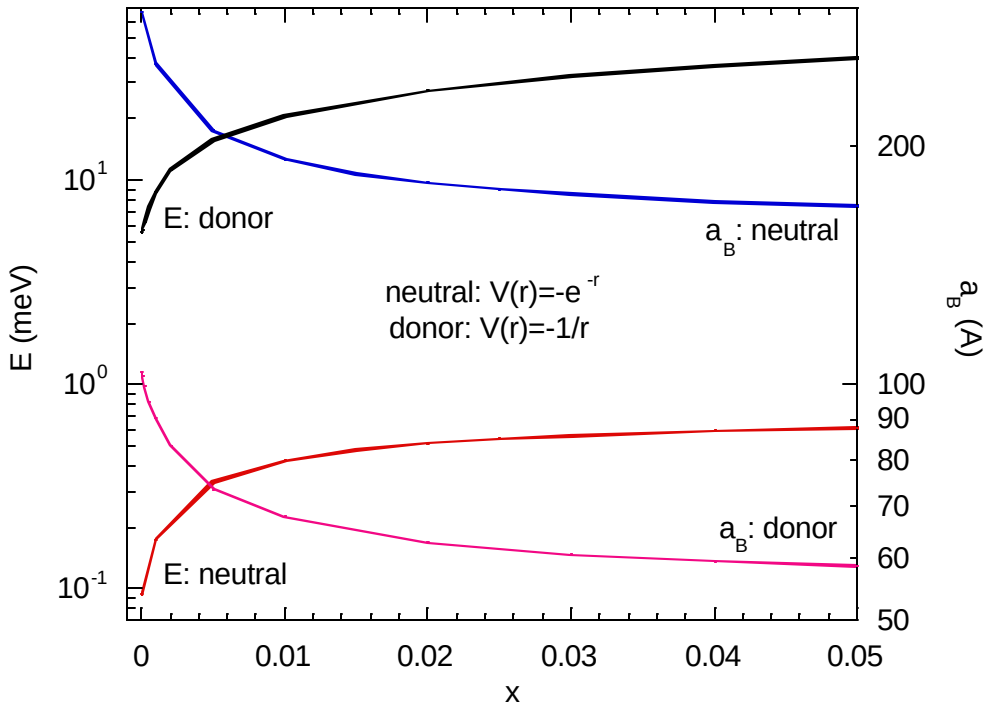


Fig.3.25 The binding energy and Bohr radius of a shallow donor (-1/$r$) and a neutral impurity potential (-$e^{-r}$). The change in $e_r$ shown in Fig. 3.20 is not considered in the calculation.

The ground-state energy of excitons can be calculated in a similar way. Assuming a single parabolic dispersion for the hole with effective mass $m_h^*$ (approximately $0.45m_0$ for heavy holes in GaAs), the total kinetic energy of the system can be written as

$$E(k) = E\_(k) + E_h(k) = E\_(k) + \frac{m^*}{m_h^*}\frac{k^2}{2}. \tag{3.43}$$

This energy is also sensitive to external pressure $P$, linked by the pressure dependencies of $E^d$ and $E^c(k)$ through $E\_(k)$. Shown in Fig.3.26 is $E(k)$ calculated at ambient pressure and for $P$=100kbar.

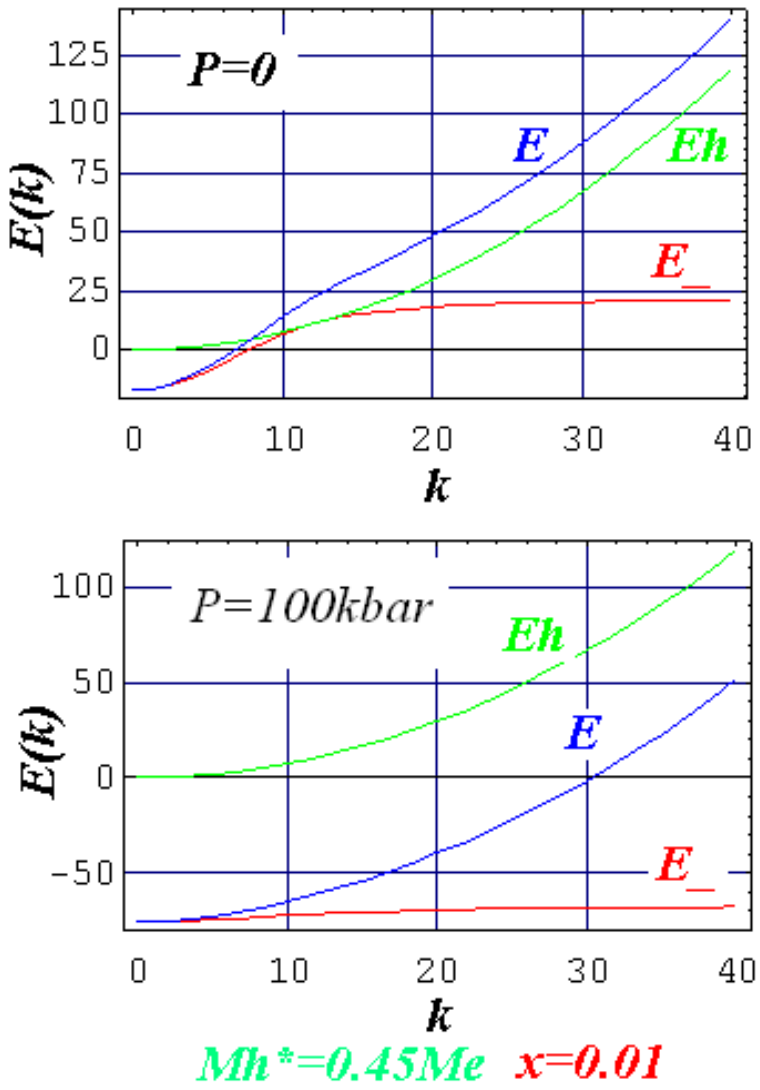


Fig.3.26 The kinetic energy of the direct exciton system for $x$=0.01 at ambient pressure and $P$=100kbar. The energy is measured in atomic units referenced to the bottom of the conduction band of GaAs, $E^{c}(0)$.

Assuming an unscreened Coulomb interaction between the electron and the hole, substitution of Eq.(3.42) into Eq.(3.41) for the variational calculation gives the Bohr radius and binding energy as a function of pressure and N concentration. The results for $x$=0.01 are shown in Fig. 3.27. The Bohr radius is reduced to ~1/4 of the ambient-

pressure value at 120 kbar. This is due to the effect that the pressure-induced flattening of the dispersion encourages the wavefunction to expand in ***k*** space, corresponding to a shrinkage of the wavefunction in real space. The increase in the binding energy is also considerable. At ambient pressure, the hole mass is much larger than the electron "mass", therefore the exciton is "hole-centered", and the binding energy is close to the binding energy of a hydrogenic donor (~5meV). At high pressures, the conduction dispersion is flattened; hence the electron effective "mass" is greatly enhanced (see Fig. 3.17). Therefore, the exciton becomes "electron-centered". As a result, the binding energy of the exciton approaches the binding energy of hydrogenic acceptors in GaAs (~35meV).

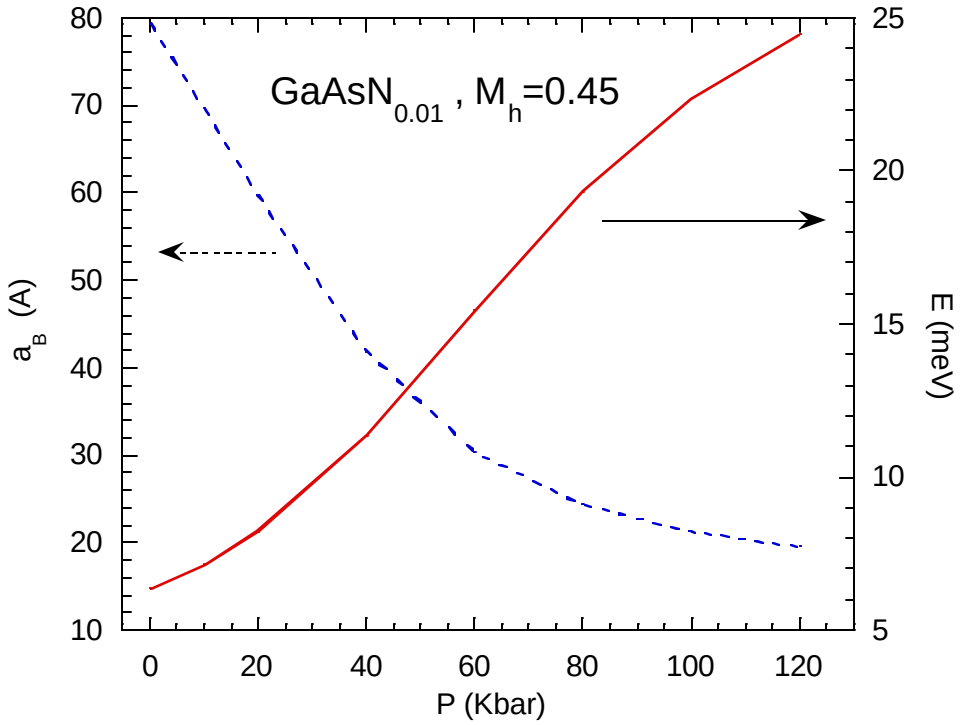


Fig.3.27 The calculated Bohr radius and binding energy for $x$=0.01 as a function of pressure. The change in $e_r$ shown in Fig.3.20 is not included in the calculation.

The variational calculations found the approximate binding energy and Bohr radius of various binding systems in $GaAs_{1-x}N_x$ with this special non-parabolic conduction dispersion. The results not only provide a possible way to understand some interesting observations made with this alloy, such as the behavior of the linewidth of exciton-related optical transitions [70], but it can be also used to analyze and predict new properties of this alloy, such as the threshold of a Mott transition and transport properties under pressure.

### 3.4.5. State Broadening and Related Effects

In preceding sections, the N-induced modification of the conduction band dispersion and some related effects are discussed in detail. In addition to the changes in the dispersion relation, the band restructuring caused by the BAC effect also includes a significant broadening of the conduction band as illustrated in Fig. 3.5(a). In this section the band broadening effect will be discussed.

As the expression of the Green's function is obtained, the density of states of free electrons can be calculated from the imaginary part of the Green's function [71],

$$r(E) = \frac{1}{p}\,\mathrm{Im}\sum_{\boldsymbol{k}} G_{\boldsymbol{kk}}(E) = \frac{1}{p}\int r_0\left(E_{\boldsymbol{k}}^{c}\right)\mathrm{Im}\left[G_{\boldsymbol{kk}}(E)\right]dE_{\boldsymbol{k}}^{c}. \tag{3.44}$$

The integration converges rapidly with $E_{\boldsymbol{k}}^{c}$ in a small range that is in proportion to $x$. The calculated perturbed DOS for $GaAs_{1-x}N_x$ with several small values of $x$ is shown in Fig. 3.28. Note that the anticrossing interaction leads to a dramatic redistribution of the electronic states in the conduction band. The most striking feature of the DOS curves is the clearly seen gap between $E_+$ and $E_-$ that evolves with increasing N content.

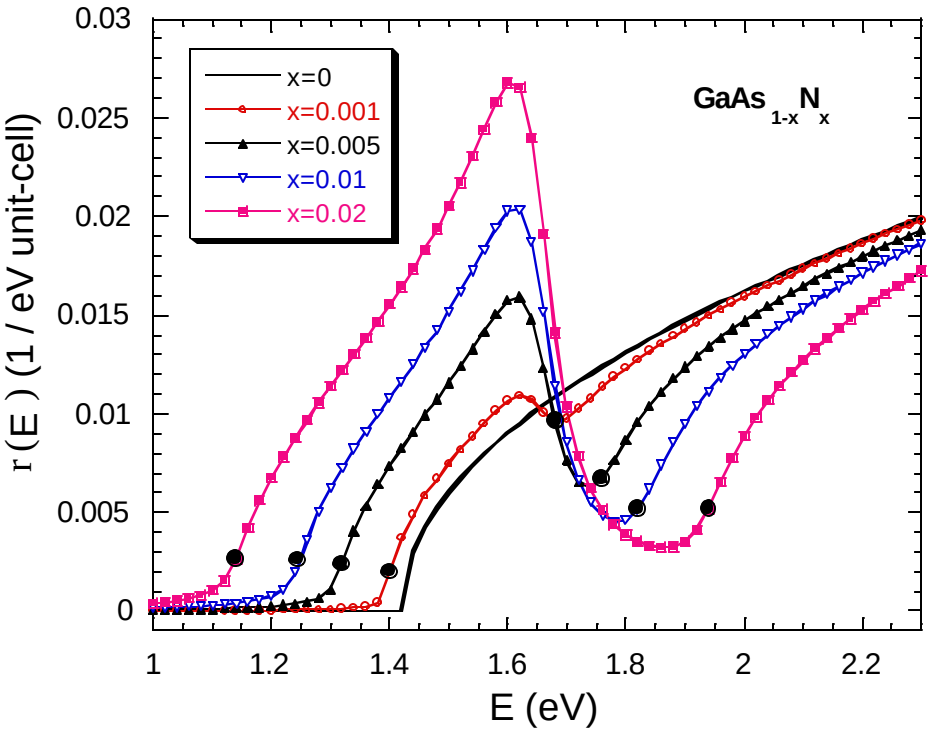


Fig.3.28 Density of states of $GaAs_{1-x}N_x$ alloys for a range of values of $x$ as compared with the unperturbed DOS. The two black dots in each curve indicate the energy positions of the $E_-$ and $E_+$ subband edges.

In order to illustrate the effect of the state broadening on the optical properties, we consider the spectral dependence of the interband absorption in $In_yGa_{1-y}As_{1-x}N_x$ alloys. The optical absorption coefficient due to the transitions from the valence bands to the restructured conduction bands can be written in the form of the joint density of states as

$$a(E) \propto \frac{1}{E}\sum_{v}\int r_0\left(E_{\mathbf{k}}^{c}\right)\mathrm{Im}\left[G_{\mathbf{kk}}\left(E+E_{\mathbf{k}}^{v}\right)\right]dE_{\mathbf{k}}^{c}. \qquad (3.45)$$

In this expression, the sum over $v$ represents the sum of the contributions from the heavy-hole, the light-hole, and the spin-orbit split-off valence bands. Assuming parabolic forms

for the dispersion of the valence bands $E_k^v$ near the Brillouin zone center, the optical absorption is calculated for $In_{0.04}Ga_{0.96}As_{0.99}N_{0.01}$ for which experimental results are available [72]. The comparison between the calculation and the experimental data is shown in Fig.3.29. In the calculation, the only parameter that has been adjusted is the prefactor $b$ used to scale the energy broadening. The best fit with the experimental data is obtained with $b$=0.22. The calculation clearly reproduces the two edges in the absorption, one starting at ~1.8 eV due to the onset of the transitions from the heavy-hole and light-hole valence bands to $E_+$, and one starting at ~1.5 eV attributed to the transition from the split-off valence band to $E_-$. The more rapid rise of the experimental data at the fundamental absorption edge near 1.2 eV is most likely due to the continuum exciton absorption effect, which has not been included in the calculation [9].

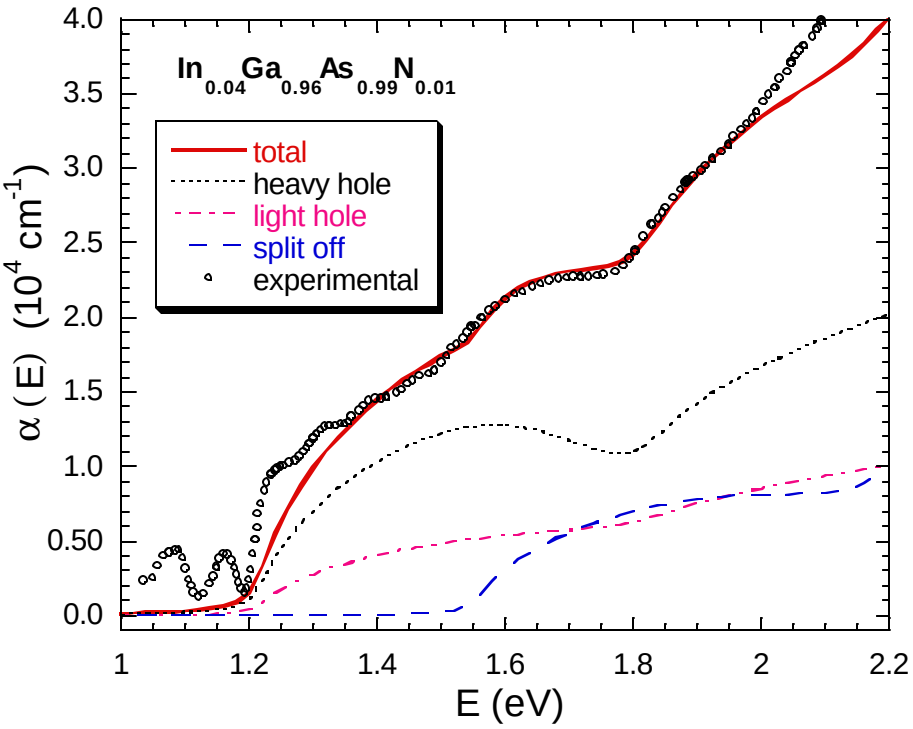


Fig.3.29 Calculated optical absorption coefficient in comparison with room-temperature experimental data for free-standing $In_{0.04}Ga_{0.96}As_{0.99}N_{0.01}$. The oscillations below the absorption edge are due to Fabry-Perot interference.

According to the band anticrossing Eq.(3.26), the hybridization results in an energy gap near $E^d$ with a magnitude depending on $x$,

$$\Delta = E_+(0) - E^d = \frac{1}{2}\left(\sqrt{\left(E^d - E_0^c\right)^2 + 4V^2 x} - \left(E^d - E_0^c\right)\right) \approx \frac{V^2 x}{\left|E^d - E_0^c\right|}. \qquad (3.46)$$

The broadening of $\tilde{E}_\pm(k)$ near the edge of the small gap is approximately $\Gamma_d = pbV^2 r_0\left(E^d\right)$. To have a well-defined band restructuring, the gap between the two

subbands should be larger than the energy uncertainty, *i.e.*, $\Delta > \Gamma_d$. This condition defines a lower limit of $x$ for the band restructuring,

$$x > x_c \equiv 4p^2 b \cdot \left( \left| E^d - E_0^c \right| / e_B \right)^{3/2}. \tag{3.47}$$

For N in GaAs, this concentration limit is $x_c \sim 0.0016$.

The band broadening function in Eq.(3.27) defines the lifetime of the free electrons through the uncertainty principle. The mean free path of the electrons is the distance that a free electron on the Fermi surface travels within its lifetime. The upper limit of $x$ for the applicability of CPA treatment can be set as the concentration for which the average distance between impurity atoms is equal to this mean free path. The upper limit of $x$ is thus inversely proportional to the free electron concentration, linked by the Fermi velocity.

For n-type $GaAs_{1-x}N_x$, the electronic transport properties are also strongly affected by the BAC effect. The conductivity of the system is closely related to the imaginary part of the Green's function [49, 71],

$$s(x) = \frac{2e^2\hbar}{pV} \int_{-\infty}^{\infty} dE \left( -\frac{\partial f(E, E_F)}{\partial E} \right) \sum_k \{ v(k) \mathrm{Im}[G_{kk}(E)] \}^2, \tag{3.48}$$

where $f(E, E_F) = 1/\{1 + \exp[(E - E_F)/(k_B T)]\}$ is the Fermi distribution, and

$$v(k) = \frac{1}{\hbar} \frac{\partial E_-(k)}{\partial k} \tag{3.49}$$

is the group velocity of the free electrons. The Fermi energy is determined by the free carrier concentration with the following equation,

$$n = \int_0^{\infty} r(E) f(E, E_F) dE \,. \tag{3.50}$$

The mobility of the system is given by

$$m(x,n)=\frac{s(x,n)}{e\cdot n}. \tag{3.51}$$

From these equations it can be seen that the transport properties are more sensitive to the level broadening than the optical properties are. Indeed, the limit on the mobility imposed by the N-state scattering is completely dictated by the broadening function. Experimentally it has been observed that the incorporation of N into GaAs reduces drastically the mobility of the material. For n-type GaAs, the room-temperature Hall mobility can easily exceed 1000 $cm^2/Vs$ [73]. Hall mobilities of 190 $cm^2/Vs$ for as-grown $In_{0.05}Ga_{0.95}As_{0.99}N_{0.01}$ and 70 $cm^2/Vs$ and 140 $cm^2/Vs$ for as-grown and 650 $^oC$ post-growth-annealed $In_{0.08}Ga_{0.92}As_{0.97}N_{0.03}$ have been reported [74]. This effect can be at least qualitatively understood from the band state broadening mechanism. The emergence of the imaginary part in $\tilde{E}_{\pm}(k)$ defines a broadening in the energy levels, along with a finite lifetime $t\sim\hbar/\Gamma_{\pm}$. The mobility of the system, neglecting phonon scattering, is given by $m\approx<t/m^*>=<\hbar/(m^*_{\pm}\cdot\Gamma_{\pm})>$. Therefore, the mobility of the system is reduced because of two effects caused by the impurity scattering: the increase in the effective mass and more strongly, the finite energy broadening. Figure 3.30 shows typical transport properties of an InGaAsN sample.

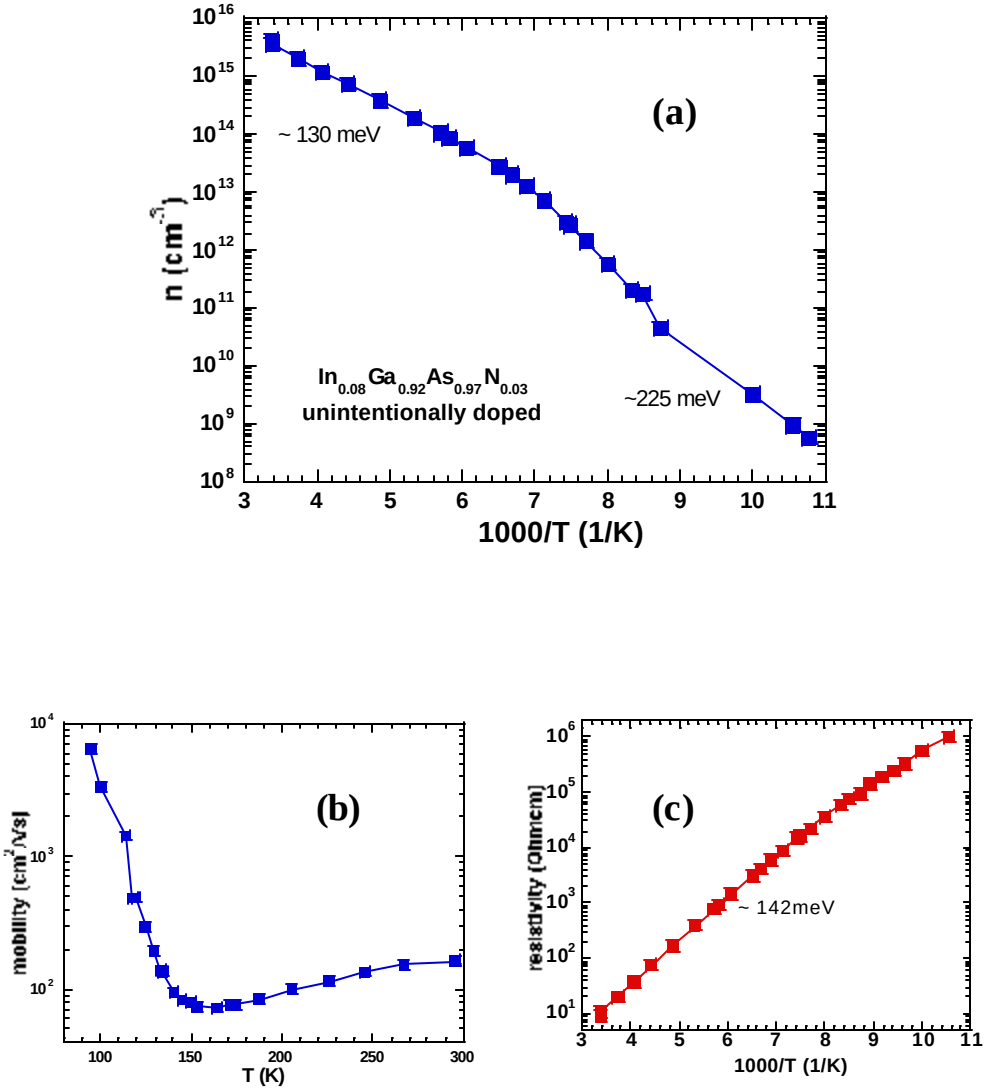


Fig.3.30 Transport properties of an unintentionally doped sample measured by Hall effect. (a) electron concentration, (b) mobility and (c) resistivity as a function of temperature. The numbers in meV represent the activation energy calculated from the slope on the Arrhenius plot.

### 3.4.6 Band Anticrossing in the Entire Brillouin Zone: $GaP_{1-x}N_x$

GaP is an indirect-gap semiconductor. It has been demonstrated that the incorporation of N into GaP changes the nature of the fundamental bandgap from indirect to direct [6]. Very recently, the transition of the lowest bandgap from indirect to direct has been shown to occur around at most $x$~0.5% by using time-resolved photoluminescence spectroscopy [75]. A new conduction band minimum is formed at the ? point as a result of the anticrossing between the ? edge of the conduction band and the N level, which is located at 2.15eV above the top of the valence band (slightly below the X band edge). The interaction strength has been determined to be $V$=3.05 eV. Figure 3.31 shows the energies of $E_-$ and $E_+$ as a function of N concentration observed using PR spectroscopy, in comparison with the BAC calculations [6]. Since the modulated PR technique responds to direct transitions only, these observations confirm the direct nature of the fundamental bandgap of the $GaP_{1-x}N_x$ alloy. The energy level of the localized N states in GaP has previously been directly observed by photoluminescence spectroscopy [11].

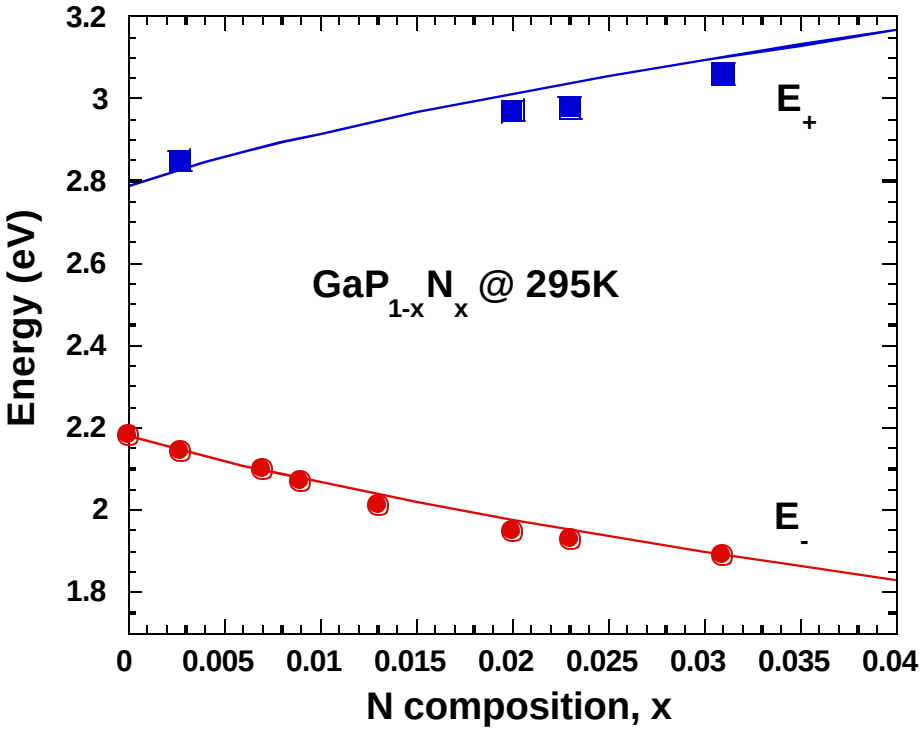


Fig.3.31 $E_+$ and $E_-$ measured by PR as a function of $x$ for $GaP_{1-x}N_x$. The point at $x = 0$ and $E_- = 2.18$ eV is not measured but the predicted nitrogen level in dilute limit. The curves are the BAC calculations.

On the other hand, since the wavefunction of the nitrogen state is highly localized in real space, its Fourier transform has significant contributions by off-zone-center components in the Brillouin zone. It is, therefore, expected to couple not only to the Γ conduction state, but also to other conduction states such as the L and X band minima. This section summarizes our low temperature investigations of the hydrostatic pressure dependence of the fundamental band gap of $GaP_{1-x}N_x$ alloys with $x$ varying from 0.7% to 2.3%. It will be shown that at high pressures the fundamental band gap shifts to lower energy as a function of pressure, approaching the negative pressure dependence of the X

band minimum of GaP. This pressure dependence is explained by the interactions of the N localized state with the lowest conduction band of the host GaP.

The $GaP_{1-x}N_x$ samples are epitaxial layers grown on GaP substrates by gas-source molecular-beam epitaxy using an rf plasma nitrogen radical beam source. The layer thickness varies from 0.75 to 0.9 μm. Prior to the growth of the $GaP_{1-x}N_x$ layer, a 0.2μm GaP buffer layer was deposited on the substrate. The nitrogen concentration of the samples was determined from high-resolution x-ray rocking-curve measurements and theoretical dynamical simulations. A detailed discussion of the sample preparation and x-ray measurements has been published [76].

Shown in Fig. 3.32 is the absorption curve of a GaPN film grown on a GaP substrate. The substrate has been thinned down to ~15 μm. As a comparison, the absorbance of a N-free GaP sample thinned to about the same thickness is also shown. The onset of the GaP X-band absorption is seen at ~ 2.3 eV. Compared with the GaP absorption curve, the GaPN film exhibits a strong absorption band below the GaP X-band edge. The bottom curve shows the difference between these two curves, corresponding to the absorption solely due to the GaPN film.

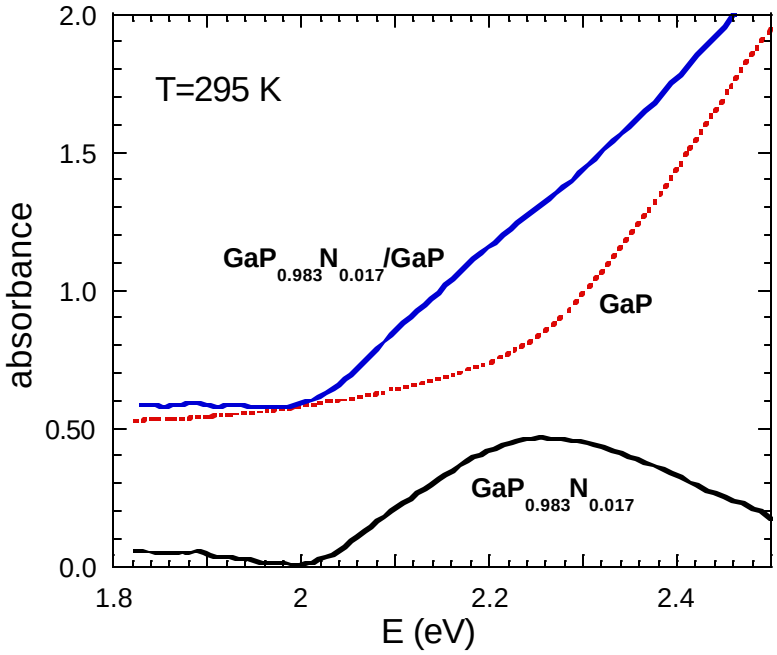


Fig.3.32 The absorbance (absorption coefficient multiplied by thickness) of two samples: $GaP_{0.983}N_{0.017}$(0.9μm)/GaP(15μm) and GaP(15μm). The bottom curve shows the difference between the absorbance of these two samples.

The $GaP_{1-x}N_x$ samples exhibit intense PL visible to the naked eye even at room temperature. Figure 3.33 Shows the PL signal obtained from a GaPN sample with a range of temperature. As the temperature increases, the PL intensity drops significantly.

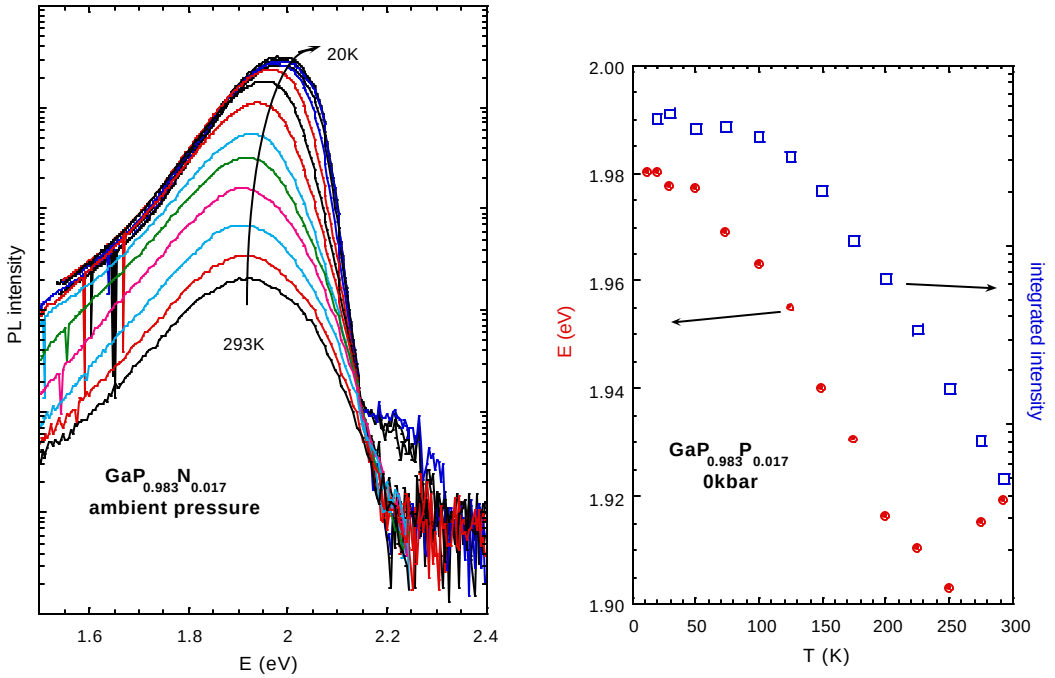


Fig.3.33 PL signal (log scale) for $x$=0.017 at ambient pressure (~0kbar) for a wide range of temperature. The right panel shows the peak energy and the integrated intensity (log scale) of the PL signal as a function of temperature.

As demonstrated earlier [6], the PL also decreases in intensity as the pressure is increased. The room-temperature PL becomes undetectable at high pressures (*e.g.*, above ~ 35 kbar for $x$ = 1.3%). Shown in Fig. 3.34 is the PL of the same sample obtained at 69.4 kbar and different temperatures. The PL intensity depends on temperature in a very similar way as at ambient pressure. However, at ambient pressure, the PL persists as temperature increases and is still strong enough to be detected at room temperature. Figure 3.34 shows that at 69.4 kbar, the PL intensity drops below the noise level (or buried by the diamond PL from the diamond anvil cell used for the application of the hydrostatic pressure) beyond ~ 150 K. Figure 3.35 shows the Arrhenius plot of the

integrated intensity as a function of inverse temperature. The numbers on the plots indicate the slope of the dependence measured in terms of the activation energy. These activation energies provide useful information for identifying the nature of the luminescence. It can be concluded that cooling down the sample greatly improves the luminescence efficiency. If the luminescence properties are to be studied at high pressure, the experiment has to be carried out at low temperature.

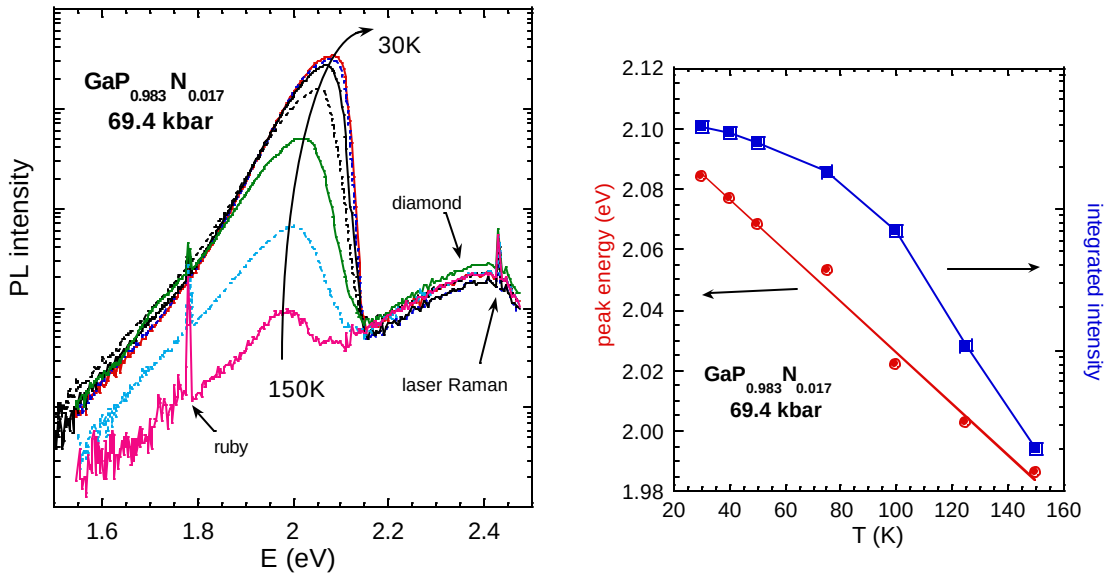


Fig.3.34 PL signal (log scale) for $x$=0.017 at 69.4K and different temperatures. The right panel shows the peak energy and the integrated intensity (log scale) of the PL signal as a function of temperature.

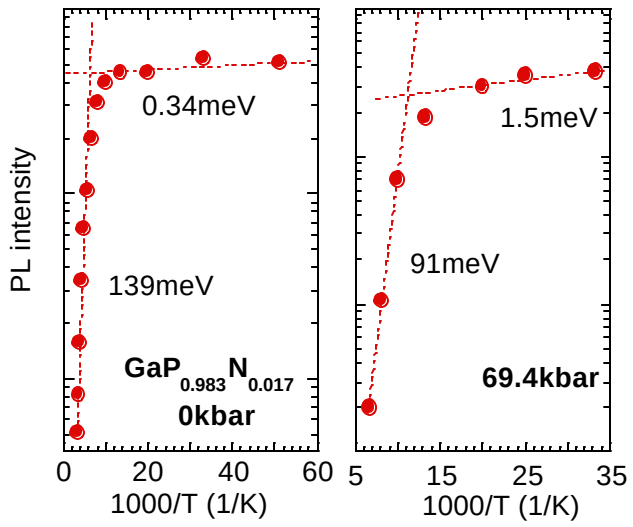


Fig.3.35 Arrhenius plot of the integrated intensity of the PL signal as a function of temperature at ambient pressure and 69.4kbar, respectively.

Shown in Fig. 3.36(a) is the 30K PL spectrum of a $GaP_{0.977}N_{0.023}$ sample at different hydrostatic pressures. The PL signal decreases in intensity with increasing pressures, but remains detectable to pressures above 100 kbar. Figure 3.36(b) shows the peak energy and the integrated area of the PL as a function of pressure. The PL intensity starts to decrease abruptly at ~ 80±10 kbar, the pressure at which the peak energy reaches its maximum. This phenomenon implies a fundamental change in the nature of the lowest conduction band edge at this pressure.

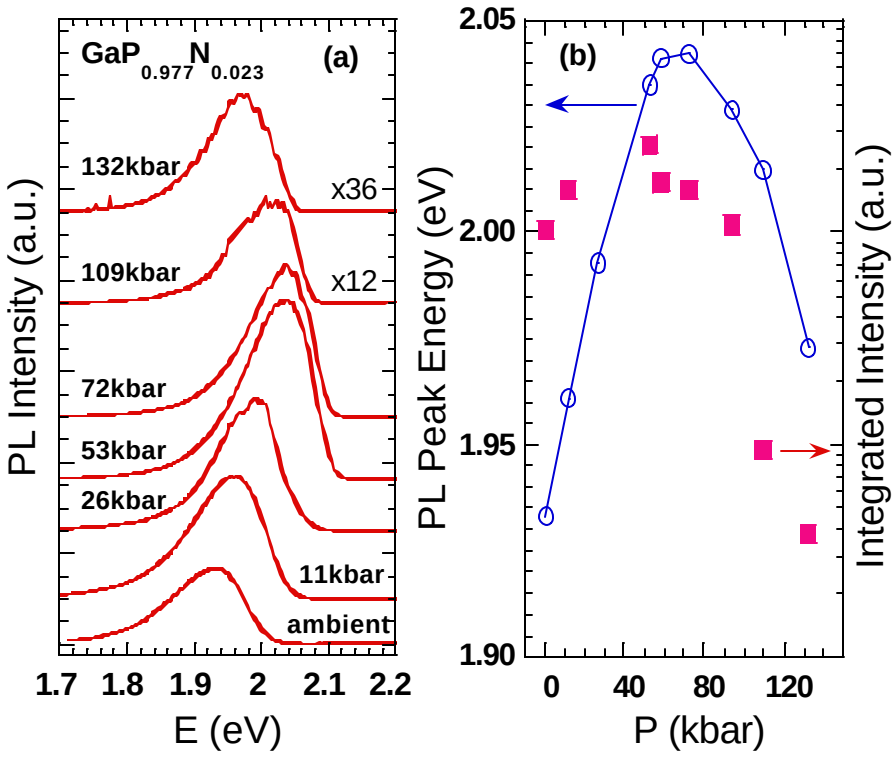


Fig.3.36(a) Photoluminescence spectra of a $GaP_{0.977}N_{0.023}$ sample at a range of pressures. All the PL spectra were taken at T=30K. (b) Pressure dependencies of the peak energy and the integrated PL intensity of $GaP_{0.977}N_{0.023}$ at 30 K. Note the logarithmic scale of the integrated intensity.

At low pressures, the PL signal from $GaP_{1-x}N_x$ corresponds to the direct transition from the lowest conduction band to the top of the valence band. As a result of the anticrossing between the Γ conduction band minimum of GaP and the N localized level, the peak energy of the PL signal blueshifts at a small rate with increasing pressure [6]. The PL peak energy for $GaP_{0.977}N_{0.023}$ as a function of pressure is shown in Fig. 3.37, together with the results from two other samples with $x$=0.007 and 0.017. The full width at half maximum (FWHM) of the PL peak is about 0.12eV. It should be noted that N-free

GaP did not show a detectable PL signal under the same experimental conditions. A similar non-monotonic pressure behavior is observed for all three N-containing samples. Interestingly, the PL peak energies of all the three samples tend to approach the same asymptotic pressure dependence at high pressures. The difference between the peak energies for $x$=0.007 and 0.023 is reduced from 160meV at ambient pressure to 50meV at ~110kbar. As is well known, in GaP the X band minimum ($E_X$) is located at ~ 2.35eV above the valence band edge at ambient pressure at 30K [77], and has a negative pressure coefficient of about -0.0024eV/kbar [78]. The energy of this band minimum is also plotted in Fig. 3.37. It is evident that at high pressures the PL peak energies of all three alloys approach the indirect band gap ($X_c$-$\Gamma_v$) of the host GaP.

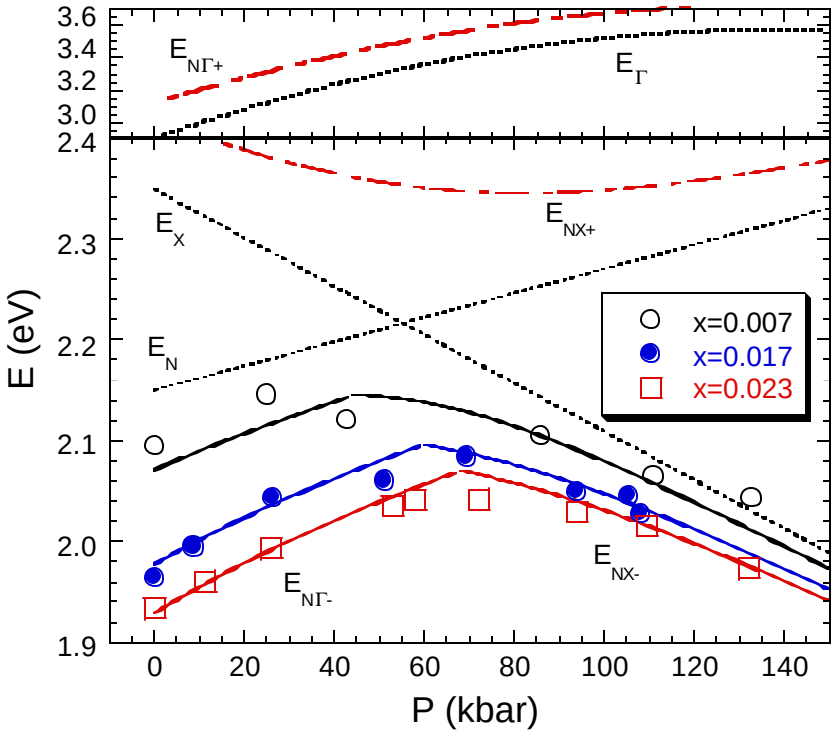


Fig.3.37 PL peak energy at 30K as a function of pressure for three samples with different N concentrations. The short-dashed lines indicate the pressure dependencies of the N localized state, the Γ band and the X band minima of GaP. The solid curves are the calculated lowest conduction band energies for the three N concentrations based on the band anticrossing model. The kinks in the calculated curves indicate the crossover of the nature of the lowest conduction band from N-G mixing to N-X mixing. The other subband edges at higher energy are also shown in dot-dashed lines.

To explain the pressure behavior of these PL spectra, we describe the conduction band states by the BAC model represented by Eq.(3.26). The coupling between the N states and the band states of GaP is described by the adjustable parameter $V$ and is assumed to be wavevector-dependent.

The location of the Γ conduction band edge $E_\Gamma$ in GaP as function of the hydrostatic pressure is well known and has been shown to be described by $E_\Gamma(P) = 2.9 + 0.0097P - 3.5\times10^{-5}P^2$ [78, 79], where $E_\Gamma(P)$ is measured in eV and $P$ is the hydrostatic pressure in kbar. With the known pressure dependencies of $E_X(P)$ and $E_\Gamma(P)$, we fit the lowest edge of the $E_-(k)$ subband calculated from Eq.(3.26) to the experimental points in Fig. 3.37. As is seen in Fig. 3.37, the pressure dependence of the PL peak energy can be divided into two regimes. At low pressures, the PL is attributed to the direct transitions from the lowest conduction band edge $E_{N\Gamma-}$, which evolves from the $E_N$ level through a band anticrossing interaction with $E_\Gamma$, to the top of the valence band. The pressure coefficient for this transition is small and positive, similar to that of the $E_N$ level. At higher pressures the $E_X$ edge shifts downwards, consequently the $E_{NX-}$ edge resulting from the anticrossing interaction between $E_X$ and $E_N$ becomes the lowest conduction band edge. The indirect transitions from $E_{NX-}$ to the top of the valence band are responsible for the PL signal in this pressure regime. The abrupt decrease of the PL intensity shown in Fig. 3.37(b) is consistent with this predicted change in the character of the fundamental band gap.

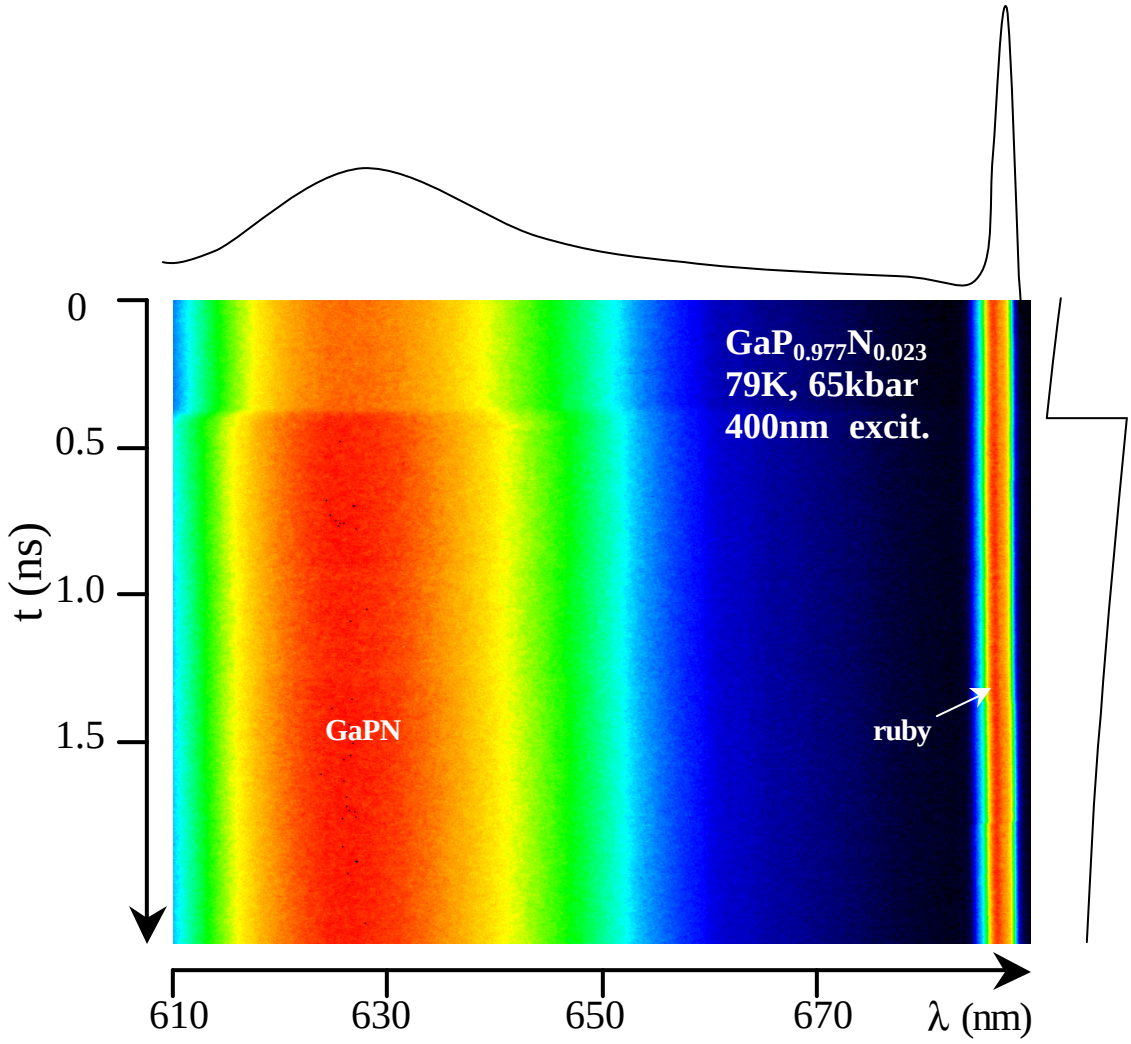


Fig.3.38 Typical time-resolved PL image of a GaPN sample. The curves plotted on the upper and right margin show schematically the time-integrated PL as a function of wavelength and the wavelength-integrated PL as a function of time. The laser pulse excites at $t \approx 0.4$ ns.

For a better understanding of the nature of the luminescence at different pressures, the PL lifetime is an important characteristic quantity. Figure 3.38 shows the typical time-resolved PL of a GaPN sample at 79K. The spectrum can be integrated over time or wavelength and the spectral or temporal dependencies of the luminescence are thus obtained. The sharp PL peak at ~690nm is due to the ruby luminescence used for pressure

calibration. The broad emission band at shorter wavelengths is due to the inter-band transition from the GaPN sample. The lifetime can be determined from the decay kinetics of its wavelength-integrated PL intensity. Shown in the inset of Fig. 3.39 is the time-resolved PL intensity of $GaP_{0.977}N_{0.023}$ at different pressures. It can be seen that the lifetime of the PL is much longer than the duration that can be measured with our equipment. However, although the PL does not show considerable decay within our measurement time window (~ 2 ns), the height of the step in the time-resolved PL curve generated by the excitation pulse shows a quite reproducible trend as a function of pressure. Considering the time interval of 13.2 ns between sequential excitation pulses, the step height can be used to estimate the lifetime of the PL assuming a single exponential temporal decay. The obtained lifetime is plotted in Fig. 3.39 as a function of pressure. Also shown is the pressure dependence of the PL intensity. Although the mechanisms of non-radiative recombination in these alloys have not been determined at this stage, it can be seen that both the lifetime and the PL intensity change abruptly at ~ 80 kbar, *i.e.*, the pressure where the peak energy of the PL reaches its maximum. This phenomenon further confirms the change in the nature of the lowest conduction band edge at this pressure.

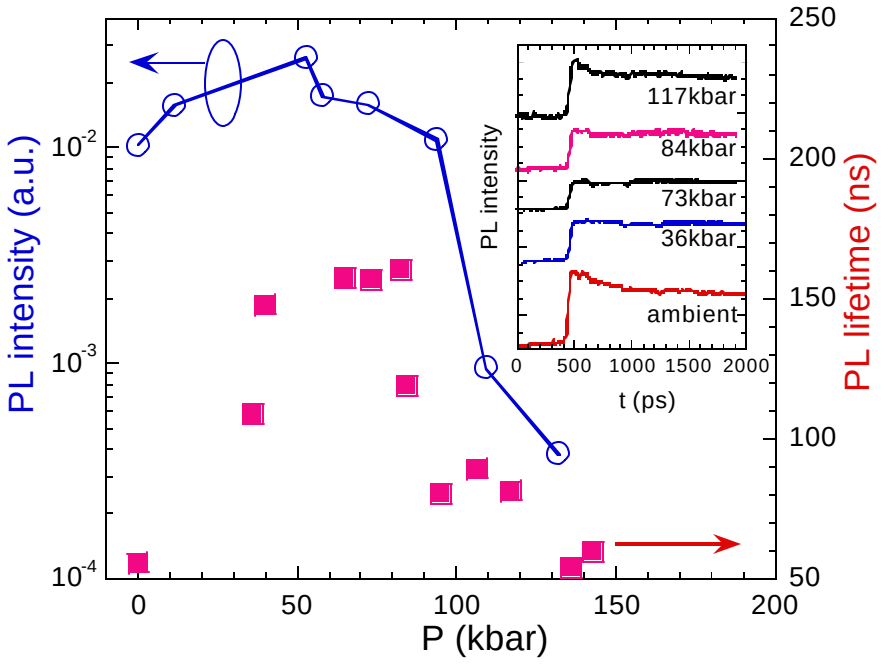


Fig.3.39 The lifetime of the PL of $GaP_{0.977}N_{0.023}$ as a function of pressure at 79K. The pressure dependence of the PL integrated intensity at 30K is also shown. Inset, the time-resolved PL curve evolving with pressure.

Although considerably weaker, the emission due to indirect transitions is still possible, because the localized N centers partially break the translational invariance of the crystal and relax the wavevector conservation requirement. Green's function calculations have shown an energy broadening of ~10 meV due to the N-atom scattering at the edge of the lower subband for $GaAs_{0.95}N_{0.05}$ [38]. The N-induced relaxation of the ***k***-vector conservation also allows intraband scattering within the lowest conduction subband. As is seen in Fig. 3.37, the measured PL peak energy makes a smooth transition between the low and high pressure regimes, rather than showing a kink as on the calculated curves. This fact suggests a strong mixing between the $E_{N\Gamma}$- and $E_{NX}$-conduction band minima when they are degenerate in energy. The best agreement with the data, as denoted by solid lines, was obtained by using the previously determined [6]

coupling constant $V_{N\Gamma}$=3.05eV at the Γ point and setting $V_{NX}$=0.90eV for the coupling constant at the Brillouin zone edge. The energy of the N localized state was set to be at $E_N$ ~ 2.15eV with a small pressure dependence of 1.2 meV/kbar. This energy location and pressure dependence are consistent with the average values for the variety of bound exciton lines in dilute N-doped GaP observed in previous reports [5, 80]. Although X states could be expected to be more concentrated than Γ states on the group V sites (where N substitutes), the X-N coupling is much weaker than the Γ-N coupling. As pointed out in Ref.[81], this is partly because X states are essentially antibonding *p*-like, while Γ states are *s*-like with the same $A_1$ symmetry as the N localized state.

Evidence of similar off-zone-center coupling in $GaAs_{1-x}N_x$ alloy has been observed by Seong *et.al.* using resonant Raman scattering [82] and by Perkins *et.al.* using the electroreflectance technique [83]. In these ambient-pressure experiments, a coupling between $E_N$ and the conduction band edge $E_L$ at the L point of the Brillouin zone was observed. This is because in GaAs, the $E_N$ level is closer to the L band minima ($E_L$-$E_N$=0.12 eV) than to the X minima ($E_X - E_N$ = 0.27 eV), whereas in GaP $E_N$ is located much closer to the X band minima than to the L minima, $E_X$ - $E_N$ = 0.17 eV and $E_L$ - $E_N$ = 0.46 eV. In GaAs, the negative pressure derivative resulting from the coupling between $E_N$ levels and $E_X$ minima can be observed only at very large pressures when the X band minimum shifts down to the band edge. In fact, the onset of this effect has been observed in $GaAs_{1-x}N_x$ at a pressure of about 120 kbar [50] (see Fig. 3.8).

In order to calculate the BAC effect over the entire Brillouin zone, the interaction constant *V* has to be known as a function of wavevector. The hybridization parameter is essentially the Fourier transform of the interaction matrix element between the localized

impurity state and the Wannier function of the band [39]. In the Green's function calculation in section 3.3, the $\boldsymbol{k}$ dependence of $V_{\boldsymbol{kj}}$ is assumed to be weak on the momentum scale we are interested in. In Eq.(3.12), the parameter $V_{\boldsymbol{kj}}$ is averaged over the impurity sites and in $\boldsymbol{k}$ space. In the simplest case, all the impurity atoms are of the same type, so that the $\boldsymbol{j}$ dependence of $V_{\boldsymbol{kj}}$ is removed. The $\boldsymbol{k}$ dependence of $V_{\boldsymbol{kj}}$ can be estimated from Eq.(3.2). Assuming that the Hartree-Fock energy varies slowly in space and can be replaced by a constant $e_{HF}$, we have

$$V_k = e_{HF} \cdot \sum_l e^{i\boldsymbol{k}\cdot\boldsymbol{l}} \int a^*(\boldsymbol{r}-\boldsymbol{l}) j_d(\boldsymbol{r}) d\boldsymbol{r}. \tag{3.52}$$

Due to the localized character of both $a(\boldsymbol{r})$ and $j_d(\boldsymbol{r})$, the overlap integral in Eq.(3.52) is essentially zero when $a(\boldsymbol{r})$ and $j_d(\boldsymbol{r})$ are located on two sites far apart from each other. In an attempt to model the $\boldsymbol{k}$-dependence of $V_{\boldsymbol{k}}$, we replace the integral in Eq.(3.52) by an exponentially decaying function $\sim \exp(-l/l_d)$, and obtain

$$V_k = e_{HF} \sum_l e^{i\boldsymbol{k}\cdot\boldsymbol{l}} e^{-l/l_d} = \frac{V_0}{\left(1+l_d^2 k^2\right)^2}. \tag{3.53}$$

Experimental evidence indicates that the values of $V_{\boldsymbol{k}}$ at the L point in $GaAs_{1-x}N_x$ [83] and at the X point in $GaP_{1-x}N_x$ [84] are about 3 ~ 4 times smaller than the $V_{\boldsymbol{k}}$ at the $\Gamma$ point. This ratio corresponds to a wavefunction decay length ($l_d$) of the order of the lattice constant, which is consistent with the strongly localized nature of the N states. This result also demonstrates that the off-zone-center conduction band minima are affected by the anticrossing interaction only when their energies are close to the localized level.

Shown in Fig.3.40 is a schematic diagram of the conduction band of $GaP_{0.977}N_{0.023}$ at ambient pressure. The energy minima restructured from the $\Gamma$-N and X-N anticrossing

interactions at 100 kbar are also shown in symbols. The fundamental bandgap of the material changes from direct at ambient pressure to indirect at high pressures. In this BAC calculation, the dispersion relations are obtained by substituting the wavevector-dependent interaction constant into Eq.(3.26).

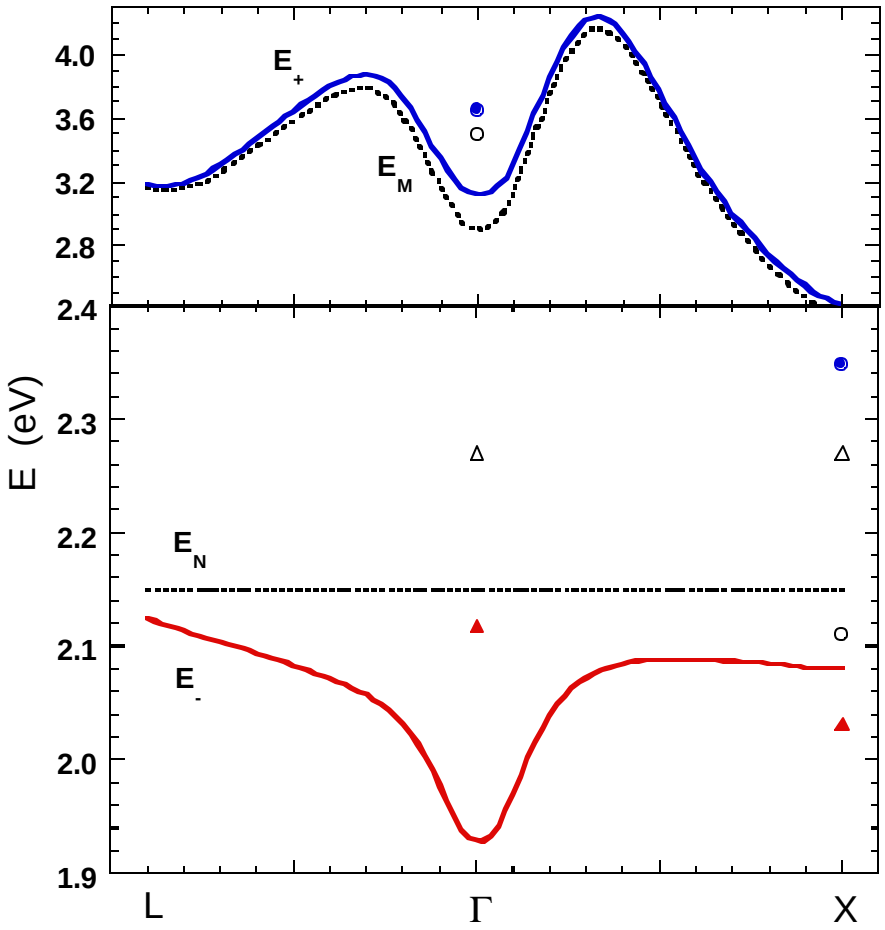


Fig.3.40 BAC-caused restructuring of the conduction band of $GaP_{1-x}N_x$. The curves show the lower $E_-(k)$ and the upper $E_+(k)$ band edges at ambient pressure. The symbols show the energy minima at 100kbar: open triangles, $E_N$; open circles, $E_M$ (including $E_\Gamma$ and $E_X$); solid triangles, $E_-$ (including $E_{N\Gamma-}$ and $E_{NX-}$); solid circles, $E_+$ (including $E_{N\Gamma+}$ and $E_{NX+}$). Note the change in the nature of the lowest conduction band edge, from direct at ambient pressure to indirect, mostly X-like at 100 kbar.

Figure 3.41 shows the ambient-pressure bandgap energy of four samples with different N concentrations measured using PL at 30K. The lowest solid line represents the N-like conduction band minimum of $GaP_{1-x}N_x$ restructured through the interaction between $|N\rangle$ and $|\Gamma\rangle$ as calculated from Eq.(3.26). Also shown in solid lines are the predicted energy of the other minimum restructured from the interaction between $|N\rangle$ and the X band, and two higher energies corresponding to the X-like and Γ-like edges of the upper subbands calculated from Eq.(3.26). These higher critical energies may be observed by modulation spectroscopy.

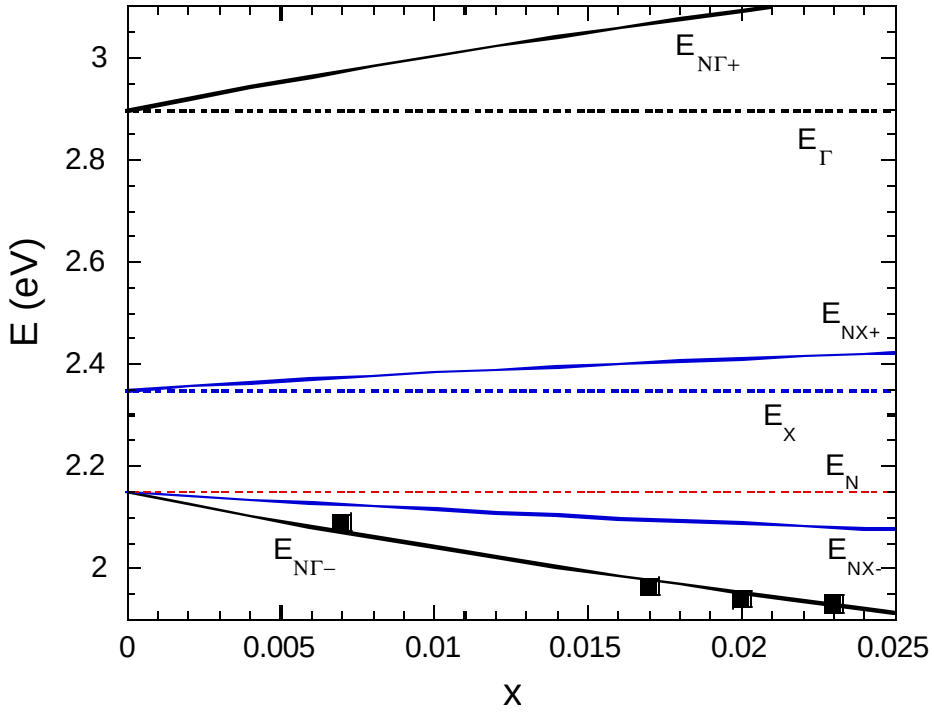


Fig.3.41 PL peak energy at 30K and ambient pressure of four GaPN samples as a function of N concentration. The dashed lines mark the energy locations of the N state, the Γ band, and the X band minima of GaP. The solid lines are the energies of the subbands edges as a result of the band anticrossing repulsion.

Summarizing this section, photoluminescence measurements have been performed on $GaP_{1-x}N_x$ alloys at 30K. Based on the non-monotonic pressure dependence of the PL peak energy, it is demonstrated that the fundamental bandgap in $GaP_{1-x}N_x$ changes its nature from direct to indirect at high pressures. The anticrossing repulsion between the N localized state and the X conduction minima of the host GaP explains the negative pressure dependence of the fundamental band gap at high pressures. The coupling between the N localized state and the $\Gamma$ band states is more than three times stronger than the coupling between the N localized state and the X band states. This finding accounts for a number of previous observations indicating that the off-zone-center minima are affected only when their energies lie close to the localized N-level energy.

# 4. Highly-mismatched Semiconductor Alloys: Group II-VI Based

## 4.1 Conduction Band Anticrossing (CBAC) in II-VI Alloys

The classification scheme of the semiconductor alloys based on the electronegativity mismatch applies not only to III-V compounds, but also to II-VI compounds. For example, according to Tab.3.1, ZnSeS belongs to lightly mismatched alloys because there is only a small electronegativity difference between S and Se (0.1 eV). Figure 4.1 shows the composition dependence of the low-temperature band gap of ZnSeS alloys on the ZnSe rich side. The bowing parameter is ~ 0.3 eV, indicating a small deviation from the VCA prediction, similar to the case of GaAsP shown in Fig. 3.2. As a comparison and a typical example of more mismatched II-VI alloys, Fig.1.1 shows the large band gap bowing of $ZnSe_{1-x}Te_x$. The bowing parameter is ~ 1.2 eV, much larger than that of the ZnSeS system.

Effects of the electronegativity mismatch are reflected not only in the bandgap bowing. Because states with different characters have different pressure behaviors, the pressure dependence of optical transition energies is widely used to study the nature of the states involved in the transition. Shown in Fig. 4.2 is the pressure dependence of the band gap of $ZnSe_{0.95}S_{0.05}$ measured by optical absorption at room temperature. The pressure dependence of the band gap of ZnSe is also shown as a comparison. These pressure curves are fitted to a second order polynomial of the pressure. It can be seen from the figure that the pressure dependencies of these two materials are very similar. For example, the linear pressure coefficient of $ZnSe_{0.95}S_{0.05}$ differs from that of ZnSe by 2%

only. For more highly mismatched alloys, this difference can be much larger. For example, 4% ZnSe alloyed with ZnTe results in a reduction as large as 10% in the linear pressure coefficient, as will be shown in the following text.

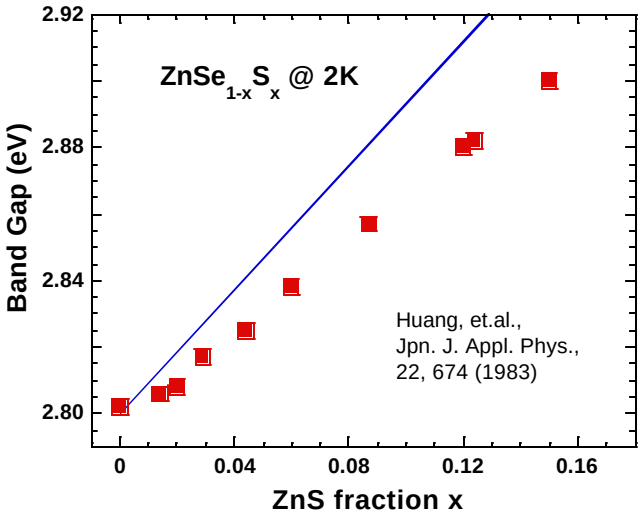


Fig. 4.1 Bandgap as a function of composition for ZnSeS alloys. The solid line represents the linear prediction.

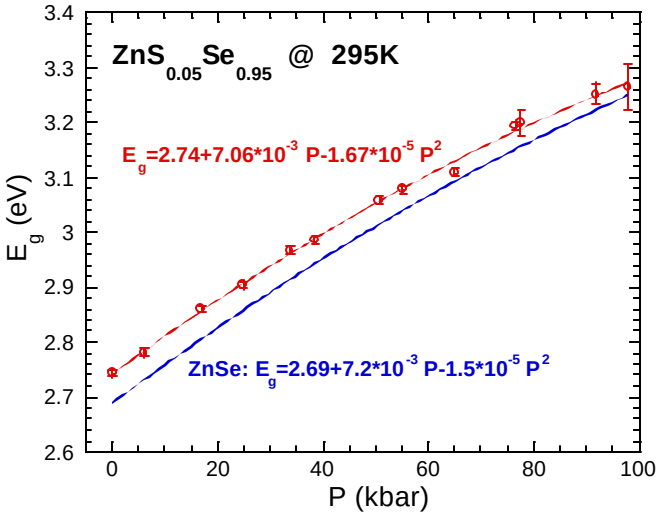


Fig.4.2 Room-temperature energy gap as a function of pressure for $ZnSe_{0.95}S_{0.05}$ and ZnSe.

The large bandgap bowing has been attributed traditionally in part to the nonlinearity of the electronic band structure associated with the matrix elements of the VCA potential and in part to compositional and structural disorder [85]. The recently discovered BAC model offers a different approach to an understanding of the same effect. The BAC model has been used to explain successfully the electronic properties of III-V-N alloys where a very large bowing of the bandgap is observed [33,34]. In the context of this work, it is of great interest to study the generality of the applicability of the BAC model, and inquire if the interaction is not an isolated effect but also occurs in other systems with large bandgap bowing parameters. The most important feature of the III-V-N alloys is that the highly electronegative N atoms introduce localized $A_1$ levels close to the conduction band edges (CBE's) of III-V compounds. The interaction of these levels with the extended states of the conduction band strongly affects the electronic states that determine the basic electrical and optical properties of the alloys. Most notably the interaction produces a downward shift of the lowest CBE, which leads to the large bowing of the fundamental bandgap. Unfortunately, the N content in currently available $GaAs_{1-x}N_x$ as well as in other group III-V-N alloys is limited to several atomic percent, precluding the use of these alloys to study the large bandgap bowing effects over the whole composition range. To overcome this limitation, we have chosen to study the alloys $ZnSe_{1-x}Te_x$ and $ZnS_{1-x}Te_x$. These alloys also exhibit large bandgap bowing effects and are readily available over the whole composition range. In Te-rich $ZnSe_{1-x}Te_x$ and $ZnSe_{1-x}Te_x$ ($x$ close to 1), similar effects are expected as metallic Te atoms are partially replaced by much more electronegative S or Se atoms.

Shown in Fig.4.3 is the CBE of Te-rich ZnSTe and ZnSeTe measured by optical absorption as a function of hydrostatic pressure, reported by Walukiewicz *et*. *al* [20]. A remarkable feature of the data shown in Fig.4.3 is a strongly nonlinear shift of the absorption edge with increasing pressure that clearly resembles the pressure dependence of the fundamental band gap previously observed in GaAsN alloys [34,50].

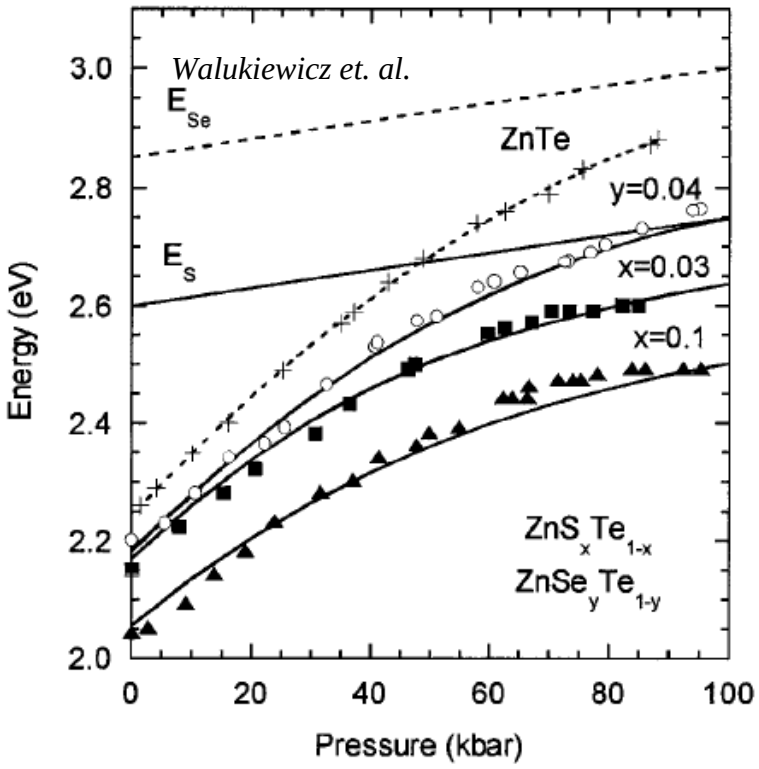


Fig.4.3 Dependence of the CBE in Te-rich ZnSTe and ZnSeTe on pressure [20]. The solid lines represent the dependencies calculated using the BAC model. The energies of the localized S and Se-derived $A_1$ states are also shown. All the energies are relative to $E_v$(ZnTe) at ambient pressure. Note that in this graph the Te concentration is represented by 1-*x* (in ZnSTe) or 1-*y* (in ZnSeTe), in different notation as in this thesis.

It has been shown in the case of III-V-N alloys that the localized, N-derived $A_1$ states interact primarily with the conduction band [33,34,50]. The valence band states experience only a gradual shift expected from a linear interpolation between the end-point compounds. Since the available III-V-N alloys are limited to very low N concentrations, it has been a good approximation to assume that N does not have any effect on the valence band structure [50]. However, since the II-VI alloys studied here cover a relatively wide range of S or Se contents, we need to decompose the total shifts of the conduction and the valence band edges (VBE's) into their linear parts given approximately by the VCA, and the nonlinear parts associated with the large bowing. The linear contributions to the band edge (including the spin-orbit valence band edge) shifts are calculated from the known VBE offsets [86]. With the known locations of $E_v^{VCA}$ as a function of composition, we can determine the composition dependent energy of the CBE from the measured energy gaps.

The strongly nonlinear pressure dependence of the band gaps shown in Fig. 4.3 indicates a strong interaction between the localized S or Se level with the band states of ZnTe matrix, similar to the situation in GaAsN alloys. We formulate the problem in the following mathematical way that is coherent with a later analysis of the alloy system on the other composition side. We first discuss $ZnSe_{1-x}Te_x$ as an example. For Te-rich ZnSeTe ($x \to 1$), the BAC model predicts a new CBE formed by the anticrossing interaction between the Se localized states and the Γ conduction band of ZnTe [34]. The Hamiltonian matrix of the system can be written as,

$$H_c = \begin{pmatrix} E_c^{Te-rich}(x) & C_{ZnTe-Se}\sqrt{1-x} \\ C_{ZnTe-Se}\sqrt{1-x} & E_{Se} \end{pmatrix}, \qquad (4.1)$$

where $E_c^{Te-rich}(x) = 2.24 - 0.3(1-x)$ is the VCA interpolated value of the CBE on the Te-rich side, referenced to the top of the ZnTe valence bands. The conduction band and valence band offsets between ZnTe and ZnSe are assumed to be 0.7 and 0.3 eV, respectively [86]. $E_{Se}$ is the energy of the Se localized level, and is determined by fitting the calculated results with the data. $C_{ZnTe-Se}$ is the coupling constant between $E_c^{Te-rich}$ and $E_{Se}$. The restructured CBE is given by the lower eigen-values of $H_c$, and has the functional form of the $E_-$ subband as given in Eq.(3.26). The fundamental bandgap on the Te-rich side, $E_g^{Te-rich}(x)$, is given by the energy separation between this restructured CBE and the top of the valence bands that is linearly interpolated between ZnTe and ZnSe VBEs based on their offsets.

In good agreement with existing data [87], the pressure dependence of $E_c$ in the ZnTe matrix shown in Fig. 4.3 can be well described by the relation $E_c(P) = 2.24 + 10.9 \times 10^{-3} P - 4.25 \times 10^{-5} P^2$, where $P$ is the pressure in kbar. The nonlinear term originates from the pressure dependence of the bulk modulus in ZnTe. It is quite evident from the data shown in Fig.4.3 that alloying of ZnTe with both ZnS or ZnSe considerably affects the pressure coefficients. The best fit to the experiment was obtained by assuming that the locations of both the S and the Se levels depend slightly on pressure and are given by $E_{Se} = 2.85 + 1.5 \times 10^{-3} P$ and $E_S = 2.60 + 1.5 \times 10^{-3} P$. It should be noted that this is about the same pressure dependence as the one found for the N level in III-V-N alloys [34, 50]. For both $ZnSe_{1-x}Te_x$ and $ZnS_{1-x}Te_x$ samples, good agreement between the calculations and the experiments is obtained by setting the coupling constant at $C_{ZnTe-Se} \approx C_{ZnTe-S} \approx 1$ eV. The value of the coupling parameter is significantly smaller

than the coupling parameter $V$=2.7 eV used previously to describe the interaction between the N levels and the extended states in $GaAs_{1-x}N_x$ alloys [33,50]. This is not surprising, however, since as can be seen in Tab.3.1, the electronegativity difference between N and As (1.0 eV) is more than 2 times larger than between Se and Te (0.3 eV).

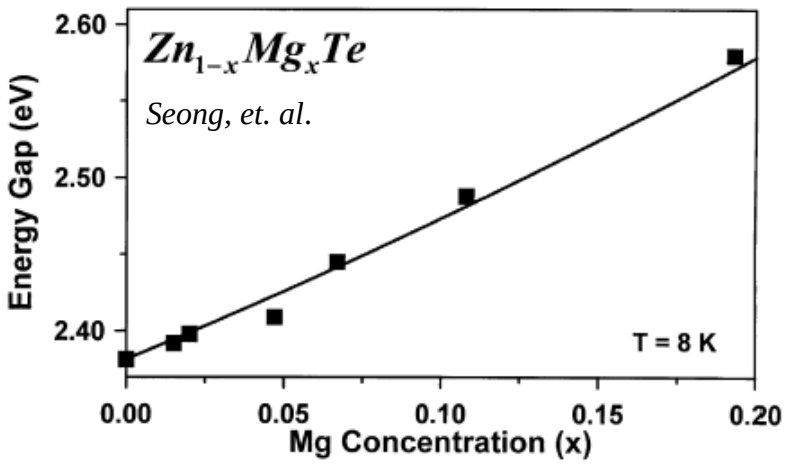


Fig.4.4 The energy gap of $Mg_xZn_{1-x}Te$ measured by PR as a function of $x$ [88].

The perturbation of the Se and S localized states on the ZnTe conduction band described by the matrix in Eq.(4.1) thus accounts successfully for the hydrostatic pressure dependence of the fundamental bandgap on the Te-rich side. It also explains why the large bowing parameters are observed only in the alloys involving highly electronegative elements (anion alloys) and are much smaller when more metallic elements are exchanged (cation alloys). As can be seen in Fig.2.1, the localized $A_1$ levels of more metallic atoms have higher energies and thus only very weakly interact with the CBE states. A good example of the later case is ZnMgTe where only a small bowing parameter is found [88] despite a significant electronegativity difference between Zn (1.5 eV) and Mg (1.2 eV) [13]. The results are shown in Fig.4.4 [88].

To further investigate the different effects of isovalent substitution in these anion and cation II-VI alloys, we extend our studies to $Mg_yZn_{1-y}Te$ and and $Mg_yZn_{1-y}Te_{1-x}Se_x$ alloys to determine if band anticrossing effects are found in alloys with electronegativity-mismatched cations (*i.e.* Mg and Zn). Also, as is seen from Eq.(4.1), the strength of the anticrossing interaction depends on the location of the localized level relative to the band edges of the host matrix. Quaternary alloy systems create the possibility to independently vary the band edge energies and thus the energy difference between the localized level and the conduction band minimum. It is important to determine the applicability of the BAC model to this system. The results show that, indeed, for the anion-mismatched systems the anticrossing interaction is entirely controlled by the location of the conduction band relative to the localized level. It was also found that alloys with significant electronegativity difference on the cation sites do not show nonlinear effects and are well described within the VCA.

Figure 4.5 shows the optical absorption curves of $Mg_{0.10}Zn_{0.90}Te_{0.92}Se_{0.08}$ measured for a range of hydrostatic pressures. The dashed curve at the top represents a PR spectrum taken at room temperature and ambient pressure. The bandgap energy determined from the PR spectrum, 2.28eV, is in agreement with the gap energy defined by the crossing point of the steeply rising portion and the saturation line of the absorption curve. The apparent absorption below the band edge originates from the fact that the reflection of the beam from the surface of the sample has been neglected in the absorbance calculation.

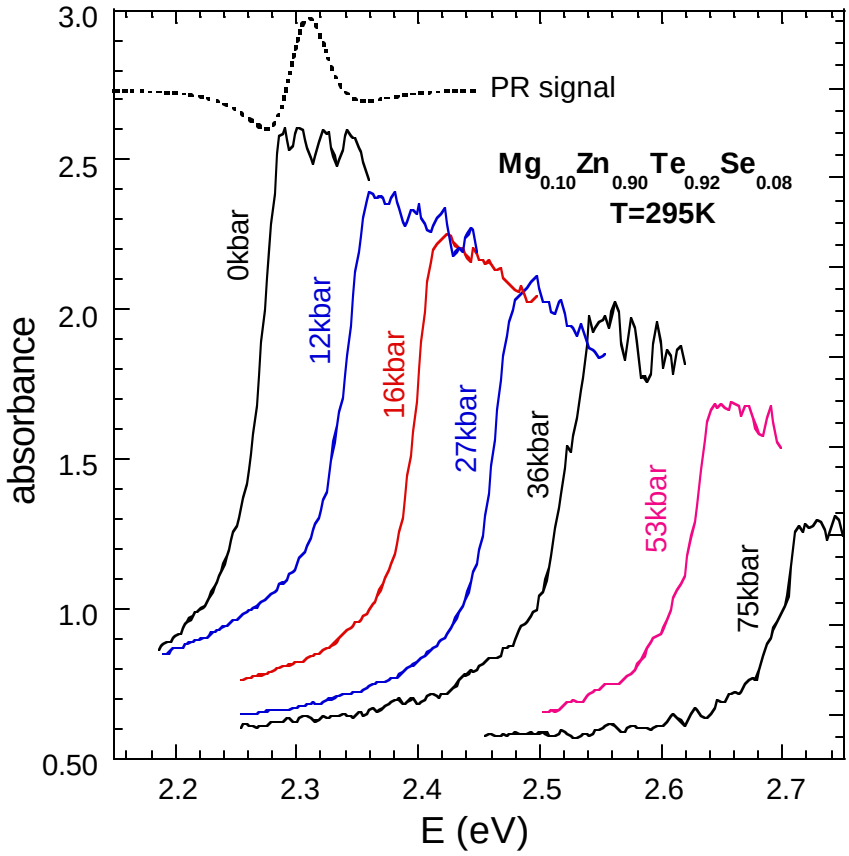


Fig.4.5 Room-temperature optical absorption curves of $Mg_{0.10}Zn_{0.90}Te_{0.92}Se_{0.08}$ at different hydrostatic pressures. The dashed curve in the top portion of the figure is a PR spectrum obtained at ambient pressure.

It is evident from Eq.(4.1) that an analysis of the experimental data in terms of the BAC model requires knowledge of the composition and pressure dependence of $E_{Se}$ and $E_c^{Te\text{-}rich}$. It has been shown previously that energies of highly localized levels remain constant on an absolute energy scale [89]. This means that their energy can be deduced from the known band offsets in a given alloy system [90].

To determine the pressure dependence of the localized level, we have measured oxygen-related PL with unintentionally O-doped $ZnTe_{0.99}Se_{0.01}$. The PL spectra recorded at 30K at different hydrostatic pressures are shown in Fig. 4.6. The broad emission band at low energies (1.8-2.1eV) is associated with the oxygen impurity [91]. The band edge emission at higher energies with its phonon replicas is also clearly seen. The broad, smooth features at higher energies are due to impurity luminescence from the type-I diamonds in the diamond anvil cell. It is clear from Fig. 4.6 that the energy of the oxygen deep level shows a much weaker pressure dependence than the band edge. In Fig. 4.7, the peak energies of the O-related PL and the inter-band PL and their phonon replica are shown as a function of the number of phonons emitted. The linear dependence is clearly seen, and the slopes of the linear dependence that corresponds to the energy of the phonon emitted are essentially the same (~ 26 - 29 meV). This phonon energy is very close to the LO phonon energy of ZnTe listed in the literature (25.6 meV, or 6.2 THz at room temperature) [92]. A linear fit to the no-phonon line of the O-related PL yields the relation $E_{oxy} = 2.0 + 1.3\times10^{-3}\cdot P$ for the pressure dependence of the oxygen level. This pressure coefficient is quite close to the pressure coefficient of the Se localized level used in Fig.4.3, 1.5 meV/kbar [20]. We attribute the small positive pressure coefficient of the localized O level to the pressure-induced downward shift of the VBE.

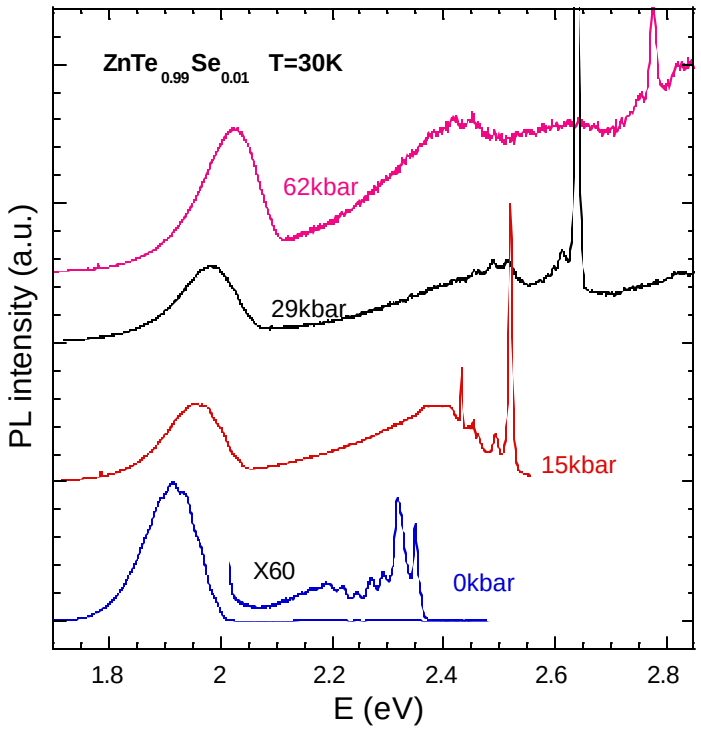


Fig.4.6 Photoluminescence spectrum of an oxygen-containing $ZnTe_{0.99}Se_{0.01}$ sample at 30K.

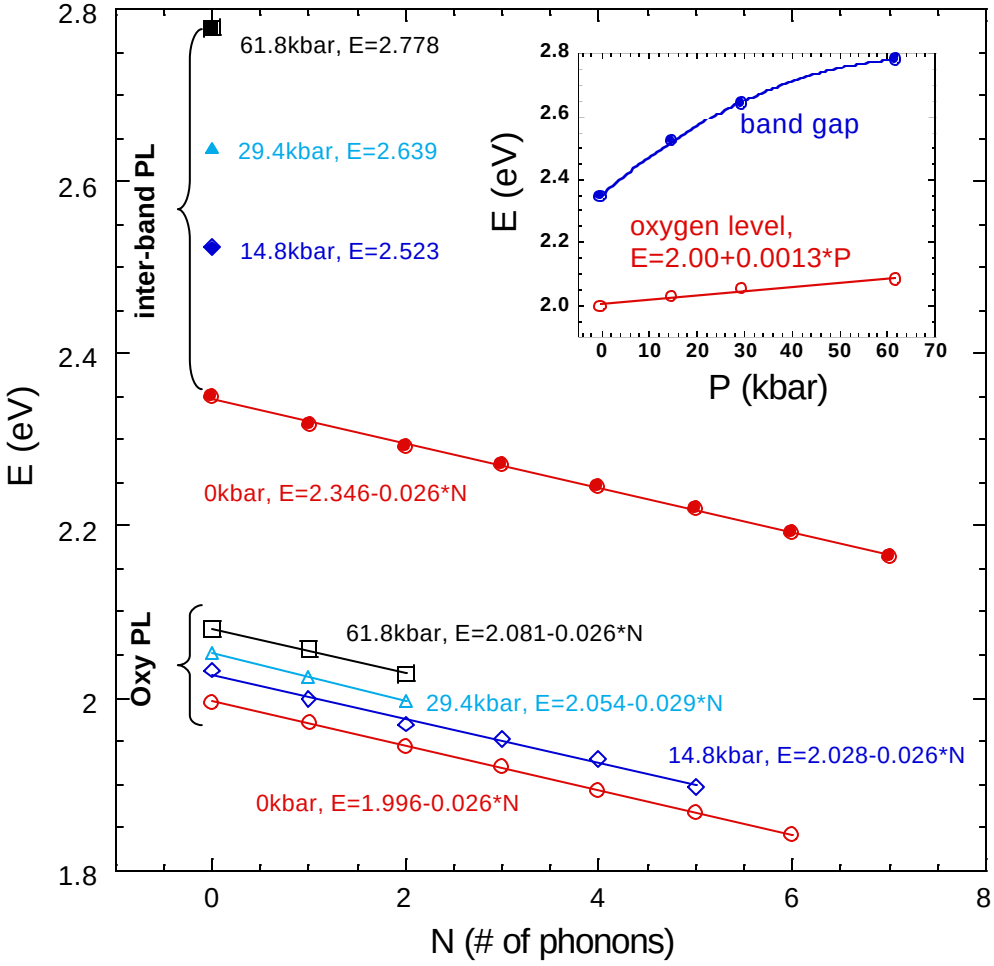


Fig.4.7 The peak energies of the oxygen-related and inter-band PL of $ZnTe_{0.99}Se_{0.01}$ and their phonon replica. The straight lines are linear fits. The inset shows the no-phonon line energy as a function of pressure.

The theoretically calculated [93] valence band offsets $\Delta E_v$(ZnTe/MgTe)=0.73 eV and $\Delta E_v$(ZnTe/ZnSe)=0.76 eV and the known bandgap energies of the end-point compounds were used to determine the location of the CBEs of the host semiconductor matrices. Using the determinations of the composition dependence of the VBEs, we plot in Fig. 4.8 the measured CBE energies relative to a common energy reference, *i.e.*, the

VBE of ZnTe at ambient pressure. It is important to note that the CBE energy in $Mg_{0.185}Zn_{0.815}Te$ has nearly the same pressure dependence as that of ZnTe, showing clearly that the replacement of Zn with less electronegative Mg does not strongly affect the pressure dependence of the resulting alloys. This is consistent with the results presented in Fig.4.4 that show no strong bowing in the composition dependence of the bandgap of $Mg_yZn_{1-y}Te$ alloys [88].

It is also seen in Fig. 4.8 that the presence of Se in either $ZnTe_{0.96}Se_{0.04}$ or $Mg_{0.1}Zn_{0.9}Te_{0.92}Se_{0.08}$ considerably changes the pressure dependence of the CBE energies in these alloys. The observed tendency for the CBE energy to saturate at high pressures is a clear indication of an anticrossing effect between the localized Se level and the extended states of the conduction band. This is in contrast to the case of Mg replacing Zn cations where the same electronegativity difference does not produce any unusual effects. The sudden reduction of the CBE energy in $Mg_{0.1}Zn_{0.9}Te_{0.92}Se_{0.08}$ at the pressure of 85 kbar is attributed to the onset of a pressure-induced phase transition, which has been observed previously in $Mg_yZn_{1-y}Te$ alloys [94].

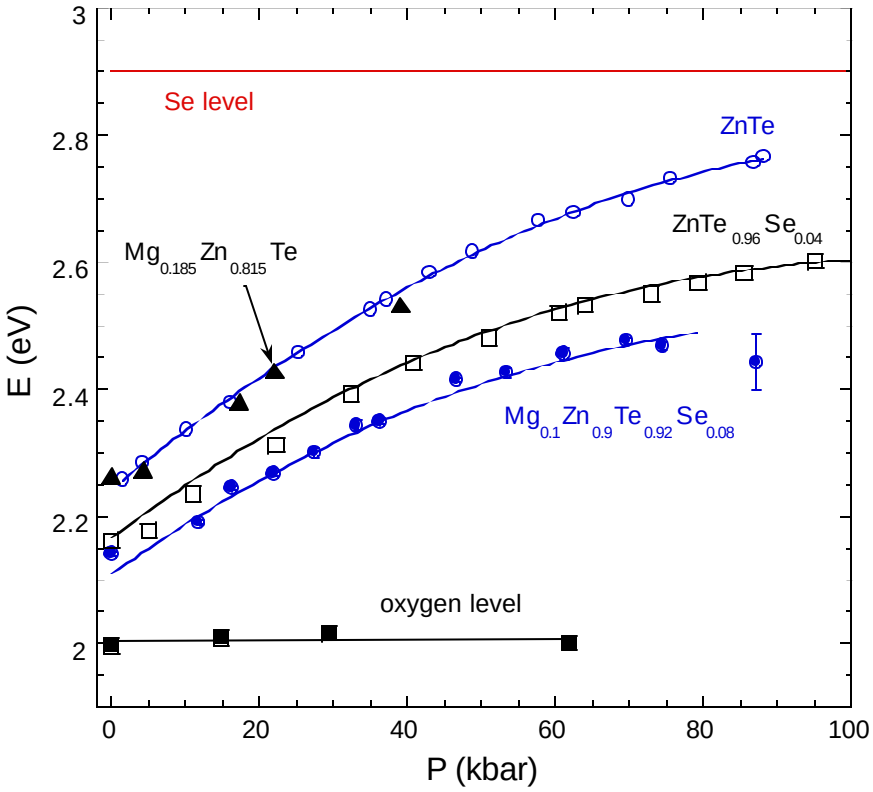


Fig.4.8 Pressure dependencies of the CBE of four compounds with respect to the VBE of ZnTe at ambient pressure. The energy of the Se localized level and the no-phonon-line energy of the oxygen impurity level determined from the PL spectrum in $ZnTe_{0.99}Se_{0.01}$ are also shown. The solid curves through the data points of the two Se-containing samples represent the dependencies calculated using the BAC model. The line through the data points of the ZnTe sample is a quadratic fit. All the data points were obtained at room temperature except for the oxygen deep level data, which were taken at 30K.

The solid lines in Fig. 4.8 are BAC model-based calculations using the pressure and composition dependencies of the host band edge and the localized level discussed above. The best fit with the experiment is obtained with a coupling coefficient $C_{MgZnTe-}$

$_{Se}$=1.1 eV and a Se localized level $E_{Se}$=2.9 eV. These values are in quantitative agreement with the values determined in Fig. 4.3 for $ZnTe_{1-x}Se_x$ ternaries ($C_{ZnTe\text{-}Se}$=1 eV and $E_{Se}$=2.85 eV) [20]. It is important to note that, as is exemplified by the case of the $E_{oxy}$, the energies of the localized levels do not depend on pressure in our present energy reference, *i.e.*, with respect to the ambient-pressure VBE of ZnTe.

The successful, simultaneous fitting of the BAC model to both the Mg-containing and Mg-free samples with nearly the same values of the parameters implies that, unlike alloying with ZnSe, the incorporation of MgTe into ZnTe results in a linear variation of the band edge energies that can be well described by the VCA. Thus, the change in the bandgap of the quaternary alloy $Mg_yZn_{1-y}Te_{1-x}Se_x$ can be decomposed into a linear VCA alloying effect and a nonlinear BAC effect arising from the hybridization between the Se localized level and the VCA conduction band edge.

An extreme case of electronegativity mismatch between the alloy constituents, is represented by group II-VI-O system in which highly electronegative oxygen (electronegativity=3.5 eV) [14] partially substitutes other group VI elements. A large BAC effect is expected in this system as it is a direct analog of group III-V-N alloys. Indeed, it is now well established that substitutional oxygen introduces localized states close to the CBE in many II-VI compounds [91]. The epitaxial growth of O-containing II-VI alloys has turned out to be a difficult task. The achievable concentrations of O dopant are too low to clearly show any alloying effects. We have successfully synthesized $Cd_{1-y}Mn_yO_xTe_{1-x}$ quaternary alloys by using the ion implantation technique, followed by a rapid thermal annealing treatment to activate the implanted O atoms [95].

The band gap of these alloys is shifted downward from that of the O-free ternaries, in agreement with the predictions of the BAC model. The results are summarized in Fig.4.9.

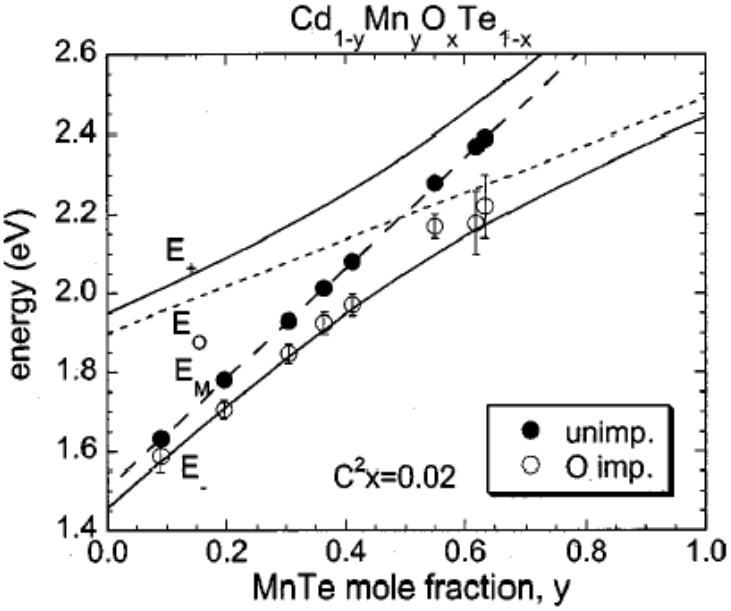


Fig.4.9 Room temperature band gap energies of un-implanted and O-implanted $Cd_{1-y}Mn_yTe$ samples as a function of $y$ for $0.1<y<0.64$. The known dependencies of the conduction band minima on the MnTe mole fraction and the estimate of oxygen level on $y$ are also shown. The solid lines are the upper and lower subbands calculated by the BAC model using a $C^2 x$ value of 0.02.

## 4.2. The Entire composition Range of ZnSeTe and ZnSTe

It has been shown in the last section that the bandgap reduction observed in these alloys on the Te-rich side ($x > \sim 0.8$) can be explained by the conduction band anticrossing (CBAC) model [20]. In this section, we show that the predominant bowing mechanism in these systems over the entire composition range is driven by the localized nature of the states of the minority alloy element, specifically the presence of a Te level above the VBE at low $x$ and the presence of a Se or S level above the CBE at high values of $x$. By considering the interactions between these localized levels and the extended states using the BAC model, the behaviors of the bandgap, valence and conduction band shifts, and the spin-orbit splitting are accurately predicted.

### 4.2.1. Experimental Observations

Figure 4.10 shows typical PR spectra obtained from the $ZnSe_{1-x}Te_x$ alloys with several compositions. Two features can be clearly identified in these spectra. The one at lower energy ($E_g$) corresponds to the critical transition from the top of the degenerate heavy-hole (*hh*) and light-hole (*lh*) valence bands to the CBE, and the one at higher energy ($E_g + \Delta_0$) is attributed to the transition from the top of the spin-orbit (*so*) split valence band to the CBE. The fundamental bandgap and the spin-orbit splitting of $ZnSe_{1-x}Te_x$ are shown as a function of composition in Fig. 4.11. The data shown in Fig. 4.11 are in quantitative agreement with previous measurements by electro-reflectance spectroscopy [96] and photoconductivity methods [97]. The energy gap shows a convex

dependence on the Te concentration with a significant deviation from the linear dependence as predicted by the VCA. The spin-orbit splitting, in contrast, shows a concave dependence on the alloy composition. $\Delta_0$ increases rapidly for small $x$ until $x \sim 0.5$. The different behavior of $\Delta_0$ on the Se-rich and the Te-rich side suggests different origins of the bandgap bowing in Se- and Te-rich $ZnSe_{1-x}Te_x$ alloys. The notion of a different origin of the bandgap bowing on the Te- and Se-rich side is further supported by the large asymmetry in the composition dependence of the PR linewidth shown in the inset of Fig. 4.10.

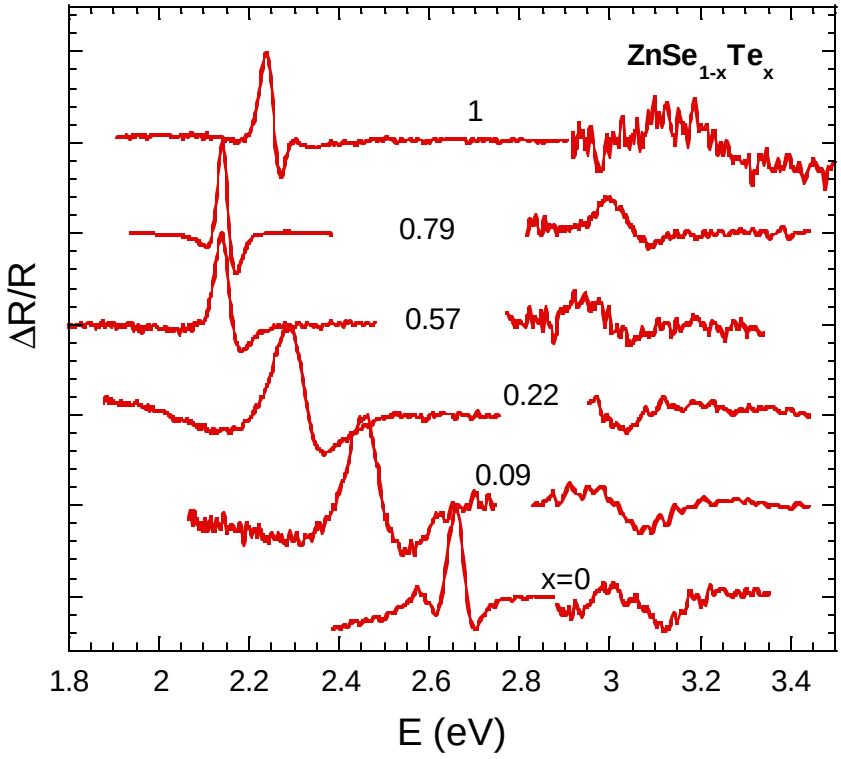


Fig. 4.10 Typical PR spectra of ZnSeTe alloys over the entire composition range.

In Te-rich alloys ($x \rightarrow 1$), the large reduction of the bandgap can be explained by the CBAC model. The model predicts a new CBE that forms by the anticrossing

interaction between the Se localized states and the Γ conduction band of ZnTe [20]. Due to the large energy separation between the Se localized level and the valence bands, the valence bands are not involved in this localized-extended anticrossing interaction; *i.e.*, the energies of the VBE and the spin-orbit splitting follow the VCA interpolations between the values of ZnSe and ZnTe. The fundamental bandgap on the Te-rich side, $E_g^{Te-rich}(x)$, is given by the energy separation between the restructured CBE and the top of the valence bands. The perturbation of the Se localized states on the ZnTe conduction band described in Eq.(4.1) explains successfully the composition and hydrostatic pressure dependencies of the fundamental bandgap on the Te-rich side [20].

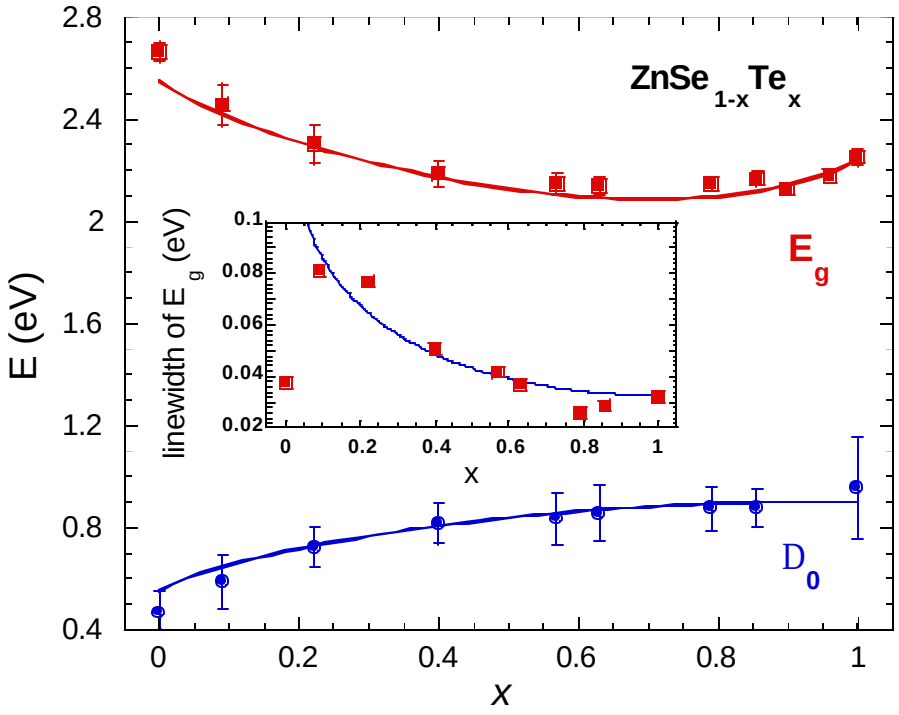


Fig. 4.11 Band gap and spin-orbit splitting as a function of composition as determined from Fig. 4.10. Inset, the composition dependence of the PR linewidth. The lines are fits based on the interpolation between the CBAC and VBAC model (see text).

4.2.2. Valence band Anticrossing (VBAC) in ZnSeTe and ZnSTe

For Se-rich alloys ($x \to 0$), the rapid increase in $\Delta_0$ at small $x$ implies that the incorporation of ZnTe in ZnSe perturbs the valence bands. It is known [98] that an isoelectronic Te impurity substituting Se in ZnSe forms a localized level above the VBE. At dilute concentrations, the Te level gives rise to a strong broad luminescence line below the bandgap [98]. In close analogy to the anticrossing effect between the Se localized level and the ZnTe conduction band on the Te-rich side [20], we consider the hybridization between the localized Te level and the valence bands of the host material. The original four $\Gamma_8$ and two $\Gamma_7$ valence bands are described by the conventional 6×6 Kohn-Luttinger $\boldsymbol{k} \cdot \boldsymbol{p}$ matrix [99] with band-edge energies set at corresponding VCA values. An 8×8 Hamiltonian matrix is formed by augmenting the 6×6 matrix with two localized Te states with energy $E_{Te}$ and opposite spins. The valence band restructuring is computed by diagonalizing this 8×8 matrix. Specifically, we choose as a basis the following six time-reversal symmetry-invariant wavefunctions [99] for the valence bands and the two Te states with opposite spins for the Te localized level,

$$
\begin{aligned}
&\left|\frac{3}{2},\frac{3}{2}\right\rangle=\frac{1}{\sqrt{2}}\left|(X+iY)\uparrow\right\rangle,\\
&\left|\frac{3}{2},\frac{1}{2}\right\rangle=\frac{i}{\sqrt{6}}\left|(X+iY)\downarrow-2Z\uparrow\right\rangle,\\
&\left|\frac{3}{2},-\frac{1}{2}\right\rangle=\frac{1}{\sqrt{6}}\left|(X-iY)\uparrow+2Z\downarrow\right\rangle,\\
&\left|\frac{3}{2},-\frac{3}{2}\right\rangle=\frac{i}{\sqrt{2}}\left|(X-iY)\downarrow\right\rangle,\\
&\left|\frac{1}{2},\frac{1}{2}\right\rangle=\frac{1}{\sqrt{3}}\left|(X+iY)\downarrow+Z\uparrow\right\rangle,\\
&\left|\frac{1}{2},-\frac{1}{2}\right\rangle=\frac{i}{\sqrt{3}}\left|(-X+iY)\uparrow+Z\downarrow\right\rangle,\\
&\left|E_{Te}\uparrow\right\rangle=\left|E_{Te}\right\rangle\uparrow,\\
&\left|E_{Te}\downarrow\right\rangle=\left|E_{Te}\right\rangle\downarrow.
\end{aligned}
\tag{4.2}
$$

In this basis the Hamiltonian matrix can be written as [99],

$$
H_v=\begin{pmatrix}
H & a & b & 0 & \frac{ia}{\sqrt{2}} & -i\sqrt{2}b & \frac{(1+i)}{\sqrt{2}}V & 0\\
* & L & 0 & b & \frac{iD}{\sqrt{2}} & \frac{i\sqrt{3}a}{\sqrt{2}} & -\frac{i\sqrt{2}}{\sqrt{3}}V & \frac{(-1+i)}{\sqrt{6}}V\\
* & * & L & -a & -\frac{i\sqrt{3}a^{*}}{\sqrt{2}} & \frac{iD}{\sqrt{2}} & \frac{(1-i)}{\sqrt{6}}V & \frac{\sqrt{2}}{\sqrt{3}}V\\
* & * & * & H & -i\sqrt{2}b^{*} & -\frac{ia^{*}}{\sqrt{2}} & 0 & \frac{(1+i)}{\sqrt{2}}V\\
* & * & * & * & S & 0 & \frac{1}{\sqrt{3}}V & \frac{(1+i)}{\sqrt{3}}V\\
* & * & * & * & * & S & -\frac{(1+i)}{\sqrt{3}}V & \frac{i}{\sqrt{3}}V\\
* & * & * & * & * & * & E_{Te} & 0\\
* & * & * & * & * & * & * & E_{Te}
\end{pmatrix}.
\tag{4.3}
$$

In this 8×8 matrix, the parameters involved are defined in the following,

$$
\begin{aligned}
H &= -\frac{\hbar^2}{2m_0}\left[\left(k_x{}^2 + k_y{}^2\right)\left(g_1 + g_2\right) + k_z{}^2\left(g_1 - 2g_2\right)\right], \\
L &= -\frac{\hbar^2}{2m_0}\left[\left(k_x{}^2 + k_y{}^2\right)\left(g_1 - g_2\right) + k_z{}^2\left(g_1 + 2g_2\right)\right], \\
a &= \sqrt{3}\frac{\hbar^2}{m_0}\left[k_z\left(k_x - ik_y\right)g_3\right], \\
b &= \frac{\sqrt{3}}{2}\frac{\hbar^2}{m_0}\left[\left(k_x{}^2 - k_y{}^2\right)g_2 - 2ik_xk_yg_3\right], \\
D &= L - H, \\
S &= \frac{1}{2}\left(L + H\right) - \Delta_0,
\end{aligned}
\tag{4.4}
$$

where $\boldsymbol{k}$ is the wavevector, and the $g$ vector and $\Delta_0$ are the the Kohn-Luttinger parameters and the spin-orbit splitting for the valence bands, respectively. $V$ is the hybridization energy between the Te localized states and the three wavefunctions of the $\Gamma_4$ representation of the $T_d$ crystal group,

$$
V \equiv \left\langle Te\middle|U\middle|X\right\rangle = \left\langle Te\middle|U\middle|Y\right\rangle = \left\langle Te\middle|U\middle|Z\right\rangle = C_{ZnSe-Te}\sqrt{x}\,. \tag{4.5}
$$

In Eq.(4.5), a similar square-root dependence on the impurity concentration is assumed as in the previously considered case of the conduction band hybridization [20]. $C_{ZnSe-Te}$ is a parameter that describes the coupling strength and is to be determined by fitting with experimental data. The energy levels are given by the four doubly-degenerate eigen-values of $H_v$. In the Brillouin zone center, they can be labeled according to the nature of their wavefunctions as $E_{Te-like}$, $E_{hh-like}$, $E_{lh-like}$, and $E_{so-like}$ in the order of descending eigen-energy. Since the energy level of the Te localized states is located above the top of the original valence band, a new VBE is formed at energy $E_{Te-like}$. The fundamental bandgap in Se-rich $ZnSe_{1-x}Te_x$, denoted as $E_g^{Se-rich}(x)$, is attributed to the transition between the VCA conduction band edge and this newly-formed VBE. The spin-orbit

splitting is given by the energy separation between $E_{Te-like}$ and $E_{so-like}$. We note that the orthogonality between opposite spin states leads to two zero-valued off-diagonal matrix elements in Eq.(4.3), *i.e.*, $\langle Te\downarrow|\frac{3}{2},\frac{3}{2}\rangle$, $\langle Te\uparrow|\frac{3}{2},-\frac{3}{2}\rangle$ and their Hermite conjugate elements. As a result, the heavy-hole band does not mix with the Te states at the Γ point, and the energy of the heavy-hole band edge remains unchanged. The light-hole and spin-orbit valence band edges, on the other hand, are pushed downward by the anticrossing repulsion from the up-lying Te level. The energy degeneracy between the heavy-hole and the light-hole bands at Γ point is thus removed. The band restructuring in the whole composition range is schematically shown in Fig. 4.12.

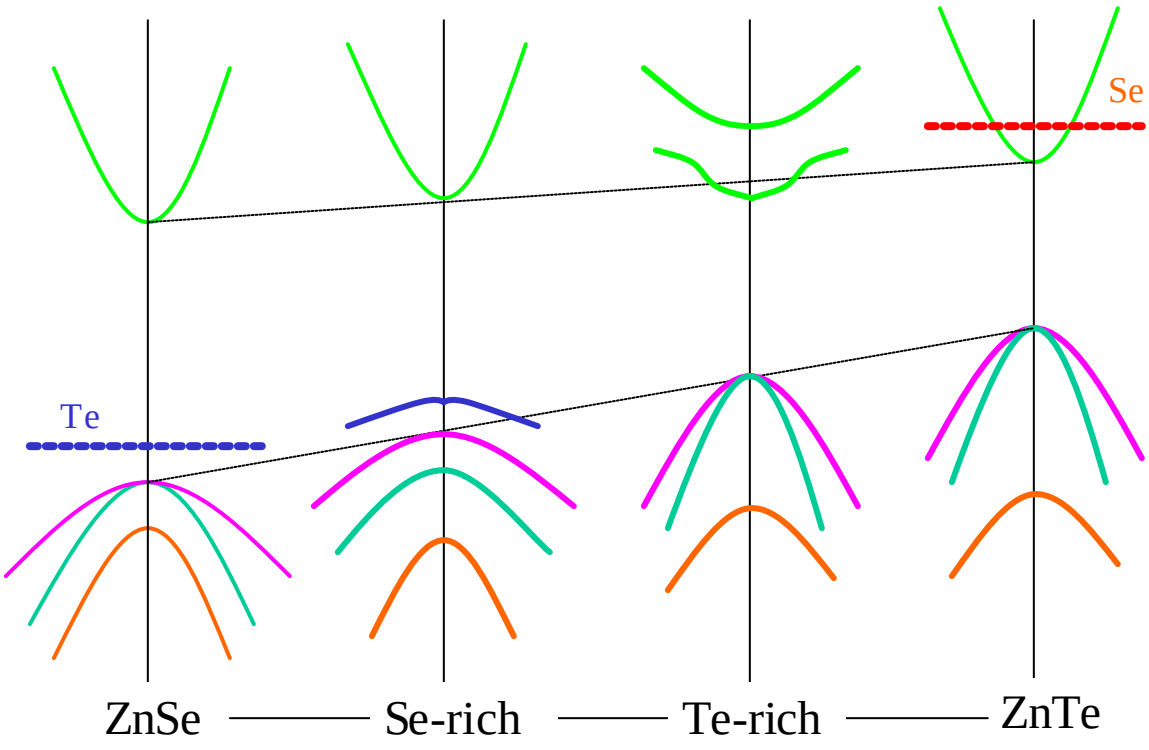


Fig.4.12 The schematic band diagram showing the band restructuring of ZnSeTe over the entire composition range.

In order to fit the experimental data over the entire composition range ($0 \le x \le 1$), we adopt a linear interpolation scheme, similar in spirit to the original VCA interpolation, between these two effects, *i.e.*, the conduction band anticrossing (CBAC) on the Te-rich side and the valence band anticrossing (VBAC) on the Se-rich side. For the composition dependence of the fundamental bandgap, it is written as

$$E_g(x) = (1-x)\cdot E_g^{Se-rich}(x) + x \cdot E_g^{Te-rich}(x). \tag{4.6}$$

This linear interpolation weighs the importance of these two effects by the concentration of the majority component from each side. In the calculation, the band offset values between ZnTe and ZnSe are adopted from the literature and are shown in Fig. 4.13.

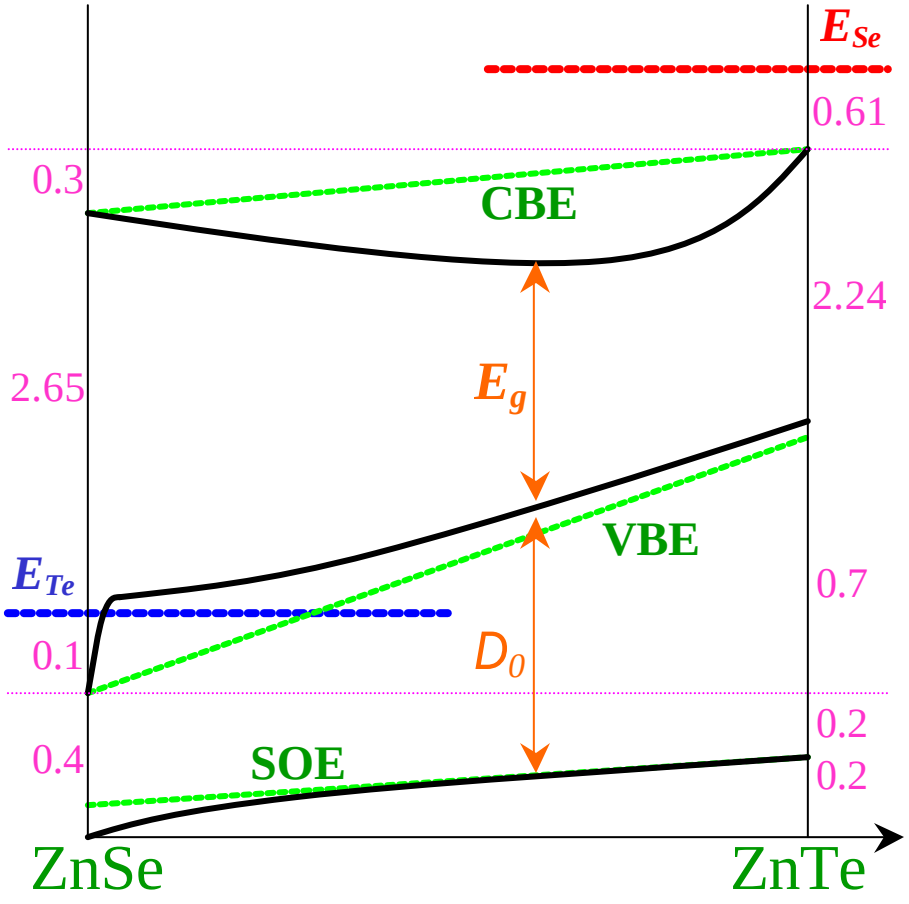


Fig. 4.13 The band offsets used in the calculation [93].

The calculated bandgap and the spin-orbit splitting are compared in Fig. 4.11 with the experimental results. The best agreement with the experimental data gives a coupling parameter $C_{ZnSe-Te}$ =0.30 eV and the Te localized level at 0.10 eV above the top of the original ZnSe valence band. This energy location is close to the value reported in ref. [98].

It is worthwhile to note the unusual composition dependence of the PR linewidth of the $E_g$ transition shown in the inset of Fig. 4.11. An abrupt broadening of the linewidth is observed on the Se-rich side. This composition dependence of the PR linewidth is quite similar to the behavior of the previously reported PL linewidth in $ZnSe_{1-x}Te_x$ alloys [97]. The asymmetry in the PR line broadening behavior is associated with a change in the nature of the band edge states. As indicated by Eq. (3.28) in the Green's function calculations [38], the energy broadening of an eigen-state in the localized-extended hybridization system is proportional to the admixture of the localized states in its wavefunction. The curve in the inset is a fit to the linewidth data based on the percentage of localized states in the wavefunction of $E_{Te\text{-}like}$. The large linewidth for small $x$ values is associated with the localized nature of the Te-like states at the top of the valence band. For $x$ close to 1, the delocalized nature of both the conduction and the valence band edges results in a narrow linewidth for the PR spectra.

The valence anticrossing interaction does not only shift the band edges in the Brillouin zone center, but also affects the dispersion relations of the valence bands. Calculations show that the restructured valence bands become largely non-parabolic, as in the case of the conduction band anticrossing in III-V-N alloys. The dispersion relations for $x$=0.1 is compared with that of pure ZnSe in Fig. 4.14. The hole effective mass at the

top of the valence bands is enhanced from that of pure ZnSe. The enhancement of the hole effective mass as a result of the valence band restructuring may also have advantageous effects in hole-mediated ferromagnetic semiconductors [100].

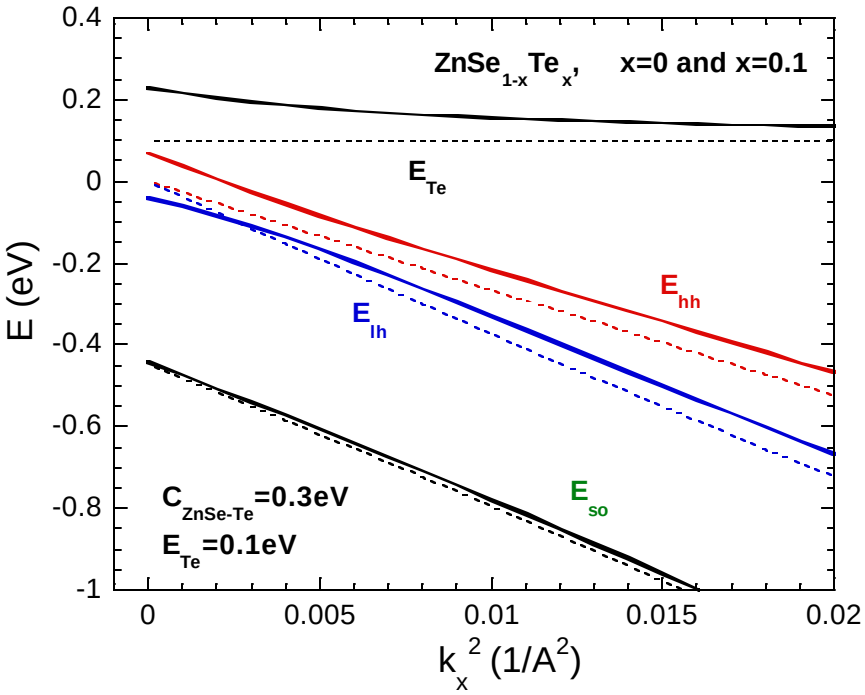


Fig. 4.14 Dispersion relations for pure ZnSe (dashed lines) and $ZnSe_{0.9}Te_{0.1}$ (solid lines) in (100) direction. Note that the horizontal axis is scaled in $k_x^2$.

### 4.2.3. Soft x-ray Fluorescence Studies of ZnSTe

It is important to note that according to the BAC model, the main contribution to the bandgap bowing originates from the downward shift of the conduction band edge on the Te-rich side and an upward shift of the valence band on the Se-rich side. In order to obtain an independent confirmation for this assertion, one needs to determine the conduction and the valence band offsets as a function of composition. In this context, we

have used soft x-ray emission (SXE) spectroscopy to measure the valence band shift in $ZnS_{1-x}Te_x$. A large shift of the valence band is expected in this alloy system, as it has been known for a long time that the localized Te level is separated by as much as 1.2 eV from the VBE of ZnS [101].

Figure 4.15 shows a typical SXE spectrum of a $ZnS_{1-x}Te_x$ film excited at S-2p level. The SXE and absorption spectra near the energy gap for a range of Te fraction are shown in Fig. 4.16(a). In this experiment, the excitation x-ray energy was first scanned across the S-2p core levels, and the partial fluorescence yield was recorded as the x-ray absorption spectrum. The threshold energies of the excitation determine the energy of the conduction band minimum with respect to the core level for a number of compositions. They are shown on the right part of the curves in Fig. 4.16(a). The doublet structure due to the S-$2p_{3/2}$ and S-$2p_{1/2}$ splitting (~ 1.6 eV) [102] is clearly resolved for Te-rich samples. The excitation energy was then tuned to the edge of the conduction band so that only the S-$2p_{3/2}$ core level was ionized. The x-ray emission due to electronic transitions from the upper valence band region to this core level was monitored with an energy-dispersive detector. The emission spectra are shown in Fig. 4.16(a) as the left part of the SXE curves. In this way the relative shifts of the conduction band minimum (schematically shown by the dashed arrow in Fig. 4.16(a)) and the valence band maximum (solid arrow in Fig. 4.16(a)) as a function of composition are directly measured. The results are summarized in Fig. 4.16(b). It is evident that, in agreement with the VBAC model, the top of the valence band exhibits a strong non-linear composition dependence on the S-rich side. This upward shift is caused by the transition

in the nature of the highest VBE from that of extended states of pure ZnS to localized Te-like states, hybridized with the extended valence band states of the ZnS matrix.

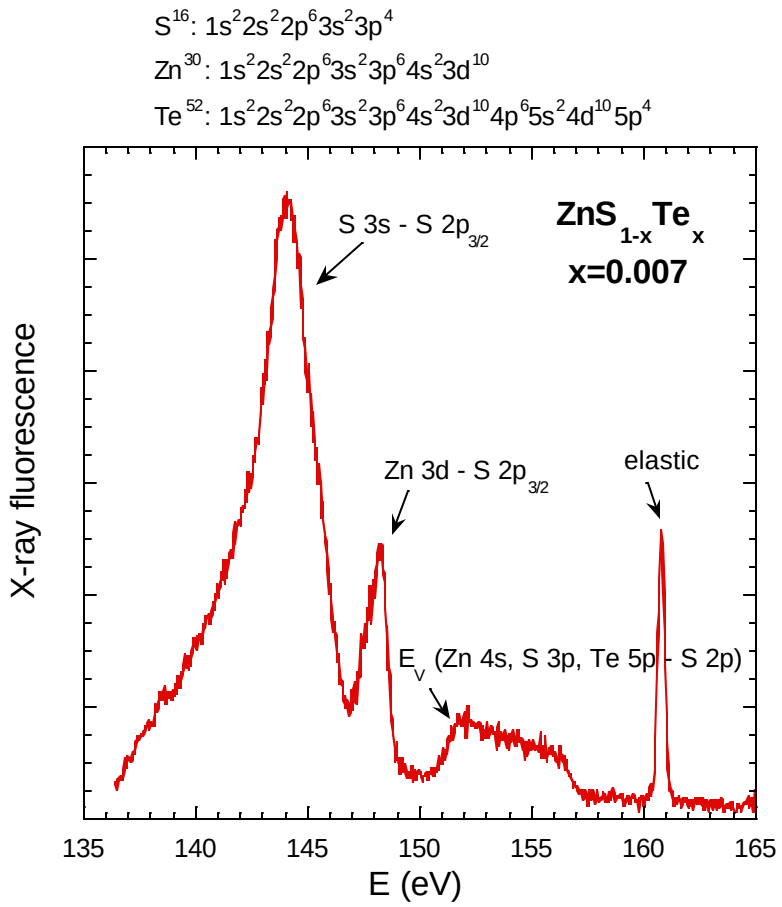


Fig. 4.15 Typical soft x-ray emission spectrum of ZnSTe alloys excited at the threshold of the S-2p level.

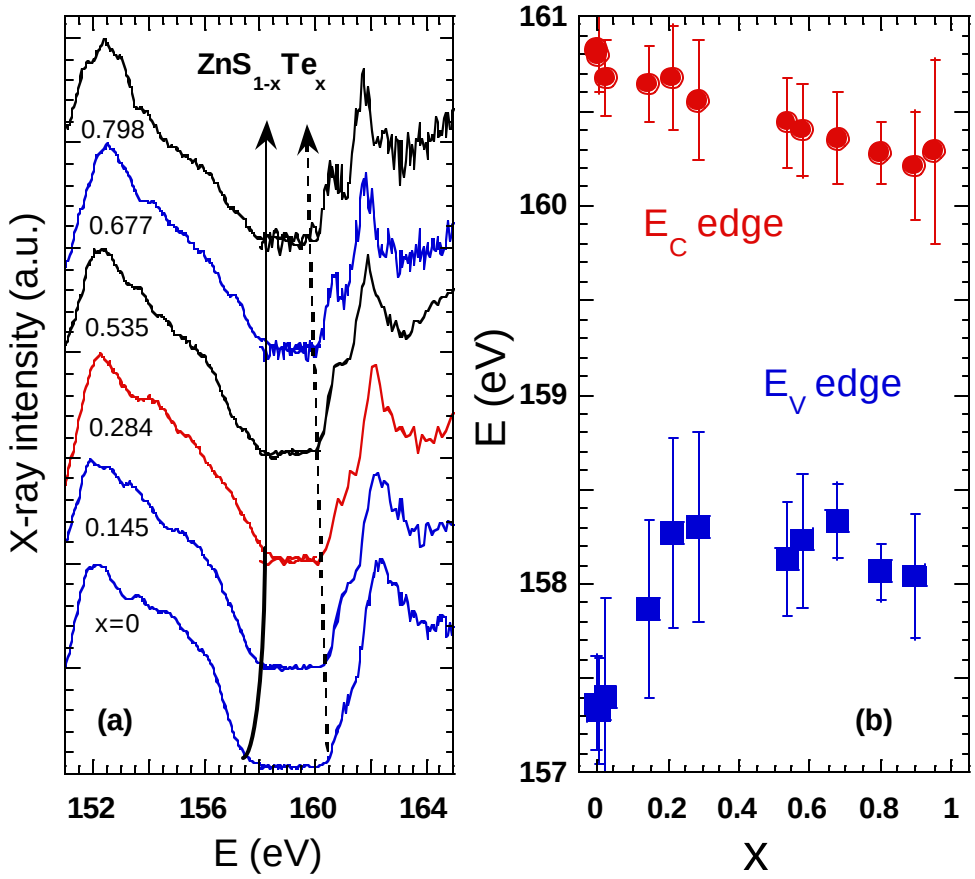


Fig. 4.16 (a) Soft x-ray emission and absorption spectra for a range of Te concentration. (b) The conduction and valence band edges as determined in (a) plotted as a function of Te concentration.

Figure 4.17 summarizes the transition energies measured by different techniques over the entire composition range of the $ZnS_{1-x}Te_x$ alloy. The data points from PR and absorption experiments that measure the large density of extended states show a strong bandgap bowing. On the other hand, the PL peak is shifted to lower energies as it is associated with optical transitions to deep states. The energy gap measured by SXE in Fig. 4.16 is also plotted in Fig. 4.17. Within experimental error, these gap energies agree

with the bandgaps measured by absorption and PR. This agreement confirms that the band edges measured by SXE in Fig. 4.16 are indeed the ones involved in the inter-band transitions observed in absorption and PR experiments.

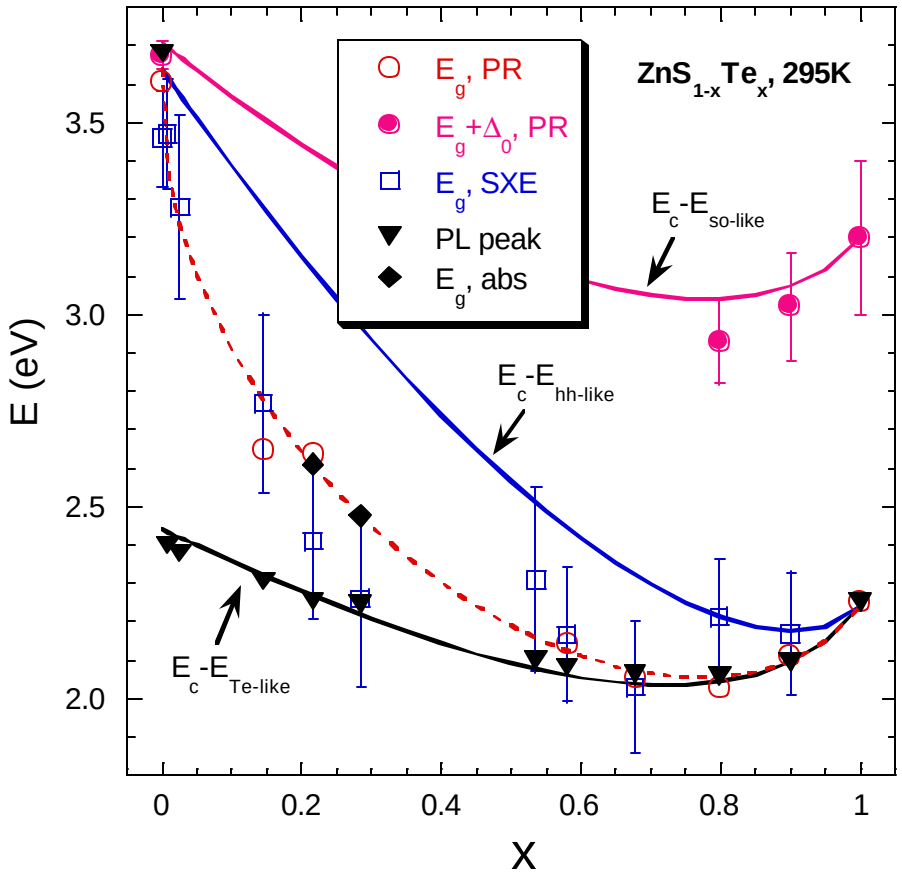


Fig. 4.17 PL peak energy and bandgap measured by SXE, PR and absorption experiments (abs) plotted as a function of $x$. The solid lines show the calculated energy difference between $E_c$ and $E_{Te\text{-}like}$, $E_{hh\text{-}like}$, and $E_{so\text{-}like}$, respectively. The dashed line is an empirical interpolation between $E_c$ - $E_{Te\text{-}like}$ and $E_c$ - $E_{hh\text{-}like}$ fitted to the composition dependence of the measured bandgaps.

Calculations based on the CBAC and VBAC models applied to $ZnS_{1-x}Te_x$ are shown as curves in Fig. 4.17. On the Te-rich side, as shown in Ref.[20], an anticrossing interaction between the ZnTe conduction band minimum and the S level located at ~ 0.36 eV above the minimum was assumed. A valence band anticrossing on the S-rich side was calculated and an interpolation as expressed in Eq.(4.6) was carried out over the complete composition range. The best fit is obtained by setting the Te level at 1.2 eV above the valence band maximum of ZnS and a coupling constant of $C_{ZnS-Te}$ = 0.5 eV. It can be seen that the PL peak energy agrees well with the calculated transition energy from the conduction band minimum to the highest, Te-like VBE. The dashed line in Fig. 4.17 is an empirically weighted interpolation between the calculated $E_c$ - $E_{Te\text{-}like}$ and $E_c$ - $E_{hh\text{-}like}$. The measured bandgap of $ZnS_{1-x}Te_x$ deviates from $E_c$ - $E_{hh\text{-}like}$ as a result of the hybridization. But unlike in $ZnSe_{1-x}Te_x$, it does not immediately follow $E_c$ - $E_{Te\text{-}like}$ because of the much larger energy separation between the Te level and the valence band maximum of ZnS. Consequently, the fraction of extended states at the top of the restructured valence band (*i.e.*, $E_{Te\text{-}like}$) is too small to contribute to the absorption or PR transitions. Such transitions are observable only when the anticrossing interaction becomes strong enough at relatively high Te concentrations.

### 4.2.4. Hydrostatic Pressure Coefficients

As has been shown in Fig. 3.8 for Te-rich $ZnSe_{1-x}Te_x$ alloys [20], alloying of ZnSe with ZnTe results in a large reduction in the hydrostatic pressure dependence of the bandgap. This pressure behavior has also been fully accounted for by the anticrossing interaction between the localized Se state, which is insensitive to pressure, and the extended states of the ZnTe conduction band, which rapidly shifts upwards with pressure.

To understand more about the electronic structure of $ZnSe_{1-x}Te_x$, we have measured the optical absorption edge at different pressures for the alloys over the entire composition range. Typical absorption curves are shown in the inset of Fig. 4.18. The energy gap as a function of pressure is extracted from the absorption curves. Representative pressure dependencies of the bandgap for the Te- and Se-rich alloys are shown in Fig. 4.18. Unlike in the Te-rich alloys, alloying with the minority component on the Se-rich side does not change the pressure dependence considerably from that of the majority component. This phenomenon can be understood by the fact that the largest contribution to the blue-shift of bandgap under pressure comes from the upward shift of the CBE with pressure. Because the conduction band is not perturbed on the Se-rich side except for the weak, linear VCA effect, the pressure coefficient is not significantly affected.

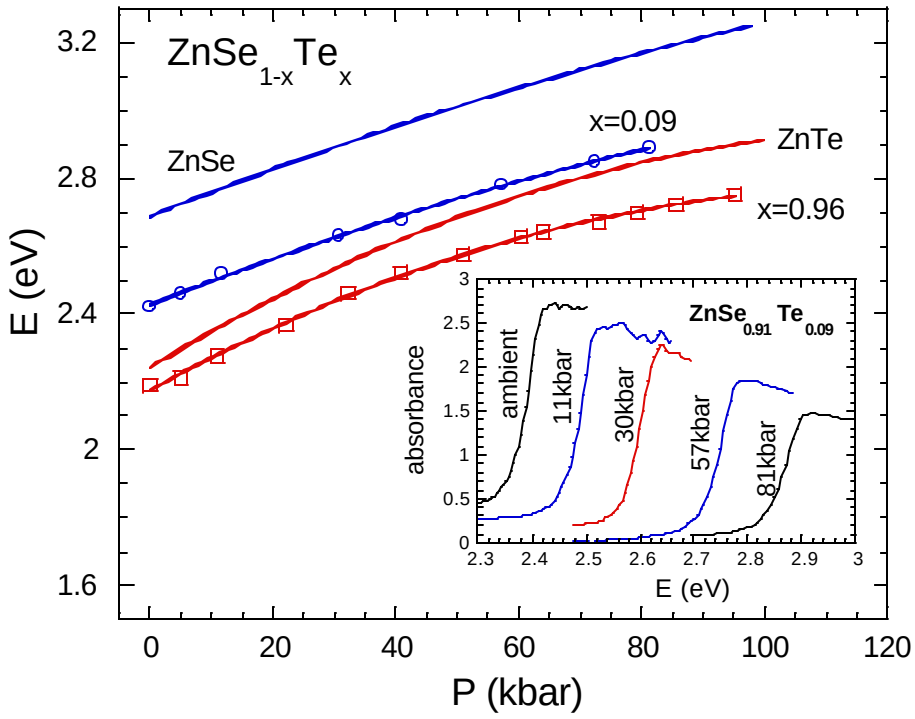


Fig. 4.18 Pressure dependence of the fundamental bandgap determined from optical absorption measurements. The solid curves are quadratic fits to the experimental data. Inset, absorption curve of a 10 μm-thick $ZnSe_{0.91}Te_{0.09}$ sample evolving with pressure. All the data were taken at room temperature.

The linear ($a_1$) and second-order ($a_2$) pressure coefficients are defined as,

$$a_1(x) \equiv \left.\frac{\partial E_g(x,P)}{\partial P}\right|_{P=0} ; \; a_2(x) \equiv \frac{1}{2}\cdot\left.\frac{\partial^2 E_g(x,P)}{\partial P^2}\right|_{P=0} . \qquad (4.7)$$

In Fig. 4.19, they are shown as a function of the Te concentration. The curves are the calculated results following a similar interpolation scheme as expressed in Eq.(4.6). In the pressure coefficients interpolation, the term to be weighted on the Se-rich side is fixed at the pressure coefficients of ZnSe. On the Te-rich side, the CBAC-calculated CBE is

expanded in Taylor series in terms of pressure, and the linear and second-order coefficients are extracted and numerically calculated. A linear pressure coefficient of $1.5\times10^{-3}$ eV/kbar is assumed for the Se localized level in the calculations [20]. For the ZnTe conduction band, $a_1$=10.9×10$^{-3}$ eV/kbar and $a_2$=-4.25×10$^{-5}$ eV/kbar$^2$ are used as determined by previous experiments [20]. As can be seen from Fig. 4.19, this simple interpolation predicts the linear pressure coefficient quite well. The second-order coefficient deviates from this simple interpolation, especially on the Te-rich side. This is mostly due to the fact that the pressure dependence of the bandgap predicted by the CBAC model contains considerable higher-order coefficients beyond the linear and quadratic dependencies [20].

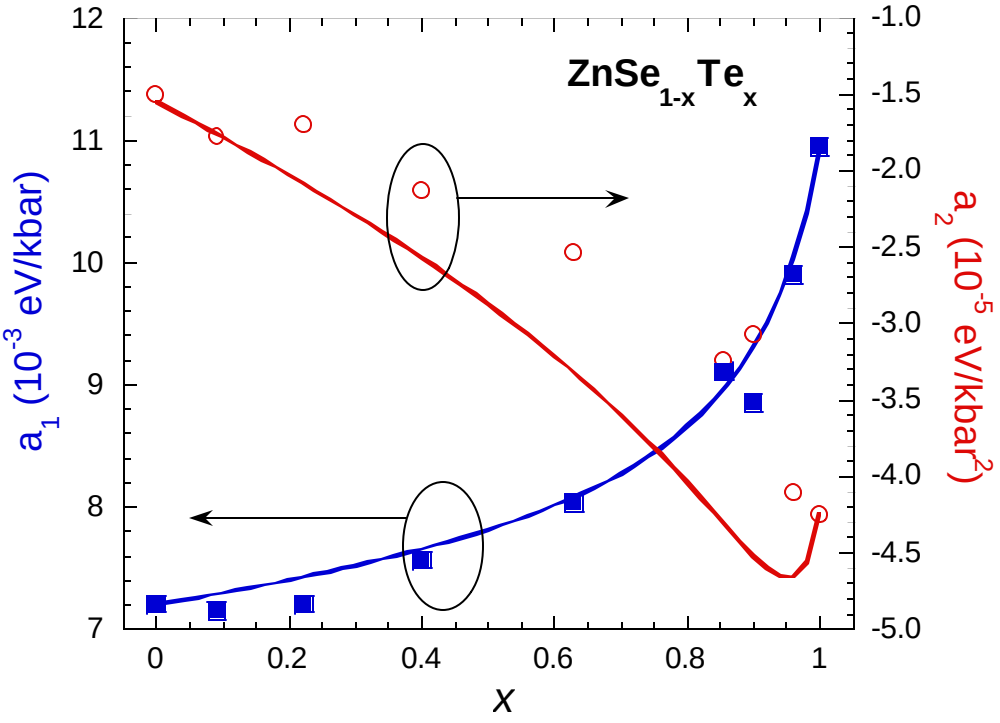


Fig. 4.19 Linear and second-order pressure coefficients as a function of Te concentration. The curves show the calculated dependencies of the coefficients.

The calculations and their comparison with experimental results support the fundamentally different origins of the bandgap bowing in Se (or S) -rich and Te-rich $ZnSe_{1-x}Te_x$ (or $ZnS_{1-x}Te_x$). The results are important for the understanding of the doping behavior of these alloys as well. As has been shown recently [37], the N-induced modification of the conduction band structure of GaAs greatly increases the upper limit of the free electron concentration in $GaAs_{1-x}N_x$ alloys. In view of the findings in these II-VI alloys, we also expect that the downward shift of the conduction band edge in Te-rich, and the upward shift in Se (or S) -rich alloys, should lead to improvements in the activation efficiency of donors in the former, and acceptors in the latter. These predictions are indeed in agreement with recent experimental observations, which have shown that alloying of ZnSe with small amounts of ZnTe greatly improves the activation efficiency of nitrogen acceptors [103].

# 5. Summary of the Band Anticrossing Effect in Highly Mismatched Semiconductor Alloys

The band anticrossing model successfully explains the strong bandgap bowing of all highly electronegativity-mismatched semiconductor alloys. Chapter 3 and 4 present the theoretical origin and resultant effects of band anticrossing between localized impurity states and the extended band states of the host in these HMAs. Some important experimental results have been discussed in the context of the band anticrossing model. The band anticrossing interaction does not only exist between the localized states and the conduction band near the Brillouin zone center, but also extends to states at the Brillouin zone edge. As examples for the generality of the application of the band anticrossing model, it has been shown in section 3.4.2 that the large bowing parameters observed in group III-Sb alloys with As or P substituting the Sb can also be explained by the interaction between localized As or P levels and the extended conduction band states of the semiconductor matrix.

Valence band anticrossing has been demonstrated in Se-rich ZnSeTe and S-rich ZnSTe alloys. The interaction between the localized states of the minority component and the degenerate valence bands of the host has been formulated in a $\boldsymbol{k}\cdot\boldsymbol{p}$ matrix form. The eigen-energies have been calculated and compared with experimental results. The valence band anticrossing effect is further confirmed by the direct measurements of the band edge energies in soft x-ray emission experiments. The bandgap bowing effect over the complete composition range is interpreted by a linear interpolation between the conduction band anticrossing and the valence band anticrossing. Similar to the

conduction band anticrossing, valence band anticrossing also occurs in both group II-VI and III-V alloys. Shown in Fig. 5.1 is the band gap and spin-orbit splitting of $GaAs_{1-x}Sb_x$ as a function of $x$ measured by photomodulated reflectance. The bowing effect can be well explained by an anticrossing interaction between the valence bands of GaAs and the Sb level lying at 1 eV below the top of the valence band with an interaction parameter of $C_{GaAs-Sb}$=0.6 eV. Unlike in ZnSeTe and ZnSTe, the bowing in $GaAs_{1-x}Sb_x$ shown in Fig. 5.1 is relatively small. This is attributed to the fact that the Sb localized level lies below the valence band edge in resonance with the valence bands.

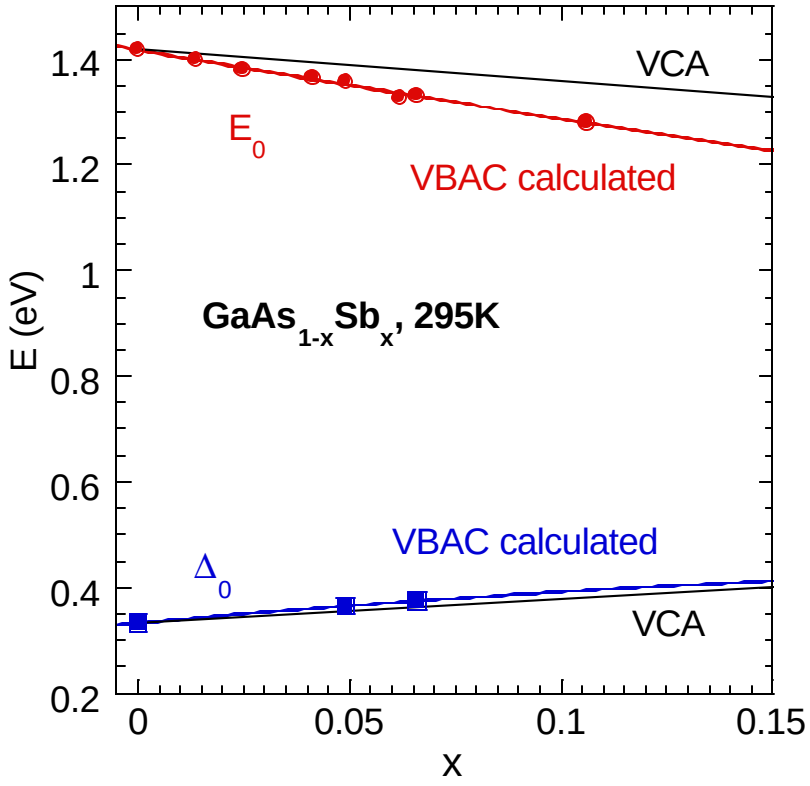


Fig. 5.1 The composition dependence of the band gap and spin-orbit splitting in As-rich GaAsSb.

Experimentally, it has been observed that in anion alloys the larger the electronegativity difference between the anion elements is, the stronger is the bandgap bowing. This implies a direct influence of the electronegativity on the BAC coupling parameter in these alloys. This is not unexpected, though, because when the host atom is substituted by an isovalent impurity atom with larger electronegativity, a stronger local potential is formed in the space surrounding the atom site. In Fig. 5.2 the relationship in conduction band anticrossing is summarized for all the alloys discussed in this thesis. It can be seen that the coupling parameter is practically proportional to the electronegativity difference.

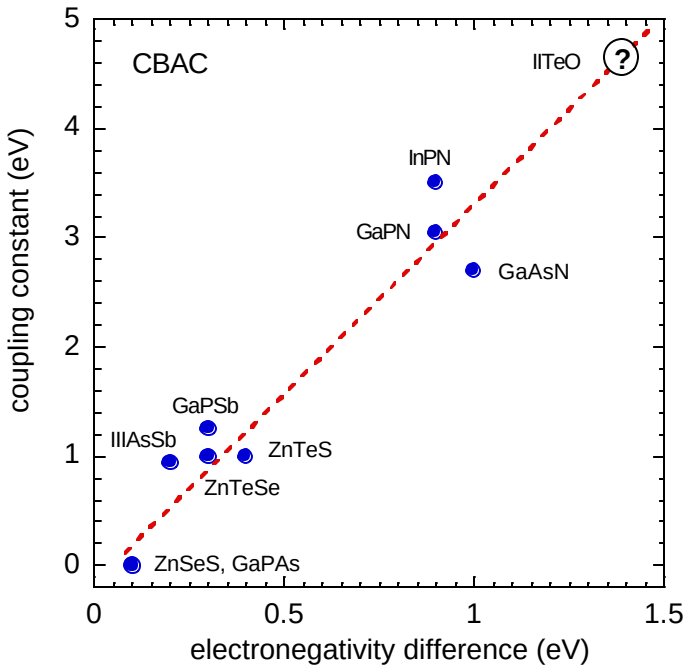


Fig. 5.2 The coupling constant of the conduction band anticrossing in II-VI and III-V anion alloys plotted as a function of the electronegativity difference of anion elements. For II-Te-O alloys the value of the coupling parameter has not yet been experimentally determined due to the lack of information about the oxygen concentration that is electrically active in our samples.

# 6. Additional Studies of InN and Related Alloys

## 6.1 Studies of the fundamental bandgap of InN

In previous chapters, strong bandgap bowing has been demonstrated to occur in highly mismatched semiconductor alloys as a result of anticrossing interaction between localized states and extended states. There is another situation in which large bandgap bowing exists due to large differences between the bandgaps of end-points materials. Group III-nitride alloys belong to such a system. Group III-nitrides have become a widely studied class of semiconductor materials. Both GaN and $In_xGa_{1-x}N$ with small $x$ are very efficient light emitters, even in samples with relatively high densities of structural defects, and are used as component layers in a wide range of opto-electronic devices [1]. In contrast, InN has been observed to date to be a very poor light emitter. Early studies of the interband optical absorption performed on InN thin films deposited by sputtering techniques [2,3] and metalorganic vapor phase epitaxy [4] were interpreted as being consistent with a fundamental energy gap of about 2 eV. The electron concentration in those films was usually over $10^{20}$ $cm^{-3}$ and the room-temperature mobility was below 100 $cm^2/Vs$. This value of the bandgap has been widely accepted and frequently used as the end point value for the extrapolation of the bandgap in $In_xGa_{1-x}N$ alloys [5]. It should be emphasized that despite extensive efforts, no light emission associated with the energy gap near 2 eV has ever been reported in these early studies of InN. Only most recently, very weak photoluminescence peaks with energies ranging from 1.81 eV to 2.16 eV were observed on InN grown on Si substrates [6].

Recent improvements in epitaxial growth techniques have led to the availability of InN films with considerably lower electron concentrations and much higher electron mobilities. Electron concentrations in mid $10^{18}$ $cm^{-3}$ with room temperature electron mobilities well in excess of 1000 $cm^2/Vs$ were achieved by these methods [7-9]. It has been reported most recently that these improved InN films show a strong photoluminescence at energies around 1 eV [9]. Since it has been also found that the position of the photoluminescence energy correlates with an onset of strong absorption, it has been argued that the optical transition at about 1 eV corresponds to the fundamental bandgap of InN [9].

Interestingly, a number of first-principles theoretical calculations predict an energy gap for InN much smaller than 2 eV. As expected, the calculations based on the local density approximation (LDA) severely underestimate the energy gap; these calculations predict that InN is metallic with a negative energy gap of -0.4 eV [10]. A recently developed self-interaction and relaxation-corrected pseudopotential approach predicts a larger gap (1.55 eV); this is still significantly smaller than 2 eV [11]. These low values of theoretical energy gaps cannot be entirely attributed to the limitations of the LDA. Indeed, a quasi-particle corrected LDA calculation that gives accurate values of the energy gaps in GaN and AlN predicts a gap of only 1.39 eV in wurtzite InN [12].

In this section, results of comprehensive studies of the optical and electrical properties of InN samples grown in two laboratories are summarized. Our optical absorption, photomodulated reflection, and hydrostatic pressure and temperature dependent photoluminescence results are consistent with an intrinsic fundamental

bandgap of InN of about 0.8 eV. We have also found that the low energy gap exhibits unusual temperature and pressure dependencies.

InN films were grown on (0001) sapphire with an AlN buffer layer by molecular-beam epitaxy [13]. The thickness of the buffer layer ranges from 70 nm to 200 nm. The InN layer thickness is between 120 nm and 1000 nm. The details of the growth process have been published elsewhere [13]. X-ray diffraction studies have shown that high-quality wurtzite-structured InN epitaxial layers form with their c-axis perpendicular to the substrate surface. To confirm the experimental results we have obtained from this series of samples, we have also measured the photoluminescence signal from an InN sample grown in another laboratory by radio-frequency plasma-excited molecular-beam epitaxy [14]. This particular sample will be referred as the Ritsumeikan sample in the text following.

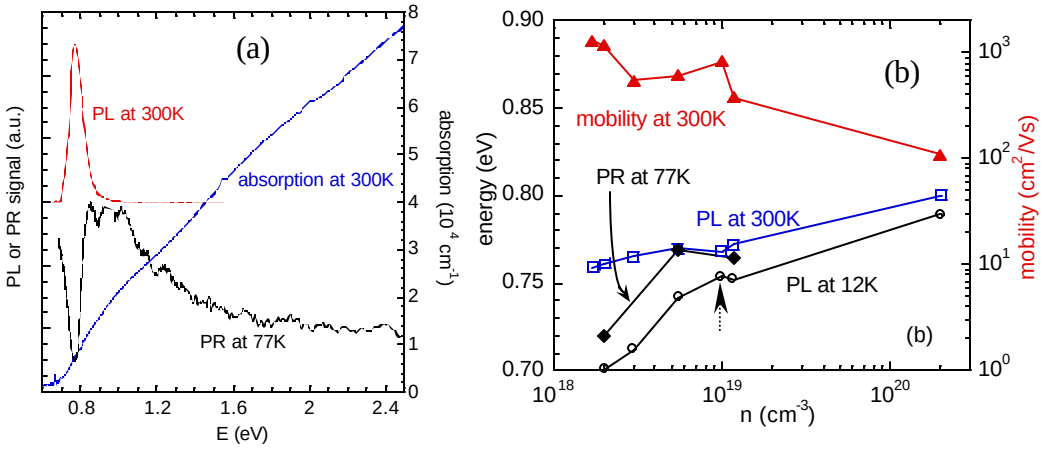


Fig. 6.1 (a) Optical absorption, PL, and PR spectra of a typical InN sample. (b) Mobility, PL peak energy, and the critical energy determined by PR (77 K) as a function of free electron concentration. The sample with $n$=1×$10^{19}$$cm^{-3}$ (indicated by a broken arrow) is the Ritsumeikan sample.

Figure 6.1 (a) shows the optical characteristics of a typical InN sample. The free electron concentration in this sample was measured by Hall Effect to be $5\times10^{18}$ $cm^{-3}$. The optical absorption curve shows an onset at ~0.78 eV. The absorption coefficient increases gradually with increasing photon energy and reaches a value of more than $10^4$ $cm^{-1}$ at the photon energy of 1 eV. This high value of the absorption coefficient is typical for an interband absorption in direct-gap semiconductors [15]. It is important to emphasize that there is no noticeable change in the absorption in the 1.9 to 2.0 eV region, *i. e.*, in the energy range of previously reported bandgaps in InN [3-5].

Also, as shown in Fig. 6.1 (a), the samples exhibit intense room temperature luminescence at energies close to the optical absorption edge. Finally, the 77 K PR spectrum exhibits a transition feature at 0.8 eV with a shape that is characteristic of direct gap interband transitions. As with the absorption spectrum, there is no discernible change in the PR signal near 2 eV. The simultaneous observations of the absorption edge and PL and PR features at essentially the same energy indicate that this energy position corresponds to the transition across the fundamental bandgap of InN.

Fig. 6.1 (b) shows the room-temperature electron mobility, the peak energy of PL and the transition energy determined by PR as functions of electron concentration. The sample with the highest free electron concentration $n = 2\times10^{20}cm^{-3}$ is silicon-doped. All the other samples are not intentionally doped. The samples with the lowest electron concentrations have mobilities $m$ greater than 1000 $cm^2/Vs$. It is seen in Fig. 6.1 (b) that the transition energies increase with increasing free electron concentration. This indicates that the transitions from higher-energy occupied states in the conduction band contribute significantly to the PL spectrum.

The temperature dependence of the PL peak energy can be seen in Fig.6.1 (b). The PL peak energy decreases from 300 K to 12 K. The shift is smaller for samples with higher free electron concentration, ranging from 0.03 to 0.2 meV/K for the samples investigated. This behavior is in a stark contrast to the temperature dependence of the direct bandgap in most semiconductors, where typically a significant reduction of the bandgap is observed with increasing temperature [16].

More detailed studies of the temperature dependence of the PL were carried out on the sample with $n$=5.48×$10^{18}$ $cm^{-3}$ and $m$=615 $cm^2$/Vs. The results are shown in Fig. 6.2 (a) and Fig. 6.2 (b). As can be seen in Fig. 6.2 (b), in addition to the small blueshift (nearly linear at ~ 0.1meV/K) in the peak energy of the PL, the integrated intensity of the PL decreases by ~ 20 times as the temperature is increased from 11 K to room temperature. The data in Fig. 6.2 (a) also show a considerable increase of the linewidth of the PL spectra. The FWHM increases from 35 meV to 70 meV when the temperature increases from 11 K to room temperature. It can be therefore concluded that there is no significant shift of the PL spectra, as the temperature induced line broadening can easily account for the observed small upward shift of the PL line maximum.

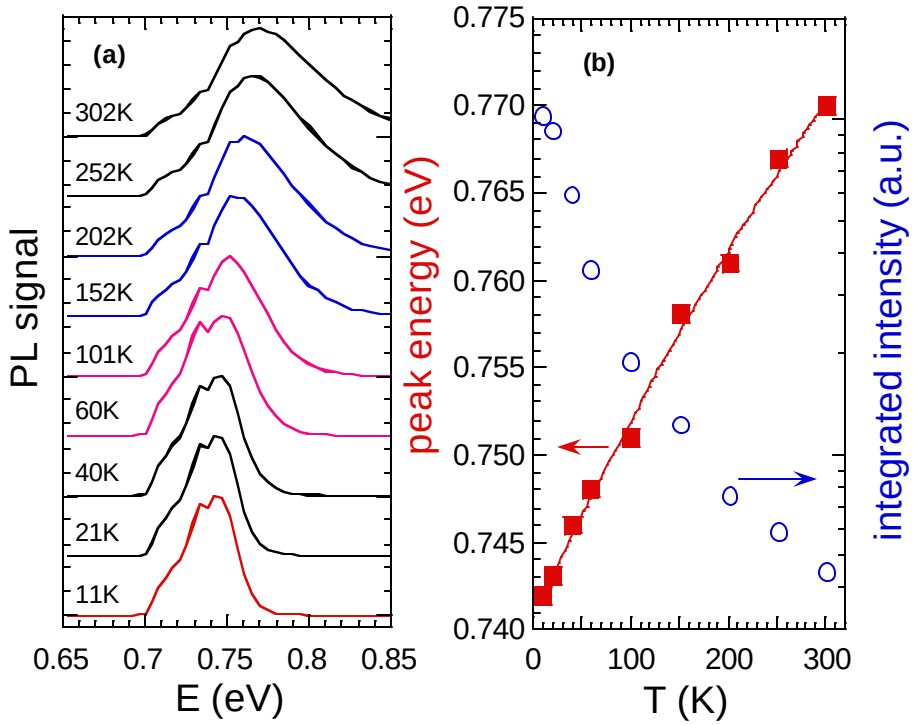


Fig. 6.2 (a) PL spectra as a function of temperature for the sample shown in Fig. 6.1 (a). The PL spectra are normalized to a constant peak height. (b) The PL peak energy and the PL integrated intensity (log scale) as a function of temperature. The line through the peak energy data is a guide for the eye.

We have also measured the excitation power dependence of the PL. As shown in Fig. 6.3 (a), the integrated PL intensity depends linearly on the excitation power over three orders of magnitude. The peak energy does not shift over this excitation energy range. The simple linear dependence and the lack of any PL signal saturation effect again suggest that the PL originates from fundamental interband transitions in InN.

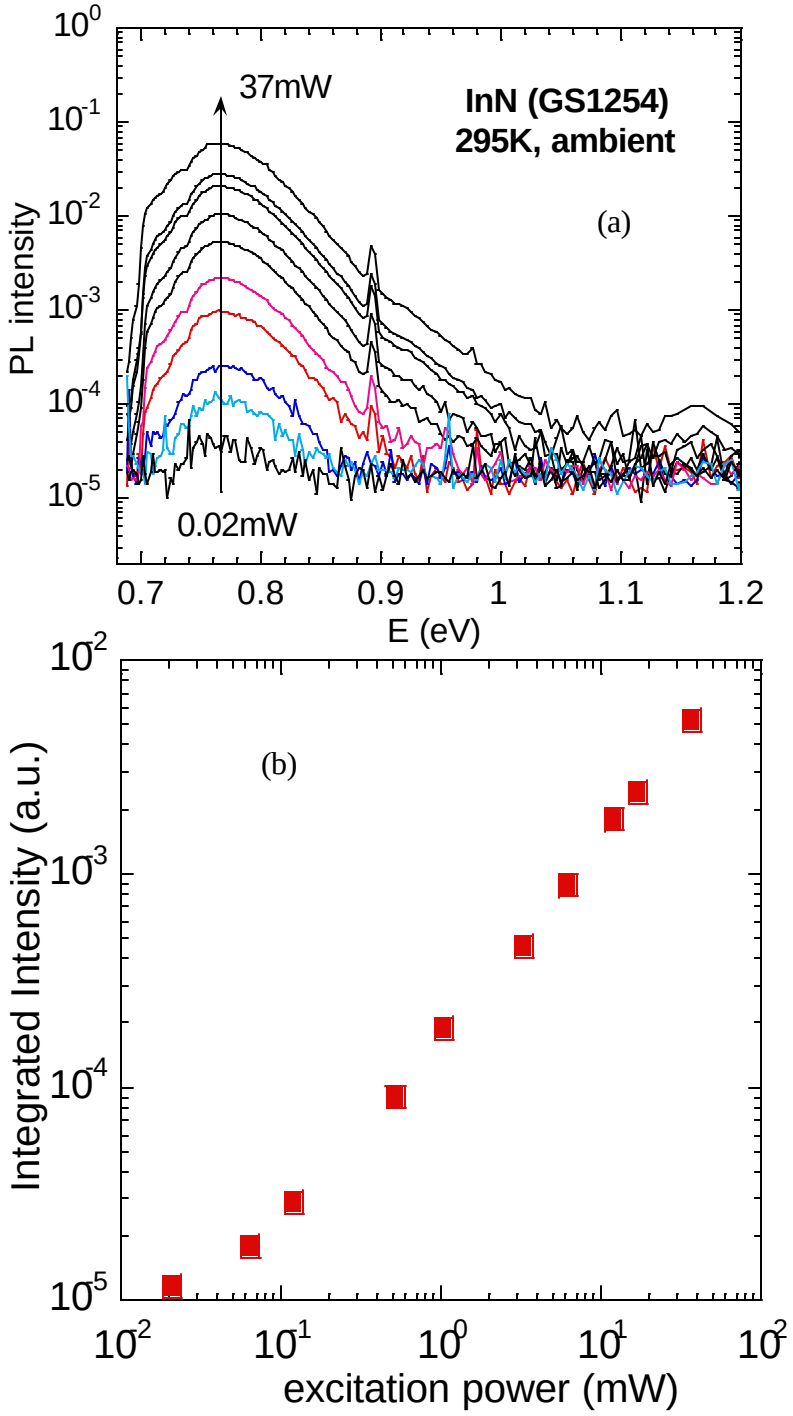


Fig. 6.3 (a) PL signals excited with different laser power. (b) The integrated PL intensity as a function of the excitation power.

To further elucidate the nature of the observed PL emission, we have studied its hydrostatic pressure behavior. The PL peak energy as a function of applied pressure is shown in Fig. 6.4 (b). The linear pressure coefficient is equal to 0.6 meV/kbar, which is considerably smaller than the pressure coefficient previously observed in other III-V compounds. For example, the pressure coefficient of GaN is 4.3 meV/kbar [17], of $Al_xGa_{1-x}N$ is 4.1 meV/kbar for $0.12 < x < 0.6$ [18], and for GaAs it is 11 meV/kbar [19]. We are aware that the presence of the sapphire, which has a larger bulk modulus than InN, will reduce the degree to which the hydrostatic pressure is transmitted to the InN film, if the film remains coherently strained to the substrate. Using experimental elastic constants for sapphire and theoretical elastic constants for InN, we estimated the correction factor for coherently strained InN on sapphire to be 1.45. Therefore, the pressure dependence of the PL peak energy is between 0.6 meV/kbar and 0.9 meV/kbar. This unusually low pressure coefficient of InN is not totally unexpected since, as it has been shown previously, the pressure dependence of the energy gap of $In_xGa_{1-x}N$ alloys decreases rapidly with increasing In content [17, 20].

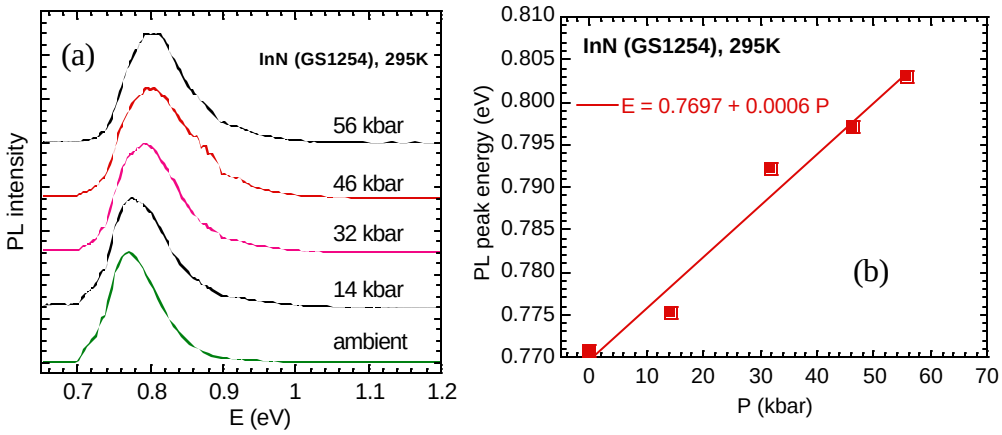


Fig. 6.4 (a) PL signal of an InN sample measured at different hydrostatic pressures. (b) The PL peak energy as a function of applied pressure.

The small pressure coefficient of the bandgap could, at least partially, explain the weak temperature dependence of the bandgap. The temperature coefficient of semiconductor bandgaps can be decomposed into two contributions, one from the change in the lattice constant due to thermal expansion, and the other one from the electron-phonon interaction [21]. The weak pressure dependence implies that there is only a very small contribution of the lattice expansion to the temperature induced bandgap change. Also, the small overall temperature coefficient further suggests that the electron-phonon coupling in this material may also be extraordinarily small.

It should be noted that in addition to the absorption edge at about 2 eV, early studies of the optical properties of InN have also reported an onset of strong absorption below 1 eV [3, 4, 22]. This absorption has been attributed to transitions from deep mid-gap defect or impurity levels to the conduction band [22]. Typical optical cross section for deep levels is of the order of $10^{-16}$ $cm^{-2}$ [23]. Therefore, in order to explain the

measured absorption coefficients of more than $10^4$ $cm^{-1}$ in our samples, it would require the presence of more than $10^{20}$ $cm^{-3}$ mid-gap defects or impurities. Even if this were the case, one should still be able to see the onset of the valence to the conduction band transitions around the bandgap of 2 eV. However, both optical absorption and PR spectra show no indication of any inter-band transition in this energy range in our samples, indicating that the previously observed 2 eV absorption edge is most likely not an intrinsic property of InN.

## 6.2 In-rich InGaN and InAlN Alloys

The $In_{1-x}Ga_xN$ alloy system has been studied extensively in recent years. An especially intensive effort has been directed towards studies of Ga-rich alloys which are used as the active layer in blue and green light-emitting diodes and lasers [24-27]. Another attribute of this alloy system is that its energy gap can be varied over a wide spectral range. For example, it has been shown that the bandgap can be decreased from the GaN value, 3.4 eV, down to ~2.3 eV for $In_{0.4}Ga_{0.6}N$ [28-31]. Studies of the optical properties of these Ga-rich alloys have shown a strong dependence of the fundamental bandgap on the alloy composition. When a bandgap of ~ 1.9 eV for InN is assumed as the end point value, large bowing parameters are required to fit the composition dependence of the fundamental bandgap energy. For example, a bowing parameter of 2.5 eV was obtained from optical absorption measurements and a value of 4.4 eV was obtained from the location of the emission peaks [28].

This section shows the systematic study of the optical properties of $In_{1-x}Ga_xN$ alloys on the In-rich side grown by molecular beam epitaxy. It was found that these alloys show a strong infrared PL signal, as expected for an InN bandgap of ~ 0.8 eV. The emission spectrum of the $In_{1-x}Ga_xN$ system thus extends to the near infrared. The bowing parameter over the entire composition range can be fitted with a small bowing parameter of ~ 1.4 eV.

The samples exhibit strong infrared PL signal even at room temperature. Figure 6.5(a) shows the PL signals for samples with a wide range of Ga compositions from 0 to 0.5. Both room temperature (295K) and low temperature (11K) results are shown. As

expected, the PL peak energy shows a strong blueshift from the bandgap of InN (0.77 eV at room temperature) with increasing Ga content. The linewidth of the PL peak is significantly broadened as *x* increases. The temperature also has an interesting effect on the PL signal, which will be discussed below.

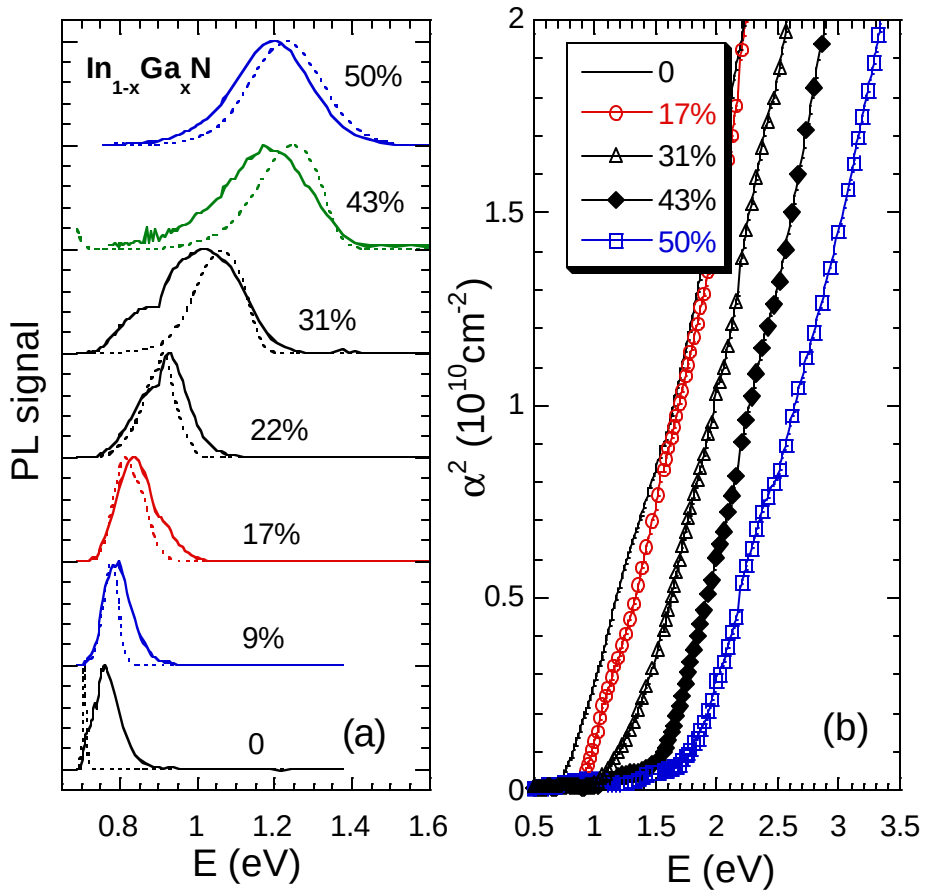


Fig. 6.5 (a) PL signals recorded at room temperature (solid line) and 11K (dashed line) for samples with the Ga atomic fraction *x* ranging from 0 to 50%. All curves are normalized to equal height and offset vertically for clarity. (b) Room-temperature absorption coefficient squared as a function of photon energy.

Figure 6.5(b) shows the absorption coefficient squared plotted as a function of the photon energy. In all cases, the absorption coefficient reaches ~ $10^5$ $cm^{-1}$ for a photon energy of ~ 0.5eV above the absorption edge, which is typical for direct bandgap semiconductors. The curves of the absorption coefficient squared are essentially linear in the range of the photon energy investigated, which again implies a direct fundamental bandgap. The observed slight non-linearity of the curves for small $x$ can be attributed to the non-parabolicity of the conduction band resulting from the $\boldsymbol{k}\cdot\boldsymbol{p}$ interaction between the $\Gamma_6$-symmetry conduction band and the $\Gamma_8$-symmetry valence bands [32].

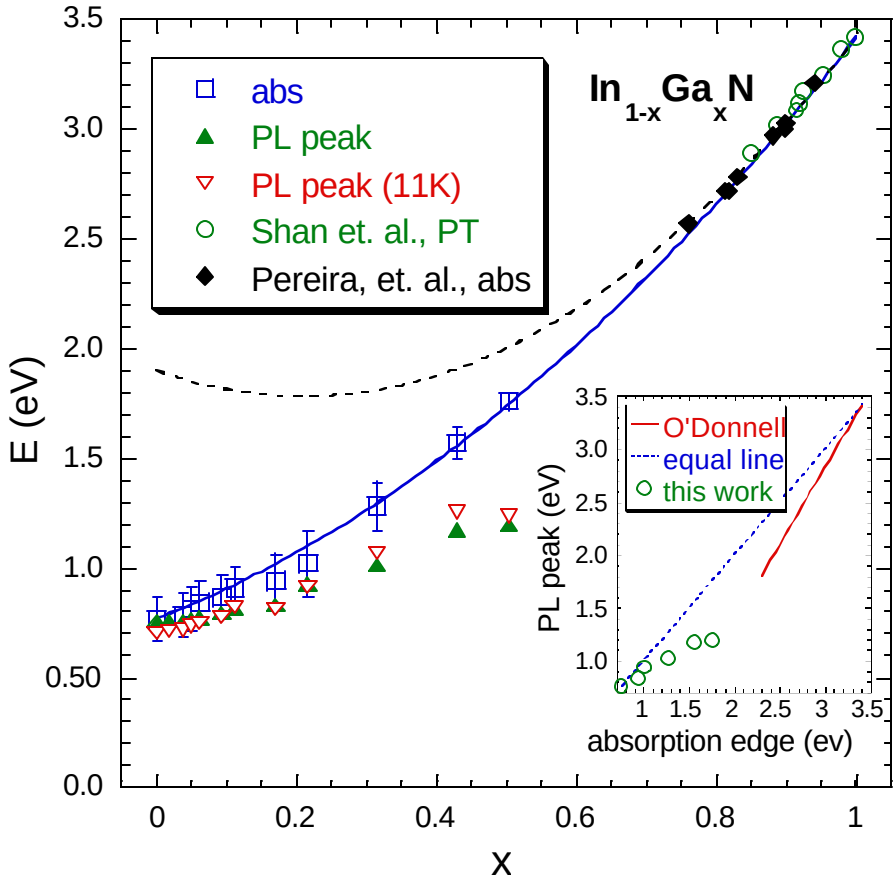


Fig. 6.6 PL peak energy and bandgap determined by optical absorption as a function of composition. Some previously reported data on the Ga-rich side are also shown. All data are taken at room temperature unless otherwise noted. The solid curve shows the fit to the bandgap energies (abs and PT) using a bowing parameter $b$ = 1.43 eV. The dashed curve is the fit to the bandgap energies on the Ga-rich side assuming a bandgap of 1.9 eV for InN. Inset: PL peak energy plotted against absorption edge energy. The solid line is a least-square fit to experimental data on the Ga-rich side adopted from O'Donnell, et. al. The dashed straight line shows the relation when the Stokes shift is zero.

The bandgaps determined from the absorption edges in Fig.6.5(b) are shown as a function of Ga concentration in Fig. 6.6. The absorption edge shifts rapidly to higher

energy as $x$ increases. Numerous studies have been performed on the composition dependence of the bandgap in Ga-rich $In_{1-x}Ga_xN$ alloys [28-31]. In order to see the composition dependence of the bandgap over the entire composition range, two sets of previously reported data on the Ga-rich side are also shown in Fig. 6.6. These bandgaps were measured by photomodulated transmission (PT) [30] and optical absorption [29], respectively. It can be seen that our data on the In-rich side makes a smooth transition to the data points on the Ga-rich side. This result further confirms that the absorption edge of InN observed near 0.77 eV indeed corresponds to the intrinsic fundamental bandgap of InN [9, 33]. As shown by the solid curve in Fig.6.6, the composition dependence of the room-temperature bandgap over the entire composition range can be well fitted by the following standard equation,

$$E_G(x) = 3.42\,x + 0.77\,(1-x) - 1.43\,x\,(1-x). \qquad (6.1)$$

with a constant bowing parameter of $b$ = 1.43 eV. This value of $b$ is much smaller than previously reported bowing coefficients for which a bandgap of ~ 1.9 eV for InN was used as the lower-energy end point [28,29], and is similar to that observed (1.4 eV) in the $Al_xGa_{1-x}N$ alloy system [18]. For example, if an InN bandgap of 1.9 eV instead of 0.77 eV is assumed, the two sets of data points on the Ga-rich side shown in Fig. 6.6 require a bowing coefficient as large as 2.63 eV to accommodate the composition dependence on the Ga-rich side. This fit is shown as a dashed curve in Fig.6.6. This artificially large bowing effect has also been discussed in terms of a composition dependent bowing parameter [20, 34]. It has been pointed out in Ref.[29] that the variety of experimental bandgaps on the Ga-rich side can be better fit with a pseudo-linear composition dependence. Our results show that this pseudo-linear composition dependence on the Ga-

rich side is simply a consequence of the small bowing over the entire composition range. An additional significance of Fig. 6.6 is that it demonstrates that the fundamental bandgap of this ternary alloy system covers a wide spectral region, ranging from near infrared at ~ 1.6 μm to near ultra-violet at ~ 0.36 μm.

The composition dependence of the peak energy of the PL signal is also shown in Fig. 6.6. At higher Ga concentrations, the PL peak energy shifts toward lower energy as compared to the absorption edge. The observed Stokes shift increases with increasing Ga content and is as large as 0.56 eV for $x = 0.5$. In the inset of Fig. 6.6, the PL peak energy is plotted as a function of absorption edge energy. Also shown by the solid line is a linear fit to experimental data on the Ga-rich side [31]. The deviation from the linear interpolation (dashed line) represents the Stokes shift. It is clearly seen that the Stokes shift tends to reach the maximum near the middle of the composition. This suggests the inhomogeneous distribution of In and Ga atoms as the origin of the shift. The large composition-dependent Stokes shift indicates that PL measurements are not reliable to determine the bowing parameter. It also explains the origin of the much large bowing parameter of 2.5 eV determined in recent PL studies of $In_{1-x}Ga_xN$ alloys [35].

The emission spectrum measured by PL spectroscopy reflects the distribution of localized states in smaller-gap regions that have larger-than-average In compositions [34, 36], while the absorption transition mainly reflects the onset of the density of delocalized states. Therefore, the fact that the Stokes shift reaches its maximum around the middle of the composition range implies that the largest degree of composition fluctuation and/or structural disorder occurs near the middle. This is also consistent with the result that the linewidth of the PL signal increases with increasing Ga concentration, as is seen in Fig.

6.5(a). As discussed in Ref.[30], PL linewidths of over 50 meV in $In_{1-x}Ga_xN$ cannot be explained by a purely statistical randomness in the alloy composition without considering carrier localization caused by significant compositional inhomogeneity.

This carrier localization effect can also be deduced from the temperature dependence of the PL signals. Fig. 6.6 shows the PL peak energy measured at room temperature and 11K. At low Ga concentrations, the low-temperature PL peak energy is lower than that at room temperature (by ~60meV at $x = 0$). As the Ga fraction increases, the difference is reduced and finally the low-temperature PL signal peaks at higher energy for large $x$. To understand the temperature behavior of these alloys, we have measured the PL signal of two samples over a wide temperature range (11K to 295K). The peak energy and the full width at half maximum (FWHM) are plotted as a function of temperature in Fig. 6.7. Both samples exhibit an anomalous temperature behavior: while the PL peak energy of InN monotonically increases as a function of temperature, a so-called inverted "S" shaped dependence is observed for $In_{0.89}Ga_{0.11}N$. This inverted S-shaped phenomenon has been observed previously in alloys such as GaInP [37], AlInAs [38], and Ga-rich InGaN [39], and in InGaN/GaN quantum wells [40], and is attributed to carrier localization. The FWHM of the PL of $In_{0.89}Ga_{0.11}N$ shows a rapid increase below the temperature (~75K) where the bandgap minimum occurs in the S-shaped curve. Afterwards, the FWHM stays essentially constant. Below 75K, carrier recombination is dominated by radiative processes, in which the carrier lifetime increases with increasing temperature. The photo-generated carriers have greater probability to relax down to the localized lower-energy states before recombining. The emission peak thus redshifts, and also significantly broadens on the lower energy side (raw data not shown here). Above

75K, non-radiative recombination becomes dominant. The carrier lifetime decreases as temperature increases and, as a result, the carriers quickly recombine before relaxing down to the lower-energy tail states. Therefore, the emission peak shifts to higher energy until the trend is compensated by the temperature-induced bandgap shrinkage. It should be emphasized that this is not the only possible explanation of the observed effect. The temperature dependence of the emission rate from the localized states can also contribute to the observed behavior of the photoluminescence.

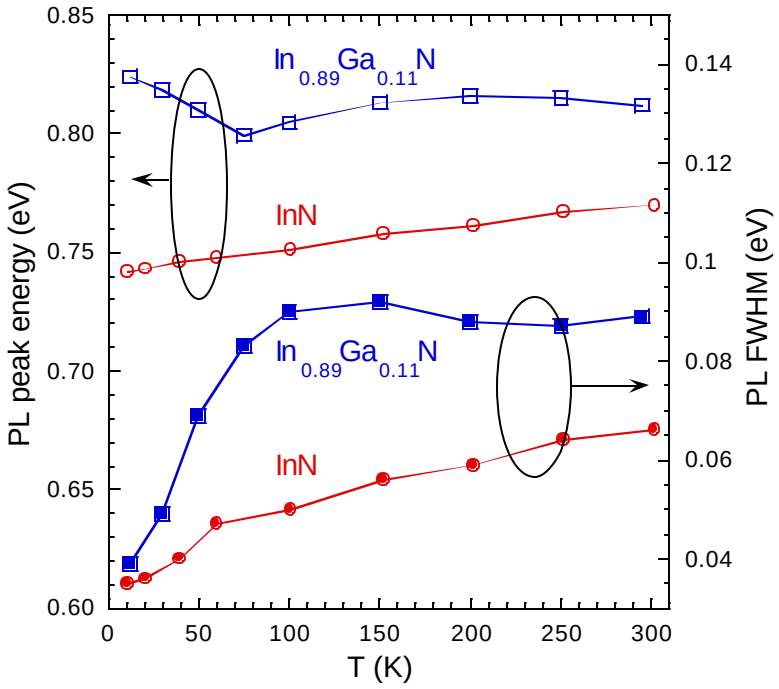


Fig. 6.7 Temperature dependencies of the PL peak energy and the FWHM for InN and $In_{0.89}Ga_{0.11}N$.

We have also studied band gap bowing in InAlN alloys grown on sapphire substrates using the MBE method at the same laboratory. In Fig. 6.8 the band gap energy is plotted as a function of Al content. The dependence is very similar to that observed in an InGaN alloy, and can be fitted using a bowing parameter of $b$=3.0eV.

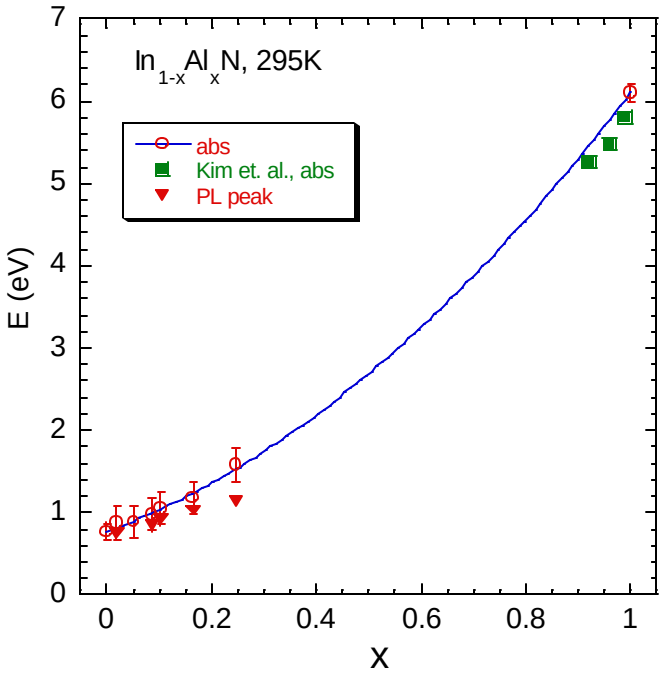


Fig. 6.8 The band gap bowing in InAlN alloys. The solid curve has bowing parameter *b*=3.0eV.

The discovery of the narrow band gap of InN and the small band gap bowing in the related ternary alloys greatly expands the spectral range covered by the direct band gaps of group III-Nitride ternaries. Their bandgap range now covers photon energies from the near infrared (InN), to the deep ultraviolet (AlN). This suggests the possibility of designing nitride-based solar cells that cover practically the full solar spectrum using one single ternary alloy. Furthermore, the bowing parameter values are also much smaller than the ones previously determined by fitting the composition dependence of the energy gaps of samples with small In content using a gap energy of 1.9 eV for InN.

It is interesting to compare the values of bowing parameter of different group III nitride ternaries. We have found a bowing parameter of 1.43 eV for InGaN [33]. We have also measured the composition dependence of the bandgap of wurtzite GaAlN alloys

grown by the same method. Our results show that their bandgap energy as a function of composition can be well fit with a bowing parameter of 1.4 eV. This value is in good agreement with the value of 1.33 eV reported by Shan *et. al.* [41]. Considering the bandgap difference between the end-point nitrides for each ternary, we note a proportional relationship between the bowing parameter and the bandgap difference. To illustrate this relationship, we define, for an alloy of the form AB, a normalized bowing parameter $b \equiv b \Big/ \left| E_g^A - E_g^B \right|$, and a dimensionless bandgap variation as $a(x_A) \equiv \left| E_g^{AB}(x_A) - E_g^B \right| \Big/ \left| E_g^A - E_g^B \right|$. The standard bowing equation in the form of Eq.(6.1) can be then rewritten as

$$a(x) = x - b \cdot x \cdot (1 - x). \tag{6.2}$$

In this equation, the dimensionless parameter $b$ describes the degree of the bandgap bowing relative to the bandgap difference of end-point materials. It is found that the value of $b$ is essentially the same for these three group III-N alloys. It only varies from 0.50 for AlGaN to 0.55 for InAlN alloys. Shown in Fig. 6.9 is the data of $a$ plotted as a function of $x$ for $In_{1-x}Al_xN$ measured in this work and from a previous report [42], for $Ga_{1-x}Al_xN$ and $In_{1-x}Ga_xN$ measured in this work, and for $In_{1-x}Ga_xN$ [29, 30, 43] adopted from the literature. It can be seen that although these gap energies were measured on different alloy systems and reported by different groups, they all fall onto one single curve when expressed in the reduced form of Eq. (6.2). A common normalized bowing parameter of $b$ = 0.54 well describes the universal composition dependence, as depicted by the curve in Fig.6.9. This scaling relationship is not surprising, though, because the main contribution to the bandgap bowing is due to the effects of composition disorder on the conduction and valence band edges [44]. Given a similar degree of disorder in space,

for a larger bandgap difference between alloy constituents, the potential perturbation caused by the composition fluctuations is larger; consequently the bandgap bowing effect is expected to be proportionally stronger.

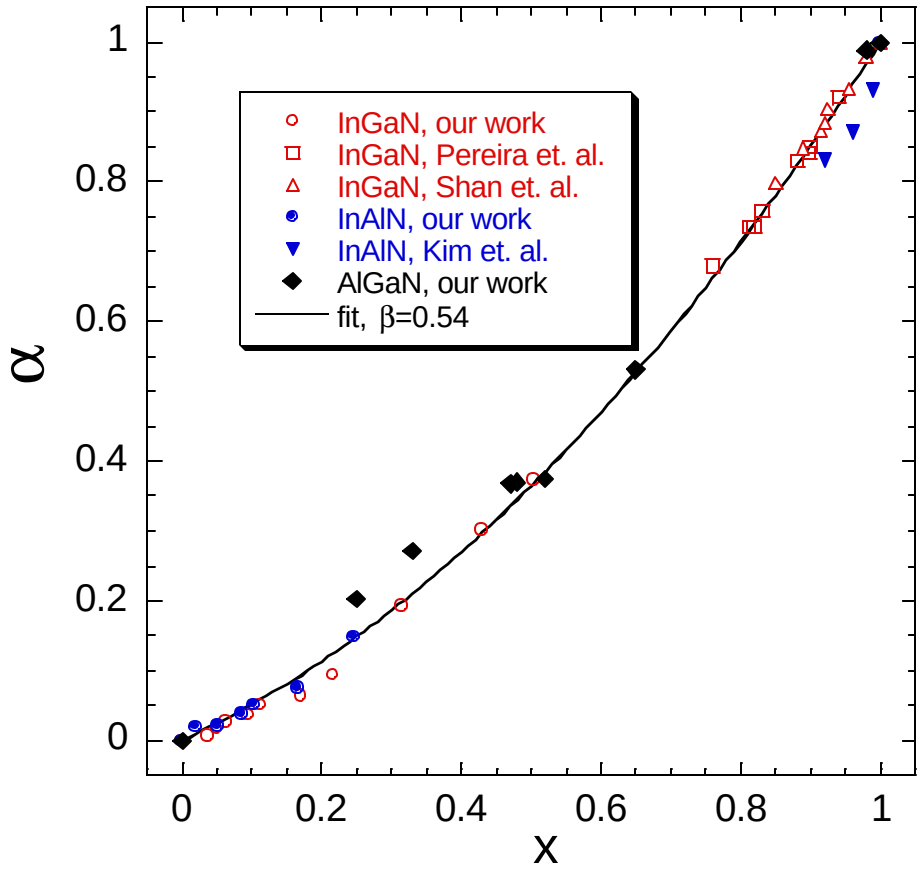


Fig. 6.9 Normalized bandgap variations shown as a function of $x$ for $In_{1-x}Ga_xN$, $In_{1-x}Al_xN$ and $Ga_{1-x}Al_xN$. The curve is a fit based on Eq.(6.2) using $b$ = 0.54.

The origin of the universal relationship describing the composition dependence of the bandgaps of group III-nitride alloys strongly suggests that similar arguments may be also used in the consideration of the composition dependence of band offsets. Since the total change of the bandgap is a sum of shifts of the conduction and the valence band

edges, it could be argued that the relationship given by Eq. (6.2) is also a proper scaling function for the band offsets. Namely, for any group III-nitride alloy system, the composition dependence of the conduction or the valence band offset is given by the band offsets of the end-point compounds multiplied by the universal scaling function in Eq. (6.2). This formula provides a method to estimate the band edge offsets between different group III-nitride alloys, which is an important issue in the design of heterostructure devices. Figure 6.10 shows the dependence of the bandgaps on the in-plane lattice constant obtained assuming a linear relationship between the lattice constant and the composition according to Vegard's law. The inset in Fig. 6.10 shows the conduction and valence band offsets calculated using the scaling function given by Eq. (6.2) and the experimentally determined valence band offsets of 1.05 eV for InN/GaN, and 0.70 eV for GaN/AlN [45].

The results shown in Fig. 6.10 suggest that a large gap difference is expected between GaN and the lattice matched $In_{0.18}Al_{0.82}N$. Also, it is important to note that most of the bandgap difference is accommodated by a large conduction band offset of almost 1 eV. This offers the interesting possibility of using $In_{0.18}Al_{0.82}N$/GaN heterostructures to confine the two-dimensional electron gas in lattice-matched GaN quantum wells. Such a heterostructure design would eliminate strain-induced polarization effects that are known to be partially responsible for the transfer of electrons from surface defects into the GaN quantum well in standard AlGaN/GaN high electron mobility transistors [46]. A reduction of the piezoelectric field-induced charge transfer could provide a better control of the heterostructure characteristics by enhancing the role of intentional doping of the barrier.

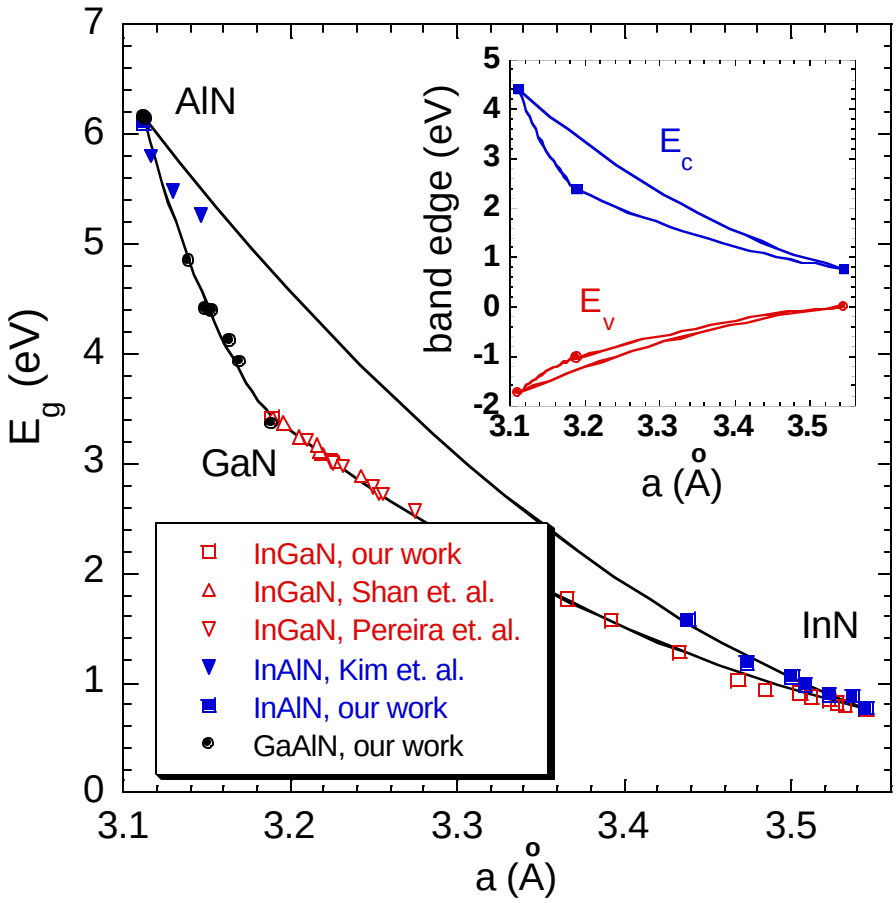


Fig. 6.10 Bandgaps of group III-nitride alloys as a function of in-plane lattice constant. Each curve between two end-points is the quadratic dependence of the bandgap of a corresponding ternary alloy described by the standard bowing equation. Inset, the calculated valence and conduction band edges of group III-N ternary alloys as a function of lattice constant. The points at lattice constants of 3.11, 3.19, and 3.54 Å represent AlN, GaN and InN respectively. All the band edge energies are referenced to the top of the valence band of InN.

## Glossary

| Acronym | Name | Page Introduced |
|---|---|---|
| BAC | Band anticrossing | 22 |
| CBAC | Conduction band anticrossing | 98 |
| CBE | Conduction band edge | 100 |
| CPA | Coherent potential approximation | 24 |
| DAC | Diamond anvil cell | 166 |
| DOS | Density of states | 28 |
| FWHM | Full width at half maximum | 86 |
| HMA | Highly mismatched alloy | 19 |
| LDA | Local density approximation | 137 |
| MBE | Molecular bean epitaxy | 41 |
| MOCVD | Metal-organic chemical vapor deposition | 41 |
| PL | Photoluminescence | 82 |
| PR | Photo-modulated reflectance | 38 |
| PT | Photo-modulated transmission | 149 |
| QW | Quantum well | 47 |
| SXE | Soft x-ray emission | 124 |
| VBAC | Valence band anticrossing | 116 |
| VBE | Valence band edge | 102 |
| VCA | Virtual crystal approximation | 3 |

# Appendices

1. Photoluminescence Spectroscopy

The term “radiative recombination” refers to the process by which electrons transit from high-energy states to low-energy states accompanied by photon emission of specific energy. Photon emission processes in semiconductors are characterized by the luminescence spectrum. These processes can only occur in a system in which electrons decay from excited states to equilibrium states. When electrons are excited by using a high-power photon flux with photon energies higher than the bandgap of the material, the resulting light emission process is called photoluminescence (PL). Figure A1 shows schematically the basic setup of a PL experiment. The laser provides the excitation and free carriers are generated in the sample. The photon emission of the sample as a result of free carrier recombination is collected and detected after being dispersed by the monochromator. The PL signal is amplified via a lock-in amplification circuit and recorded by a computer.

In the simplest description, the PL spectrum intensity of a direct-bandgap semiconductor is proportional to the production of the joint density of electronic states and the quasi-equilibrium Fermi distribution for the photo-excited electrons and holes [9],

$$I_{PL}(\hbar w) \propto \begin{cases} \sqrt{\hbar w - E_g}\,\exp\left[-\left(\hbar w - E_g\right)/\left(k_B T\right)\right] & (\hbar w \geq E_g) \\ 0 & (otherwise) \end{cases}$$

The PL line shape predicted by this equation is compared with experiments in Fig. A2 [104].

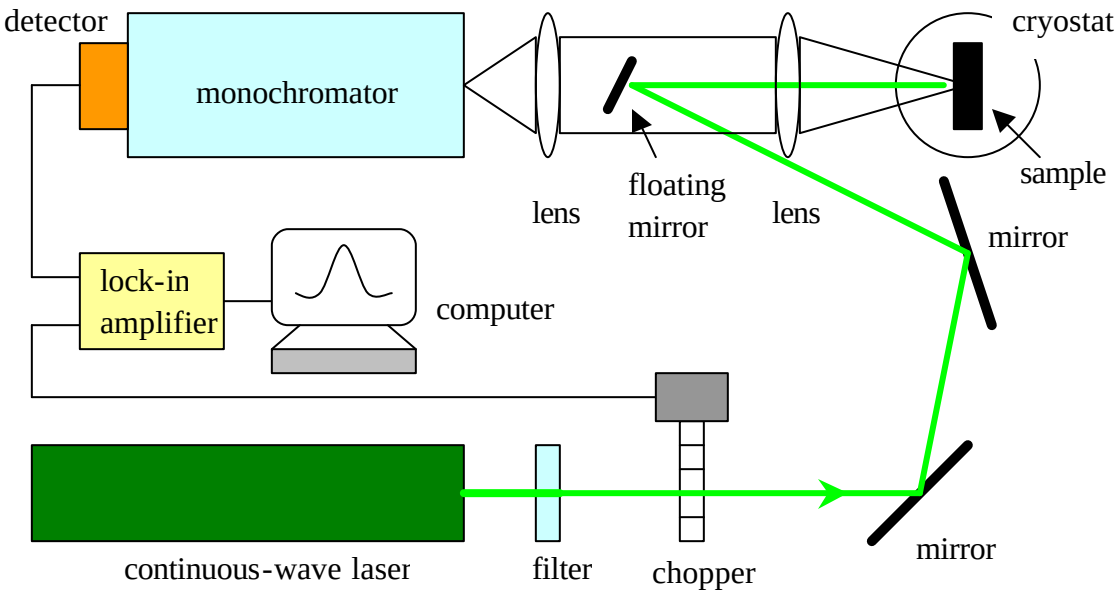


Fig. A1. Schematic diagram of a PL set-up.

Set-up I:

Laser: LEXEL-95, 8W Ar ion laser, 515 nm or 477 nm

Lock-in: SR530 lock-in amplifier

Detector: Liquid nitrogen cooled Ge detector

Monochromator: SPEX 1680, 0.22m Double Spectrometer

Set-up II:

Laser: Melles Griot HeCd 3074R-M-A02, 325 nm

Lock-in: SR530 lock-in amplifier

Detector: Hamamatsu GaAs detector

Monochromator: SPEX 1404, 0.8m Double Spectrometer

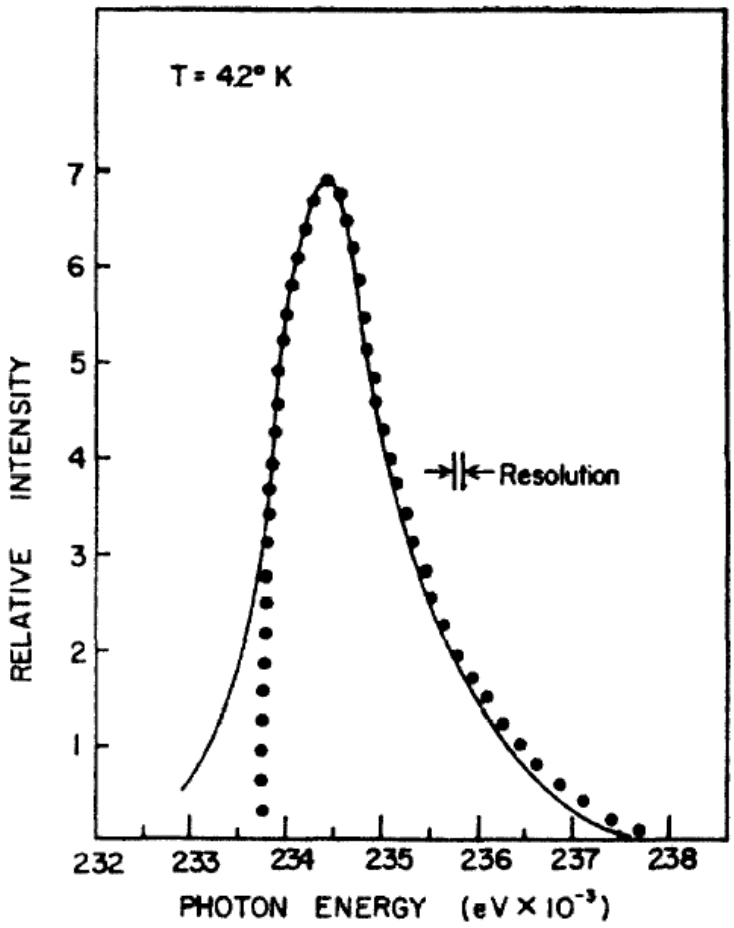


Fig. A2. PL spectrum (solid curve) for high-purity n-type InSb ($n$=5×10$^{13}$cm$^{-3}$) measured at 4.2 K. The calculated profile is shown as points [104]. The measured profile shows a tail on the low-energy side due to a band-tailing effect.

2. Photo-modulated Reflectance Spectroscopy

The dielectric function and consequently the optical properties of semiconductors (such as reflectance and transmission coefficients) have weak Van Hove singularities at interband critical points. However, their derivatives with respect to energy exhibit strong divergence at these critical points. Modulation spectroscopy directly measures the derivatives of the optical properties with respect to energy by using lock-in amplification techniques. In this way, the background can be largely suppressed and the critical-point transitions arise as sharp features in the modulation spectrum. The critical-point energies thus can be rather accurately determined.

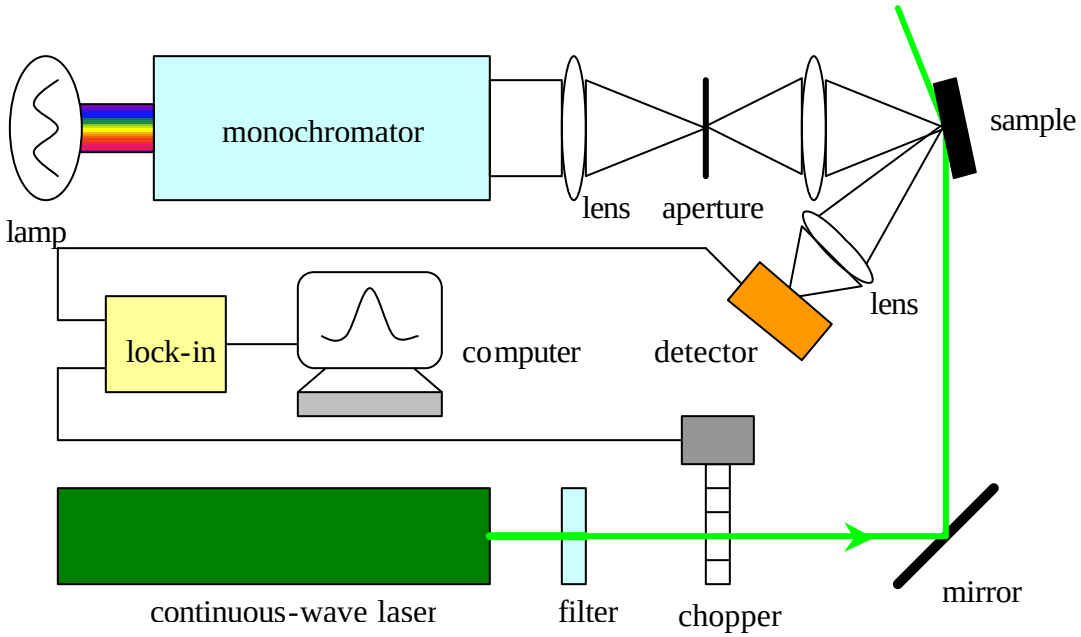


Fig. A3. Schematic of a PR set-up.

Figure A3 shows a Photo-modulated Reflectance (PR) experimental set-up. The chopped laser modulates the dielectric function of the sample; as a result, the reflectance of the sample in the laser-illuminated area is modulated at the chopping frequency (~ 300Hz). This reflectance spectrum is measured by using a standard reflection optics. Due to the sensitive dependence of the dielectric function on the electronic structure of the sample [9], the reflectance exhibits a drastic change near the critical transition energies of the material. These changes are recorded as the PR spectrum typically in the form of relative change in the reflectance $\Delta R / R$.

For $M_0$-type critical-point transitions, the transition energy can be determined by fitting the PR spectrum using the following equations [105].

$$\frac{\Delta R}{R} = a \cdot \mathrm{Re}\left[\frac{1}{(x-i)^{5/2}}\right] + b \cdot \mathrm{Im}\left[\frac{1}{(x-i)^{5/2}}\right] + c$$
$$= a \cdot \frac{\sin\left[\frac{5}{2}\arctan x\right]}{\left(1+x^2\right)^{5/4}} + b \cdot \frac{\cos\left[\frac{5}{2}\arctan x\right]}{\left(1+x^2\right)^{5/4}} + c,$$

where $x \equiv (E - E_0)/\Gamma$, and $a$, $b$ and $c$ are adjustable linear parameters in the fitting. The fit gives the critical energy $E_0$ and the broadening factor $\Gamma$.

As shown in Fig. A4, the reflectance spectrum shows weak features associated with the critical transitions at corresponding energy positions. With modulation spectroscopy, these critical transitions appear as a large, sharp, derivative-like line shape, which can be used to accurately determine the transition energy.

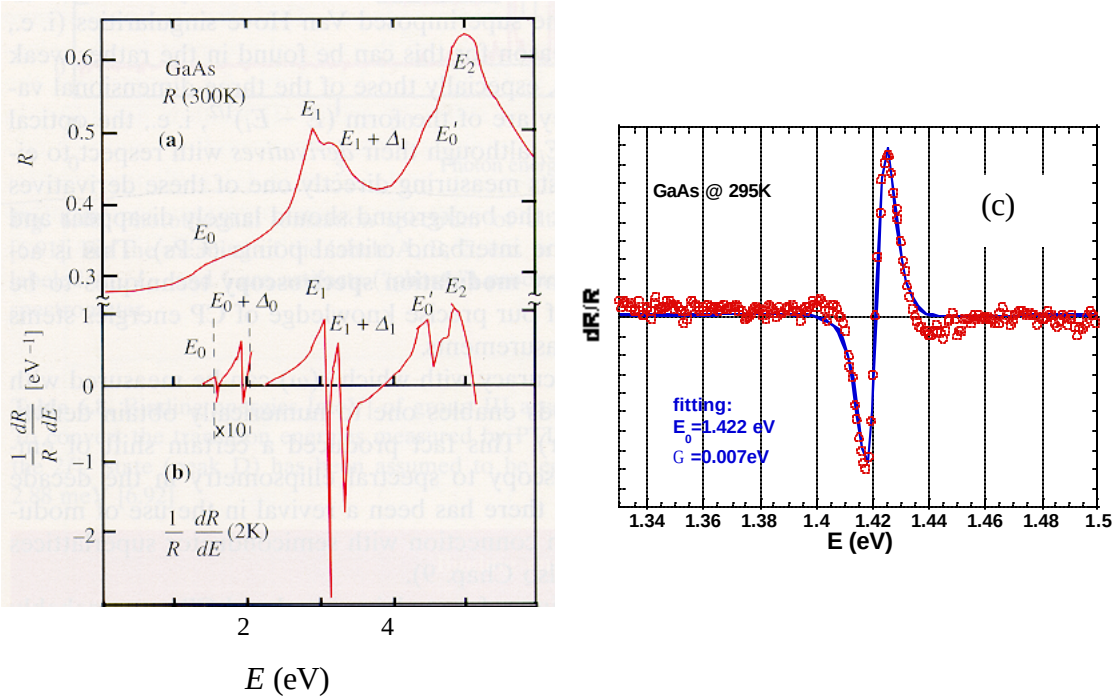


Fig. A4. (a) Room-temperature reflectance spectrum of GaAs. (b) Numerical differentiation of a reflectance curve of GaAs measured at 2K [9] showing various critical points. (c) Photo-modulated reflectance spectrum of a GaAs sample obtained at room temperature. The fit gives a bandgap energy of 1.422±0.007 eV.

Lamp: DRIEL-66181 Tungsten-Halogen lamp; DRIEL-66057 Xenon lamp

Laser: Omnichrome-100 HeCd laser, 442 nm or 325 nm

Detector: Si photodiode; Ge photodiode

Lock-in: SRS-SR850 DSP lock-in amplifier

Monochromator: Acton SpectroPro-500

3. Diamond Anvil Cell for Hydrostatic Pressure Studies

The application of hydrostatic pressure is achieved by using a diamond anvil cell (DAC). A detailed description of a DAC and its application can be found in Dr. L. Hsu's PhD thesis [106]. A magnified view of the essential parts of the DAC is shown in Fig. A5. The sample is usually thinned down to ~ 20 μm in thickness and cut into small chips of ~100×100 $\mu m^2$ in size before being loaded into the DAC. In our studies, alcohol (methanol : ethanol = 4:1) which works up to 200 kbar [107] was used as the pressure medium. The hydrostatic pressure is transmitted to the sample via the pressure medium when the upper and lower diamonds are pressed toward each other by external forces. The pressure is calibrated by the standard method of monitoring the red shift of the ruby R1 luminescence line [108].

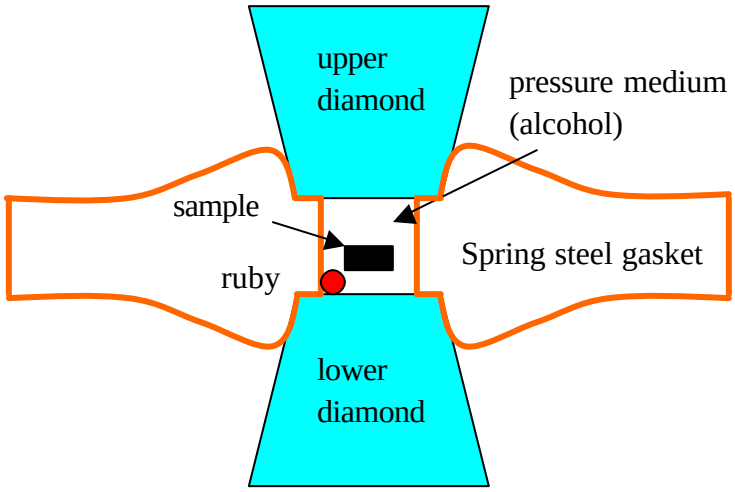


Fig . A5. Essential parts of the diamond anvil cell

The experimental setup of optical absorption with the DAC is shown schematically in Fig. A6. The sample in the tiny pressurized volume is magnified ($\times \sim$ 50) through a short-focus lens. Near the focal plane, an enlarged image of the sample and surrounding empty area in the pressurized volume is obtained. A small aperture is inserted into the image plane, through which the light intensity can be selectively detected. As shown in Fig. A6, when the aperture is placed in the shadow of the sample, the photon flux intensity is scanned and recorded as $I$; when the aperture is located in the empty area, $I_0$ is recorded. The absorption coefficient $a$ is then calculated as

$$a(\hbar w) = \frac{1}{d} \ln \frac{I_0(w)}{I(w)},$$

with $d$ the sample thickness.

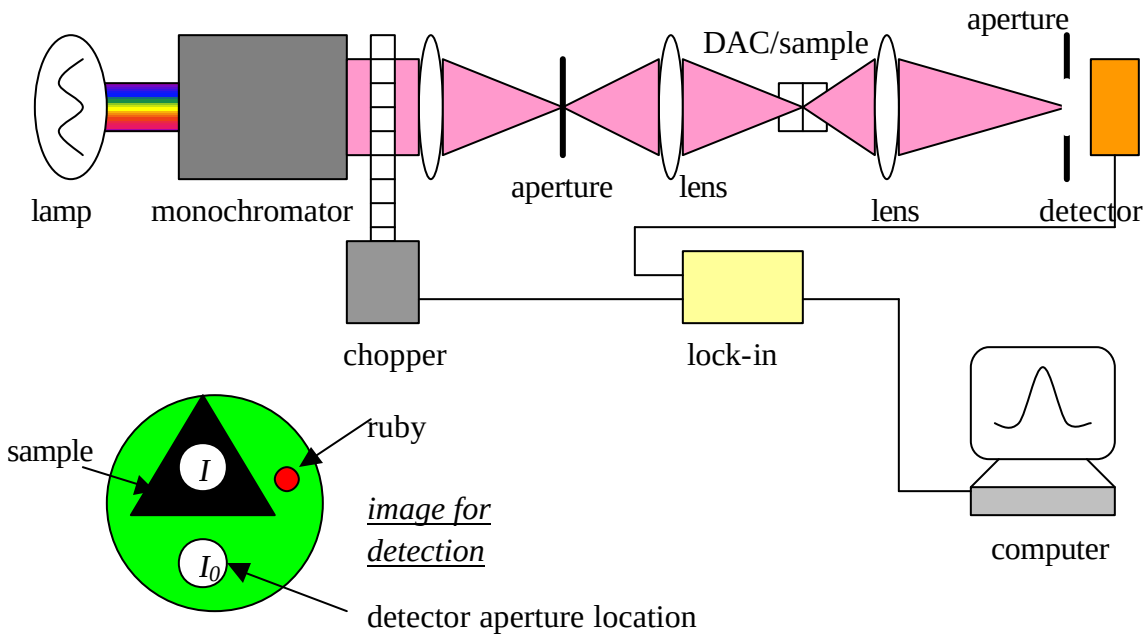


Fig. A6. Optics for absorption experiment with a DAC. The left lower part shows the schematic image of the sample area in the detector aperture plane.

## 4. Soft X-ray Emission Spectroscopy

Conventional optical experiments measure the energy separation between different states in semiconductors, such as the bandgap energy. However, it is sometimes useful to know the absolute energy locations of these states for different materials with respect to a common energy reference (*e.g.*, the vacuum level). Soft X-ray Emission (SXE) Spectroscopy is an important experimental tool that achieves this goal. The basic SXE process is illustrated in Fig. A7. Monochromatic x-rays from a synchrotron radiation source are incident on the sample and excite core electrons. The resultant core holes are filled immediately by electrons making transitions from higher lying states. Some of these transitions occur radiatively with the emission of x-ray photons at characteristic energies. If the photons associated with the transitions from the top valence band to the core levels are measured using a high-resolution spectrometer, the spectrum reflects the partial density of states of the valence band [109]. Since offsets between core levels in different elements are known from atomic physics, information on the relative energy positions of band states in different materials is obtained.

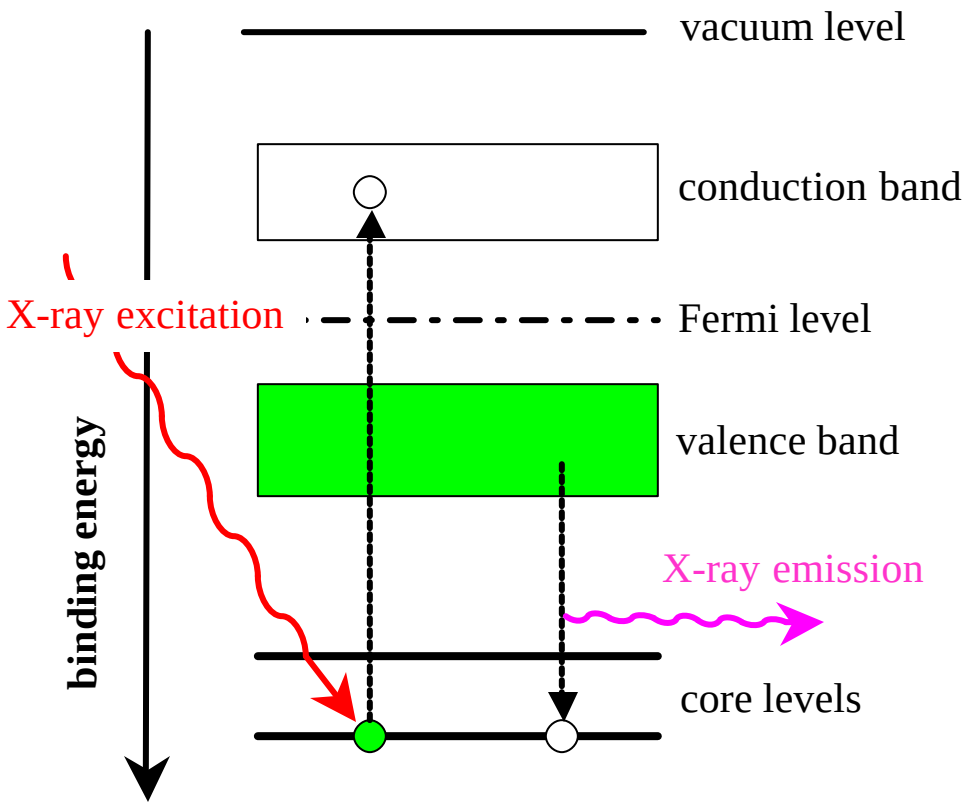


Fig. A7. Schematic illustration of soft x-ray emission spectroscopy.

5. Mathematica Programs for Computations Used in This Research

(1) Bound-state energies in $GaAs_{1-x}N_x$/GaAs single quantum well

```
"energy as a function of variable x"
ClearAll[Ega,Egb,mea,meb,La,Lb,Q,DEv,DEc,kea,keb,Ee,Ee1,Ee2,Ee3,we1,we2
,we3,plot1,plot2,plot3,plot,eexp,Eg0];

ClearAll[En,x,Em,Cnm,E1,E2,k,m,mm];
En=1.65;Eg0=1.42;
Em[k_]:=Eg0+1.973^2 k^2/(2 0.51 meb);
Cnm=2.7;
E1[x_,k_]:=0.5 ((En+Em[k])-Sqrt[(En-Em[k])^2+4 Cnm^2 x]);
m[x_,k_]=(1.973^2/0.51) (D[E1[x,k],{k,2}])^(-1);
mm[x_,k_]=(1.973^2/0.51) (D[E1[x,k],{k,1}]/k)^(-1);

Ega=E1[x,0]+0.0; Egb=Eg0;
mea=m[x,0]+0 0.067; meb=0.067;
Lb=202;La=70;
Q=0.0;

kea=Sqrt[2 (0.51/1.973^2) mea (Ee-Ega+DEv)];
we1=Ega-DEv+(Pi/La)^2/(2 0.51 mea/1.973^2);
we2=Ega-DEv+(2 Pi/La)^2/(2 0.51 mea/1.973^2);
we3=Ega-DEv+(3 Pi/La)^2/(2 0.51 mea/1.973^2);
keb=Sqrt[2 (0.51/1.973^2) meb (Egb-Ee)];
DEv=Q (Egb-Ega);
```

```
Ee1[x_]:=DEv+Ee/.FindRoot[Tan[kea La/2]==(keb mea)/(kea meb),
{Ee,Ega-DEv+0.001,Ega-DEv+0.0001,we1}];
Ee2[x_]:=DEv+Ee/.FindRoot[Tan[kea La/2]==-(kea meb)/(keb mea),
{Ee,(we1+0.0001),we1,we2}];
Ee3[x_]:=DEv+Ee/.FindRoot[Tan[kea La/2]==(keb mea)/(kea meb),
{Ee,(we2+0.0001),we2,we3}];

eexp={{0.012,1.3499},{0.016,1.3328},{0.020,1.3088},{0.028,1.27},{0.012,
1.2382},
{0.016,1.2152},{0.02,1.1735},{0.028,1.1297},
{0.045, 1.03},{0.045,1.18}};

plot1=ListPlot[eexp,Prolog->PointSize[0.05],Frame->True,GridLines-
>Automatic];

plot2=Plot[{Ee1[x],Ee2[x],Ee3[x]},{x,0.01,0.05},Frame->True,GridLines-
>Automatic];

plot3=Plot[E1[x,0],{x,0.01,0.05}];

Show[plot1,plot2,plot3];
```

(2) Variational calculations of the shallow donor ground state in $GaAs_{1-x}N_x$ in the context of the BAC model

```
ClearAll[g,g0,g00,k,ks,r,q,P,Q,R,Q0,Q1,E0,E1,E2,E12,E3,En,Cnm,x,Me,Mh,e
,
a,b,b1,b2,t,s,W,PE,PE0,PE00,PE1,PE10,PE11,PE12,KE0,KE1,KE2,KE3,CC,pr,V,
```

```
Eg];

e=15.5075;
Me=0.067;Mh=0.45;Eg0=1.52/(2 13.6 Me/e^2);
Cnm=2.7/(2 13.6 Me/e^2);
En:=Abs[(1.65-1.52+3 x+0.0015 pr-0.0108 pr)]/(2 13.6 Me/e^2);
pr=20;

x=0.01;b=0;

DEg1[x_]:=(En/2) (Sqrt[1+4 Cnm^2 x/(En)^2]-1);
Eg[x_]:=Eg0-Abs[DEg1[x]]-3 x/(2 13.6 Me/e^2);
DEg2[x_]:=(En/2) (Sqrt[1+4 Cnm^2 x/(En)^2]+1);

R[k_,q_,b_]:=-(1/(2 Pi)) Log[(b^2+(k+q)^2)/(b^2+(k-q)^2)];
Q1[k_,q_]:=-(b1 b2/Pi) (1/(b2^2+(k-q)^2)-1/(b2^2+(k+q)^2));

E0[k_]:=k^2/2;
E1[k_]:=(1/2) (En+E0[k]-Sqrt[(En-E0[k])^2+4 Cnm^2 x]);
E2[k_]:=(1/2) (En+E0[k]+Sqrt[(En-E0[k])^2+4 Cnm^2 x]);
E3[k_]:=k^2 Me/(2 Mh) ;

g00[k_,t_]:=k/(t+k^2)^2;
CC=Sqrt[Integrate[(g00[k,t])^2,{k,0,Infinity}]];
g0[k_,t_]=g00[k,t]/CC;

KE1[t_]:=Re[NIntegrate[g0[k,t] (E1[k]+DEg1[x]) g0[k,t],
{k,0,Infinity}]];
KE3[t_]:=Re[NIntegrate[g0[k,t] E3[k] g0[k,t], {k,0,Infinity}]];
```

```
PE00[t_]:=Re[Integrate[g0[k,t] R[k,q,b] g0[q,t],{q,0,Infinity},
{k,0,Infinity}]]; PE0[t_]:=N[PE00[t]];

W[t_]:=KE1[t]+ KE3[t]+PE0[t];

Plot[{En,E1[k],E2[k]},{k,0,40}];

Plot[W[t] (2 13.6 10^3 Me/e^2),{t,0.5,3},GridLines->Automatic, Frame-
>True];

N[0.053 e/Me]

N[1.52-DEg1[x] (2 13.6 Me/e^2)-0.03]
```

(3) State broadening and related effects of the BAC model based on Green's function calculation

```
"GF, JDOS"
ClearAll[R0,V,x,Gm,ImG,G,EE,Ek,k,R,P1,P2,P3,P4,P5,P6,
Rhh,Rlh,Rso,Rtotal,Eplus,Eminus];

Ed=0.23+Eg0;
Eb=70.4;
V=2.7;
Eg0=1.42;
Me=0.067;
Mhh=0.51;
```

```
Mlh=0.082;

Mso=0.154;

Delta=0.34;


x=0.01;


Eplus=0.5 (Eg0+Ed+Sqrt[(Eg0-Ed)^2+4 V^2 x]);

Eminus=0.5 (Eg0+Ed-Sqrt[(Eg0-Ed)^2+4 V^2 x]);

R0[EE_]:=4 Pi Sqrt[EE-Eg0]/Eb^(3/2);

Gm=Pi V^2 R0[Ed];


G[EE_, Ek_]:=(EE-(Ed+I Gm))/((EE-Ek+I 10^(-6)) (EE-(Ed+I Gm))-V^2 x);


R[EE_]:=(1/Pi) Abs[NIntegrate[R0[Ek] Im[G[EE,Ek]],{Ek,Eg0,Eb},

MinRecursion->3,MaxRecursion->10,WorkingPrecision->16]];


Rhh[EE_]:=(1/Pi) Abs[NIntegrate[R0[Ek] Im[G[EE-(Me/Mhh)

Ek,Ek]],{Ek,Eg0,Eb},

MinRecursion->3,MaxRecursion->10,WorkingPrecision->16]];


P1=Plot[R0[Ek],{Ek,Eg0,3},Frame->True,PlotStyle->{RGBColor[0,1,0]}];


P2=Plot[R[EE],{EE,0,3},Frame->True,PlotStyle->{RGBColor[1,0,0]}];


Show[P1,P2];
```

(4) BAC effect in the entire Brillouin zone for $GaP_{1-x}N_x$

```
ClearAll[x,y,Eg,Cnm,V0,k0,a,b,M,En,Em,Eml,Emx,k,Vnm,M0,q,kk,
W1,W2,f11,f12,f21,f22,p0,p1,p2,p3,p4,p5,p6,n,EEm,EEn,WW1,WW2,i];

"30K, GaPN";
"GaP, Valance: X:-2.32eV; Gama: 0eV";

V0=3.05;
h=6.63 10^(-34);Me=9.31 10^(-31); e=1.6 10^(-19);
a=5.45 10^(-10);

En[k_]:=2.15;

Eml[k_]:=(2.6439+0.49415 (k/1.15)+ 46.922 (k/1.15)^2+(-23.368)
(k/1.15)^3+(-1986.2) (k/1.15)^4+
(-9418.9) (k/1.15)^5+(-20899) (k/1.15)^6+(-25072) (k/1.15)^7+(-15715)
(k/1.15)^8+
(-4043.9) (k/1.15)^9);
Emx[k_]:=(2.6399+(-0.42652) (k/1.15)+22.452 (k/1.15)^2+390.93
(k/1.15)^3+(-3313.2) (k/1.15)^4+
10326 (k/1.15)^5+(-16856) (k/1.15)^6+15419 (k/1.15)^7+(-7511.9)
(k/1.15)^8+1522.8 (k/1.15)^9);
Em[k_]:=(Which[k<=0,Eml[k],k>0,Emx[k]])+(2.90-Eml[0]) (1-k)+(2.35-
Emx[1]) k;

p0=Plot[{Em[k],En[k]},{k,-0.87,1},Frame->True,GridLines->Automatic,
PlotStyle->{{Dashing[{0.01,0.01}]}}];

Vnm[x_,k_]:=V0 k0^4 Sqrt[x] /(k0^2+k^2)^2;
```

```
M0:={{En[k],Vnm[x,k]},{Vnm[x,k],Em[k]}};
MatrixForm[M0];

W1:=Eigenvalues[M0][[1]];
f11:=Eigenvectors[M0][[1]][[1]];
f12:=Eigenvectors[M0][[1]][[2]];

W2:=Eigenvalues[M0][[2]];
f22:=Eigenvectors[M0][[2]][[2]];
f21:=Eigenvectors[M0][[2]][[1]];

x=0.023;k0=1.09;

P1=Plot[Vnm[x,k],{k,-0.87,1}];

p2=Plot[{W1,W2},{k,-0.87,1},Frame->True,GridLines->Automatic];

Show[p0,p2];

Array[kk,n];Array[EEm,n];Array[EEn,n];Array[WW1,n];Array[WW2,n];n=19
5+1;
For[i=1,i<n+1,i++;
kk[i]={-0.9,-.88,-.86,-.84,-.82,-0.8,-.78,-.76,-.74,-.72,
-0.7,-.68,-.66,-.64,-.62,-0.6,-.58,-.56,-.54,-.52,
-0.5,-.48,-.46,-.44,-.42,-0.4,-.38,-.36,-.34,-.32,
-0.3,-.28,-.26,-.24,-.22,-0.2,-.18,-.16,-.14,-.12,
-0.1,-.08,-.06,-.04,-.02,0,0.02,0.04,0.06,0.08,
.1,0.12,0.14,0.16,0.18,.2,0.22,0.24,0.26,0.28,
.3,0.32,0.34,0.36,0.38,.4,0.42,0.44,0.46,0.48,
```

```
.5,0.52,0.54,0.56,0.58,.6,0.62,0.64,0.66,0.68,
.7,0.72,0.74,0.76,0.78,.8,0.82,0.84,0.86,0.88,
.9,0.92,0.94,0.96,0.98,1}[[i]];
EEm[i]=Em[kk[i]];EEn[i]=En[kk[i]];WW1[i]=W1[kk[i]];WW2[i]=W2[kk[i]];];

Transpose[{Array[EEm,n],Array[EEn,n],Array[WW1,n],Array[WW2,n]}]
```

(5) Valence band anticrossing applied to $ZnS_{1-x}Te_x$

```
"ZnS(1-x)Tex, 0<=x<=1; Interpolation";
"referenced to ZnTe VB-top";

ClearAll[p,x,ES,ES0,EZT,EZT0,CmS,a1S,a1ZT,z2ZT,EZTminus,EZTplus,a1ZTS,a
2ZTS,
a1ZST,a2ZST,n1,n2,a1,a2,P1,P2,P3,P4];

ES[p_]:=ES0+a1S p;
EZT[p_,x_]:=EZT0+a1ZT p+a2ZT p^2-0.3 (1-x);
ES0=2.6;
a1S=1.5 10^(-3);
EZT0=2.24;
a1ZT=10.9 10^(-3);
a2ZT=-4.25 10^(-5);
CmS=1;

EZTminus[p_,x_]:=0.5 ((ES[p]+EZT[p,x])-Sqrt[(ES[p]-EZT[p,x])^2+4 CmS^2
(1-x)]);
```

```
EZTplus[p_,x_]:=0.5 ((ES[p]+EZT[p,x])+Sqrt[(ES[p]-EZT[p,x])^2+4 CmS^2
(1-x)]);

Series[EZTplus[p,x],{p,0,2}];

a1ZTS[x_]:=D[EZTminus[p,x],p] /. p->0;
a2ZTS[x_]:=0.5 D[EZTminus[p,x],{p,2}] /. p->0;

"Plot[a1ZTS[x],{x,0,1},Frame->True,PlotStyle->{RGBColor[1,0,0]}];
Plot[a2ZTS[x],{x,0,1},Frame->True,PlotStyle->{RGBColor[0,0,1]}];";

a1ZST[x_]:=6.35 10^(-3);
a2ZST[x_]:=-1.31 10^(-5);
a1[x_]:=x^n1 a1ZTS[x]+(1-x^n1) a1ZST[x];n1=1;
a2[x_]:=x^n2 a2ZTS[x]+(1-x^n2) a2ZST[x];n2=2;

P1=Plot[a1[x],{x,0,1},Frame->True,PlotStyle->{RGBColor[1,0,0]}];
P2=Plot[a2[x],{x,0,1},Frame->True,PlotStyle->{RGBColor[0,1,0]}];

a1Data={{0.0,0}};
a2Data={{0.0,0}};

P3=ListPlot[a1Data];
P4=ListPlot[a2Data];

Show[P1,P3];
Show[P2,P4];

"ZnSTex, 0<=x<1, 8X8, bowing";
```

```
"referenced to ZnS VB_top";

ClearAll[r1,r2,r3,Delta0,Ctm,Et0,kx,ky,kz,k,k2,Hv,L,a,b,DD,S,V,
Ehh0,Ehh1,Ehh2,Elh0,Elh,Elh1,Elh2,Mt,Mlh,Mhh,Mso,
Eso0,Eso,Eso1,Eso2,Et,Et1,Et2,Eig,Ec,Dc,Dc2,Dv,
E0Data,Delta0Data,EcData,EvData,E0PLData,E0absData,EsoData,
P5,P6,P7,P8,P9,P10,P13,P14,offset];

hbar=1973;
m0=0.511*10^6;
r1=4.30;
r2=0.59;
r3=1.34;
Delta0=0.07;

offset=157.2;"x-ray energy offset, energy difference between S-2p core
level and the ZnS VB_top";
Ctm=0.5;
Et0=1.2;

Dv=1.2;
Dc=-0.20;Dc2=0;
Dd=0.89;
Ec[kx_,x_]=3.64+Dc x-Dc2 x^2;

kx=.;
ky=0;
kz=0;
```

```
H[kx_,x_]=-hbar^2/m0 ((kx^2+ky^2) (r1+r2)+kz^2 (r1-2 r2))+Dv x;
L[kx_,x_]=-hbar^2/m0 ((kx^2+ky^2) (r1-r2)+kz^2 (r1+2 r2))+Dv x;
a[kx_]=Sqrt[3] hbar^2/m0 (kz (kx-I ky) r3);
b[kx_]=Sqrt[3]/2 hbar^2/m0 ((kx^2-ky^2) r2-2 I kx ky r3);
DD[kx_,x_]=L[kx,x]-H[kx,x];
S[kx_,x_]=1/2 (L[kx,x]+H[kx,x])-Delta0-Dd x;
V[x_]=Ctm Sqrt[x];

Hv[kx_,x_]:={{H[kx,x],a[kx],b[kx],0,I a[kx]/Sqrt[2],-I Sqrt[2] b[kx],
(1-I) V[x]/Sqrt[2], 0},
{Conjugate[a[kx]],L[kx,x],0,b[kx],I DD[kx,x]/Sqrt[2],I Sqrt[3/2]
a[kx],I Sqrt[2/3] V[x], (-1-I) V[x]/Sqrt[6]},
{Conjugate[b[kx]],0,L[kx,x],-a[kx],-I Sqrt[3/2] Conjugate[a[kx]],I
DD[kx,x]/Sqrt[2],(1+I)/Sqrt[6] V[x], Sqrt[2/3] V[x]},
{0,Conjugate[b[kx]],-Conjugate[a[kx]],H[kx,x],-I Sqrt[2]
Conjugate[b[kx]],-I Conjugate[a[kx]]/Sqrt[2],0,(1-I)/Sqrt[2] V[x]},
{-I Conjugate[a[kx]]/Sqrt[2],-I DD[kx,x]/Sqrt[2],I Sqrt[3/2] a[kx], I
Sqrt[2] b[kx], S[kx,x], 0, 1/Sqrt[3] V[x],(1-I) V[x]/Sqrt[3]},
{I Sqrt[2] Conjugate[b[kx]], -I Sqrt[3/2] Conjugate[a[kx]], -I
DD[kx,x]/Sqrt[2], I a[kx] /Sqrt[2], 0, S[kx,x], (-1+I) V[x]/Sqrt[3],-I
V[x]/Sqrt[3]},
{(1+I) V[x]/Sqrt[2], -I V[x] Sqrt[2/3], (1-I) V[x]/Sqrt[6],0,
V[x]/Sqrt[3], (-1-I) V[x]/Sqrt[3], Et0,0},
{0,(-1+I) V[x]/Sqrt[6],V[x] Sqrt[2/3],(1+I) V[x]/Sqrt[2],(1+I)
V[x]/Sqrt[3],I V[x]/Sqrt[3],0,Et0}};

Eig[kx_,x_]:=Sort[Chop[Re[Eigenvalues[Hv[kx,x]]]]];

{Eso1[kx_,x_],Eso2[kx_,x_],Elh1[kx_,x_],Elh2[kx_,x_],
```

```
Ehh1[kx_,x_],Ehh2[kx_,x_],Et1[kx_,x_],Et2[kx_,x_]}:={Eig[kx,x][[1]],
Eig[kx,x][[2]],
Eig[kx,x][[3]],
Eig[kx,x][[4]],
Eig[kx,x][[5]],
Eig[kx,x][[6]],
Eig[kx,x][[7]],
Eig[kx,x][[8]]};

P10=Plot[{Ehh1[0,x]+offset,Elh1[0,x]+offset,Eso1[0,x]+offset,Et1[0,x]+o
ffset,Ec[0,x]+offset},{x,0,0.3},
PlotStyle-
>{RGBColor[1,1,0],RGBColor[0,1,0],RGBColor[0,1,1],RGBColor[1,0,0],
RGBColor[0,0,1]},GridLines->Automatic, Frame->True];

E0Data={{0.0,3.4600},{0.00700,3.4700},{0.0250,3.2800},{0.1450,2.7700},{
0.2160,2.4100},{0.2840,2.2600},
{0.5350,2.3100},{0.580,2.1670},{0.677,2.0300},{0.798,2.2130},{0.90,2.17
00}};
E0absData={{0.0,3.6070},{0.2160,2.6380},{0.5800,2.1422},{0.6770,2.0542}
,{0.7980,2.0264},{0.900,2.1110},
{1.00,2.2500},{0.2160,2.61},{0.284,2.477}};
P5=ListPlot[E0Data,PlotStyle->{RGBColor[1,0,0],PointSize[0.02]}];
P13=ListPlot[E0absData,PlotStyle->{RGBColor[1,0,1],PointSize[0.02]}];

EsoData={{0.0,3.6770},{0.798,2.9300},{0.900,3.0210},{1.00,3.2000}};
P14=ListPlot[EsoData,PlotStyle->{RGBColor[0,1,1],PointSize[0.02]}];
```

```
E0PLData={{0.00,3.6810},{0.00700,2.4000},{0.0250,2.3800},{0.1450,2.3060
},{0.2160,2.2540},
{0.2840,2.2460},{0.5350,2.1000},{0.5800,2.0840},{0.6770,2.0650},{0.7980
,2.0600},{0.9000,2.0940},
{1.000,2.2515}};
P9=ListPlot[E0PLData,PlotStyle->{RGBColor[0,0,1],PointSize[0.02]}];

EcData={{0.0,160.83},{0.007,160.80},{0.025,160.68},{0.145,160.64},{0.21
6,160.68},{0.284,160.56},
{0.535,160.44},{0.580,160.40},{0.677,160.36},{0.798,160.28},{0.90,160.2
1},{0.95,160.29}};
P6=ListPlot[EcData,PlotStyle->{PointSize[0.02]}];

EvData={{0.0,157.37},{0.0070,157.33},{0.0250,157.40},{0.1450,157.87},{0
.2160,158.27},{0.2840,158.30},
{0.5350,158.13},{0.5800,158.23},{0.6770,158.33},{0.7980,158.07},{0.9000
,158.04}};
P8=ListPlot[EvData,PlotStyle->{PointSize[0.02]}];

P7=Plot[{Ec[0,x]-Ehh1[0,x],Ec[0,x]-Elh1[0,x],
Ec[0,x]-Et1[0,x],Ehh1[0,x]-Eso1[0,x]},{x,0,0.3},PlotStyle-
>{RGBColor[0,1,1],
RGBColor[0,1,0],RGBColor[1,0,0],RGBColor[1,0,1]},
GridLines->Automatic, Frame->True];

Show[P10,P8,P6];
Show[P7,P5,P9];
```

```
ClearAll[E0,x,n3,n4,n5,n6,n7,P11,P12,EvZTS,EvZST,Ev,EcminusZTS,EcplusZT
S,EcminusZST,EcplusZST,
Ecminus,Ecplus,Ehh,Elh,E0fit,Eso,Esofit];

EvZTS[x_]=offset+Dv x;
EvZST[x_]:=Et1[0,x]+offset;
Ev[x_]:=x^n3 EvZTS[x]+(1-x^n3) EvZST[x];n3=1;
Ehh[x_]:=x^n3 EvZTS[x]+(1-x^n3) (Ehh1[0,x]+offset);
Elh[x_]:=x^n3 EvZTS[x]+(1-x^n3) (Elh1[0,x]+offset);
E0fit[x_]:=x^n6 (Ecminus[x]-Ev[x])+(1-x^n6) (Ecminus[x]-Ehh[x]);n6=1/3;
Eso[x_]:=x^n7 (offset-Delta0+(Dv-Dd) x)+(1-x^n7)
(Eso1[0,x]+offset);n7=1;
Esofit[x_]:=Ecminus[x]-Eso[x];

EcminusZTS[x_]:=offset+Dv+EZTminus[0,x];
EcplusZTS[x_]:=offset+Dv+EZTplus[0,x];
EcminusZST[x_]:=offset+Ec[0,x];
EcplusZST[x_]:=offset+Ec[0,x]+1;"?";
Ecminus[x_]:=x^n4 EcminusZTS[x]+(1-x^n4) EcminusZST[x];n4=1;
Ecplus[x_]:=x^n5 EcplusZTS[x]+(1-x^n5) EcplusZST[x];n5=0;
P11=Plot[{Ev[x],Eso[x],Ecminus[x],Ehh[x],Elh[x]},{x,0,1},Frame->True,
PlotStyle-
>{RGBColor[1,0,0],RGBColor[0,1,0],RGBColor[0,0,1],RGBColor[1,0,1],RGBCo
lor[0,1,1]}];
P12=Plot[{Ecminus[x]-Ev[x],Ecminus[x]-
Ehh[x],E0fit[x],Esofit[x]},{x,0,1},Frame->True,
GridLines->Automatic,PlotStyle-
>{RGBColor[0,0,1],RGBColor[0,1,0],RGBColor[1,0,0],RGBColor[1,0,1]},
PlotRange->{{0,1},{1.5,4}}];
```

```
Show[P11,P8,P6];

Show[P12,P5,P9,P13,P14];
```

(6) Non-linear fitting for the determination of electron effective mass of InN by plasma reflection experiments

```
"InN plasma edge";
ClearAll@data, er, ei, n, k, R, w, wp, wr, wp0, wr0, a, b, a0, b0, erinfinity, parameters, P1, P2D;
<<Statistics`NonlinearFit`;

data = 881000, 0.7<, 81500, 0.6<, 82000, 0.35<, 82500, 0.15<, 83000, 0.08<, 83500, 0.08<,
   84000, 0.081<, 84500, 0.082<<;
erinfinity = 5.2;

er@w_, wp_, wr_D = erinfinity * i1 - Hwp • wL^2 / 1 + Hwr • wL^2 y;
                   k                                          {
ei@w_, wp_, wr_D = erinfinity * wr • w / 1 + Hwr • wL^2;

n@w_, wp_, wr_D = & er@w, wp, wrD + " er@w, wp, wrD^2 + ei@w, wp, wrD^2 / 2;

k@w_, wp_, wr_D = ei@w, wp, wrD / " 2 er@w, wp, wrD + 2 " er@w, wp, wrD^2 + ei@w, wp, wrD^2;

R@w_, wp_, wr_, a_, b_D = a * HHn@w, wp, wrD - 1L^2 + k@w, wp, wrD^2L / HHn@w, wp, wrD + 1L^2 + k@w, wp, wrD^2L + b;

NonlinearFit@data, R@w, wp, wr, a, 0D, 8w<, 8wp, wr<D;
parameters =
  BestFitParameters • . NonlinearRegress@data, R@w, wp, wr, a, 0D, 8w<, 8wp, wr, a<,
    RegressionReport ® BestFitParametersD;
8wp0, wr0, a0< = 8wp, wr, a< • . parameters

P1 = ListPlot@data, PlotStyle ® 8PointSize@0.02D<D;
P2 = Plot@R@w, wp0, wr0, a0, 0D, 8w, 500, 5000<D;
Show@P1, P2D
```

## References


[1] J. A. VanVechten et. al., Phys. Rev. **B 1**, 3351 (1970).

[2] D. Richardson et. al., J. Phys. **C 5**, 821 (1972).

[3] L. Nordheim, Ann. Physik **9**, 607 and 641 (1931).

[4] M. Kondow, et. al., J. Cryst. Growth, **188**, 255 (1998); M. Kondow, et. al., J. J. Appl. Phys., **35**, 1273(1996).

[5] N. Baillargeon, et. al., Appl. Phys. Lett. **60**, 2540(1992).

[6] W. Shan, et. al., Appl. Phys. Lett. **76**, 3251 (2000).

[7] W. G. Bi et. al., J. Appl. Phys. **80**, 1934(1996).

[8] W. Shan, et. al., Appl. Phys. Lett., **75**, 1410 (1999).

[9] Peter Y. Yu and Manuel Cardona, *Fundamentals of Semiconductors: Physics and Materials Properties*. Springer-Verlag, New York (1996).

[10] H. P. Hjalmarson, et. a., Phys. Rev. Lett. **44**, 810 (1980).

[11] D. G. Thomas et. al., Phys. Rev. **150**, 680 (1966); D. J. Wolford, et. al., in *Physics of Semiconductors* 1984, ed. by J. D. Chadi and W. A. Harrison (Springer, New York 1984).

[12] L. Pauling, J. Am. Chem. Soc. **54**, 3570(1932).

[13] R. S. Mulliken, J. Chem. Phys. **2**, 782(1934).

[14] W. Gordy, et. al., J. Chem. Phys. **24**(2), 439(1956).

[15] J. Tietjen, et. al., J. Electrochem. Soc. **113**, 724 (1966).

[16] J. E. Bernard et. al., Phys. Rev. **B36**, 3199 (1987).

[17] M. Weyers, et. al., Jpn. J. Appl. Phys. **31**, L853(1992).

[18] J. C. Harmand, et. al., J. Crystl. Growth, **227-228**, 553(2001).

[19] B. N. Murdin, et. al., Appl. Phys. Lett. **78**, 1558(2001).

[20] W. Walukiewicz, et. al., Phys. Rev. Lett. **85**, 1552(2000).

[21] K. Uesugi, et. al., Appl. Phys. Lett. **74**, 1254(1999).

[22] B. M. Keyes, et.al., NCPV Photovoltaics Program Review, AIP Conference Proceedings **462**, 511 (1999).

[23] L. Malikova, et. al., J. Electron. Mat. **27**, 484 (1998).

[24] R. Bhat, et. al., J. Crystl. Growth, **195**, 427 (1998).

[25] J. A. Van Vechten et. al., Phys. Rev., **B 8**, 3351 (1970).

[26] S. Sakai, et. al., Jpn. J. Appl. Phys. Part 1 **32**, 4413 (1993).

[27] Su-Huai Wei et. al., Phys. Rev.Lett., **76**, 664 (1996).

[28] E. D Jones, et. al., Phys. Rev. **B 60**, 4430 (1999).

[29] T. Mattila, et. al., Phys. Rev. **B 60**, R11 245 (1999).

[30] Lin-Wang Wang, Appl. Phys. Lett., **78**, 1565 (2001); N. G. Szwacki et. al., Phys. Rev. **B 64**, 161201 (2001).

[31] A. Al-Yacoub et. al., Phys. Rev. **B 62**, 10 847 (2000).

[32] Y. Zhang, et. al., Phys. Rev. **B 63**, 161303 (2001).

[33] W. Walukiewicz, et. al., Proc. 195$^{th}$ Electrochem. Soc. Meeting, Seattle, WA, **99-11**, 190 (1999).

[34] W. Shan, et. al., Phys. Rev. Lett. **82**, 1221(1999).

[35] M. Hettrich, et. al., **76**, 1030(2000).

[36] J. Wu, et. al., Phys. Rev. B **64**, 85320(2001).

[37] K. M. Yu, et. al., Phys. Rev. B **61**, 13337(R) (2000).

[38] J. Wu, et. al., Phys. Rev. B **65**, 233210 (2002).

[39] P. W. Anderson, Phys. Rev. **124**, 41(1961).

[40] A. Yoshimori et. al., J. Magn. Magn. Mat. **31**, 475(1983).

[41] P. A. Lee, et. al., Comments Cond. Mat. Phys. **12**, 99(1986); C. M. Varma et. al., Phys. Rev. B **13**, 2950(1976).

[42] D. M. Newns et. al., Advances in Physics, **36**, 799(1987); Peter S. Riseborough, Phys. Rev. B, **45**, 13984(1992).

[43] A. N. Kocharyan, Soc. Phys. Solid State **28**(1), 6(1986).

[44] M. A. Ivanov et. al., Sov. Phys. JETP **49**, 510(1979); M. A. Ivanov et. al., Sov. Phys. JETP **61**, 1033(1985).

[45] N. F. Mott and E. A. Davis, *Electronic Processes in Non-Crystalline Materials*, Clarendon Press, Oxford (1971).

[46] G. M. Zaslavskii, et. al., Sov. Phys. JETP, **40**, 707(1975); M. A. Ivanov et. al., Sov. Phys. Solid State, **16**, 2140(1975).

[47] S. Doniach and E. H. Sondheimer, *Green's Functions for Solid State Physics*, W. A. Benjamin, Inc. 1974.

[48] Fumiko Yonezawa et al., Supplement of the Progress of Theoretical Physics, No.**53**, (1973).

[49] R. J. Elliott, et al., Rev. Mod. Phys. **46**, 465(1974).

[50] W. Shan, et. al., J. Appl. Phys. **86**, 2349(1999).

[51] K. M. Yu et. al., J. Appl. Phys. **90**, 2227 (2001).

[52] Y. Makita, et. al., Appl. Phys. Lett. **28**, 287 (1976); S. Gonda et. al., Appl. Phys. Lett. **27**, 392 (1975).

[53] K.M. Yu, et. al., J. Appl. Phys. **90**, 2227 (2001).

[54] M. B. Thomas, et. al., Phys Status Solidi **A2**, K141 (1970).

[55]W. M. Coderre, et. al., Canadian J. Phys, **46**, 1207 (1968).

[56] S. Loualiche, et. al., Appl. Phys. Lett., **59**, 423 (1991); M. J. Jou, et. al., Appl. Phys. Lett., **52**, 549 (1987).

[57] H.P. Xin et. al., Appl. Phys. Lett., **72**, 2442 (1998).

[58] Yong Zhang, et. al., Phys. Rev. B **61**, 7479 (2000).

[59] C. Skierbiszewski, et. al., Appl. Phys. Lett., **76**, 2409 (2000).

[60] B.Q. Sun, et. al., Appl. Phys. Lett., **76**, 2862, (2000).

[61] Takeshi Kitatani, et. al., Jpn. J. Appl. Phys., **38**, 5003 (1999); S. Tanaka, et. al., 25$^{th}$ International Symposium on Compound Semiconductors, Nara, Japan, 1998.

[62]. J. F. Geisz, et. al., J. Crystal Growth, **195**, 401, (1998).

[63] G. Ji, et. al., J. Appl. Phys. **62**, 3366 (1987).

[64] Siegfried Flügge, *Practical Quantum Mechanics I,* Springer-Verlag, 1971.

[65] A. Lindsay et. al., Solid State Commun., **112**, 443 (1999).

[66] E.D. Jones, et. al., Proc. 195$^{th}$ Electrochem. Soc. Meeting, Seattle, WA, **99-11**, 170 (1999).

[67] D. J. Chadi, et. al., Physics Letters, **49 A**, 381, (1974).

[68]. Takashi Kitatani, et. al., Jpn. J. Appl. Phys., Part I, **37**, 753, (1998); Shun-ichi Sato, et. al., Jpn. J. Appl. Phys., Part I, **36**, 2671 (1997).

[69] Sokrates T. Pantelides, Rev. of Mod. Phys., **50**, 797 (1987); F. Bassani, et. al., Rep. Prog. Phys. **37**, 1099(1974).

[70]. E. D. Jones, et. al., Phys. Rev. B **62**, 7144 (2000).

[71] S. Doniach and E. H. Sondheimer, *Green's Functions for Solid State Physicists*, W. A. Benjamin, Inc. (1974); A. A. Abrikosov, L. P. Gorkov and L. E. Dzyaloshiski, *Methods of Quantum Field Theory in Statistical Physics*, Prentice-Hall, Inc. 1963.

[72] P. Perlin, et. al., Appl. Phys. Lett. **76**, 1279 (2000).

[73] J. S. Blakemore, J. Appl. Phys. **53**, R123(1982).

[74] J. F. Geisz, et. al., J. Crystl. Growth, **195**, 401(1998).

[75] I. A. Buyanova, et. al., Appl. Phys. Lett., **81**, 52 (2002).

[76] H. P. Xin, et. al., Appl. Phys. Lett. **76**, 1267 (2000).

[77] M. B. Panish et. al., J. Appl. Phys. **40**, 163 (1969).

[78] S. Ves, et. al., Solid State Commun. **55**, 327 (1985).

[79] T. Takizawa, J. Phys. Soc. Jpn. **52**, 1057 (1983).

[80] B. Gil, et. al., Phys. Rev. B **29**, 3398(1984).

[81] Bernard Gil, Solid State Commun. **114**, 623 (2000).

[82] M. J. Seong, et. al., Appl. Phys. Lett. **79**, 1297 (2001).

[83] J. D. Perkins, et. al., Phys. Rev. B **64**, 121301 (2001).

[84] J. Wu, et. al., Phys. Rev. B **65**, 241303(R) (2002).

[85] M. Cardona, Phys. Rev. **129**, 69 (1963).

[86] Su-Huai Wei, et. al., J. Appl. Phys. **78**, 3846(1995).

[87] K. Strossner, et. al., Solid State Commun. **61**, 275 (1987).

[88] M. J. Seong, et. al., Solid State Commun. **112**, 329 (1999).

[89] D. Nolte, et. al., Phys. Rev. Lett. **59**, 501 (1987).

[90] W. Shan, et. al., Phys. Rev. B **62**, 4211 (2001).

[91] M. J. Seong, Phys. Rev. B **60**, R16275 (1999).

[92] N. Vegelatos, et. al., J. Chem. Phys. **60**, 3613 (1974).

[93] S. H. Wei, et. al., Appl. Phys. Lett. **72**, 2011 (1998).

[94] T. Li, et. al., Phys. Rev. Lett. **74**, 5232 (1995); P. E. van Camp, et. al., Phys. Rev. B **55**, 775 (1997).

[95] K. M. Yu, et. al., Appl. Phys. Lett. **80**, 1571 (2002).

[96] A. Ebina, et. al., Phys. Rev. Lett. **32**, 1366 (1974).

[97] M. J. S. P. Brasil, et. al., Appl. Phys. Lett. **58**, 2509(1991).

[98] D. Lee, et. al., Phys. Rev. Lett. **58**, 1475(1987).

[99] R. People et. al., Phys. Rev. **B 41**, 8431 (1990).

[100] T. Dietl, et. al., Phys. Rev. **B 63**, 195205(2001).

[101] ] I. K. Sou, et. al., Appl. Phys. Lett. **65**, 1915 (1995).

[102] C. Heske, et. al., Appl. Phys. Lett. **74**, 1451(1999).

[103] H. D. Jung, et. al., Appl. Phys. Lett. **70**, 1143 (1997).

[104] A. Mooradion, et. al., Phys. Rev., **148**, 873 (1966).

[105] D. E. Aspnes, Surf. Sci., **37**, 418 (1973).

[106] L. Hsu, PhD thesis, U.C. Berkeley, 1997, unpublished.

[107] A. Jayaraman, et. al., Rev. Mod. Phys., **55**, 65(1983).

[108] H. K. Mao, et. al., J. Appl. Phys., **49**, 3276 (1978).

[109] K. E. Smith, et. al., J. Vac. Sci. Technol. B, **16**, 2250(1998).

## References of Chapter 6


[1] S. Nakamura, and G. Fasol, *Blue laser diode*, Springer, Berlin, (1997)

[2] V. A. Tyagai, et. al., Sov. Phys. Semicond., **11**, 1257 (1977)

[3] T. L. Tansley and C. P. Foley, J. Appl. Phys., **59**, 3241 (1986)

[4] Q. Guo and A. Yoshida, Jpn. J. Appl. Phys. **33**, 2453 (1994)

[5] C. Wetzel, et. al., appl. Phys. Lett., **73**, 1994 (1998)

[6] T. Yodo, et. al., Appl. Phys. Lett., **80**, 968 (2002)

[7] D. C. Look, et. al., Appl. Phys. Lett., **80**, 258 (2002)

[8] T. Inushima, et. al., J. Crystal Growth, **227-228**, 481 (2001)

[9] V. Yu. Davydov, et. al., phys. Stat. solidi (b), **229**, R1 (2002)

[10] C. Stampfl and C. G. Van de Walle, Phys. Rev., **B59**, 5521 (1999)

[11] C. Stampfl, et. al., Phys. Rev., **B61**, R7846 (2000)

[12] C. Persson, et. al., J. Phys. Condens. Matter., **13** 8945 (2001)

[13] H. Lu, et. al., Appl. Phys. Lett., **77**, 2548 (2000)

[14] Y. Saito, et. al., Jpn. J. Appl. Phys. **40**, L90 (2001)

[15] M. D. Sturge, Phys. Rev. **127**, 768 (1962)

[16] W. Shan, et. al., Appl. Phys. Lett., **66**, 985 (1995)

[17] W. Shan, et. al., Appl. Phys. Lett., **71**, 2433 (1997)

[18] W. Shan, et. al., J. Appl. Phys. **85**, 8505 (1999)

[19] D. J. Wolford and J. A. Bradley, Solid State Commun., **53**, 1069 (1985)

[20] P. Perlin, et. al., Phys. Rev. **B64**, 115319 (2001)

[21] M. L. Cohen and D. J. Chadi, in Semiconductor Handbook, edited by M. Balkanski (North Holland, Amsterdam, 1980), Vol. **2** chapter 4b

[22] T. L. Tansley and C. P. Foley, J. Appl. Phys., **60**, 2092 (1986)

[23] M. Kaminska, et. al., Appl. Phys. Lett., **43**, 302 (1983)

[24] S. Nakamura, J. Vac. Sci. Technol. **A 13**, 705 (1995)

[25] I. Akasaki, et. al., Electron. Lett. **32**, 1105 (1996)

[26] K. Itaya, et. al., Jpn. J. Appl. Phys., Part 2, **35**, L1315 (1996)

[27] S. Nakamura, et. al., Appl. Phys. Lett. **70**, 1417 (1997)

[28] K. P. O'Donnell, et. al., Materials Science & Engineering **B 82**, 194(2001)

[29] S. Pereira, et. al., Appl. Phys. Lett. **78**, 2137 (2001)

[30] W. Shan, et. al., Phys. Stat. Sol. (**b**) **216**, 141 (1999)

[32] Evan O. Kane, J. Phys. Chem. Solids. **1**, 249 (1957)

[33] J. Wu, et. al., Appl. Phys. Lett., **80**, 3967(2002)

[34] M. Ferhat, et. al., Appl. Phys. Lett. **80**, 1394 (2002)

[35] V. Yu Davydov, et. al., Phys. Stat. Sol. (**b**) **230**, R4 (2002).

[36] R. W. Martin, et. al., Appl. Phys. Lett., **74**, 263 (1999)

[37] F. A. J. M. Driessen, et. al., Phys. Rev. **B 48**, 7889 (1993)

[38] S. F. Yoon, et. al., J. Appl. Phys. **78**, 1821 (1995)

[39] F. B. Naranjo, et. al., Appl. Phys. Lett., **80**, 231 (2002)

[40] Yong-Hon Cho, et. al., Appl. Phys. Lett. **73**, 1370(1998)

[41] W. Shan, et. al., J. Appl. Phys. **85**, 8507 (1999)

[42] K. S. Kim, A. Saxler, P. Kung, M. Razeghi and K. Y. Lim, Appl. Phys. Lett. **71**, 800 (1997)

[43] J. Wu, et. al., Appl. Phys. Lett. **80**, 4741 (2002)

[44] J. A. Van Vechten and T. K. Bergstresser, Phys. Rev. B **1**, 3351 (1970)

[45] G. Martin, A. Botchkarev, A. Rockett and H. Morkoc, Appl. Phys. Lett. **68**, 2541 (1996)

[46] see, *e. g.*, L. Hsu and W. Walukiewicz, J. Appl. Phys., **89**, 1783 (2001)